Volcanic rocks at the Møre Marginal High: geochemistry, petrogenesis and emplacement mechanisms

Master of Science Thesis

Vilde Nesbø Bakke

Department of Earth Science

University of Bergen

June 2017

Abstract

The opening of the Norwegian-Greenland Sea at the Paleocene–Eocene transition was accompanied by extensive magmatic activity, giving rise to the North Atlantic Igneous Province. The magmatic activity is today manifested along the conjugate Norwegian and Greenland continental margins. In 2014, the Norwegian Petroleum Directorate targeted a unit seen as prograding reflectors in the seismic record along the outer mid-Norwegian Margin by drilling. Approximately 40 m of igneous rocks were recovered from the shallow borehole 6403/1-U-1 at the northernmost part of the Møre Marginal High. This study presents the first documentation of ignoeus rocks from this poorly studied part of the Norwegian Margin. Based on detailed logging, petrographic and geochemical analyses, and interpretation of seismic lines over the study area, the study ads new elements to the understanding of the magmatic evolution of the Norwegian Margin. It is documented that the volcanic succession consists of brecciated material, comprising hyaloclastite and incorporated microcrystalline basalt clasts, and interlayered coherent lava flows. These are interpreted to represent the deposits formed during the build-out of a lava delta system. The findings confirm that the prograding reflectors have a volcanic origin. The cored volcanic succession has relatively uniform petrography and geochemistry, and it is exclusively composed of tholeiitic basalts with a MORB-like character. The basalts show affinities to other igneous rocks from the Vøring Marginal High, SE Greenland Margin and Jan Mayen Ridge, emplaced during the rift-to-drift transition. Geochemical modelling of rare earth elements, and of Nd and Hf isotopic compositions, along with enrichment in selective incompatible elements, provide evidence that the succession has experienced crustal contamination. Based on geochemical modelling, the melts are interpreted to originate from a mantle source more depleted than typical N-MORB sources. Seismic evidence reveals that the succession formed prior to ~56 Ma, probably in the Late Paleocene.

Acknowledgements

This thesis is written in collaboration with the Centre for Geobiology at the University of Bergen and the Norwegian Petroleum Directorate (NPD). I firstly want to thank my supervisor, Prof. Rolf Birger Pedersen, for giving me the opportunity to write this thesis, and for all of the productive discussions and feedback throughout this project. I also want to thank Nils Rune Sandstå at the NPD for helping me with the seismic observations, and for always making my stays at the NPD great during the project. I am also grateful to TGS and NDP for allowing me to include the seismic lines MNR11-90369A and NPD_MB-11-05 in my thesis.

I want to thank Assoc. Prof. Cédric Hamelin for helping me with lab work and for including me when analysing isotopes (MC-ICP-MS) – you have always time for your students, which I appreciate. I also want to thank Ole Tumyr for excellent help during mineral and major element analysis (SEM), Siv Hjorth Dundas for providing trace element analysis (ICP-MS), Yuval Ronen for isotope analysis (TIMS) and Irina Dumitru for preparing thin sections. I want to thank Kevin Glover, Kristian Agasøster Haaga and Randi Storeide for proofreading of the thesis and for constructive feedback on my writing.

Many thanks go to my family and friends for all support and patience during the period. A special thank goes to my significant other, Stephen, for providing a very critical review on my thesis.

Last, but not least, I want to thank all fellow students, and especially all on "Hjørnerommet", for brilliant company and good times during the last two years.

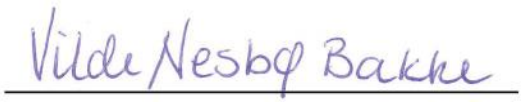

Vilde Nesbø Bakke

Bergen, June 2017

Contents

1 Introduction

1.1 Background

The opening of the Norwegian-Greenland Sea at the Paleocene–Eocene transition was accompanied by extensive and widespread magmatism, giving rise to the North Atlantic Igneous Province (NAIP) (e.g. Eldholm et al., 1989a; Meyer et al., 2007). The magmatic activity has been manifested on the bounding continental margins in the form of extrusives and intrusives along the continent-ocean-transition, forming volcanic passive margins, such as the Norwegian Vøring and Møre margins, and the conjugate Greenland Margin. Thus, the province is an excellent area to study the many igneous features created in the early stages of volcanic passive margin formation (Eldholm et al., 1987a).

The magmatic deposits along the volcanic margins have distinct characteristics in the seismic record, where its morphology and seismic signature depend largely on the environment of emplacement (Planke et al., 2000). During a scientific cruise in 2014, the Norwegian Petroleum Directorate (NPD) drilled the shallow borehole 6403/1-U-1 on the Møre Marginal High, in the easternmost Norwegian Sea. The NPD aimed to core this particular area to unravel the nature of a package observed as prograding clinoforms in seismic records of the area, and adjacent areas along the Norwegian Continental Margin, believed to represent the build-out of a lava delta system (e.g. Planke and Alvestad, 1999; Planke et al., 2000; Abdelmalak et al., 2016). Drilling of this unit has never been performed earlier on the margin, and has been considered to be essential to either confirm, or reject, the interpreted volcanic model for the prograding clinoforms.

Petrological and geochemical data on igneous rocks on the Norwegian Margin is restricted to a few localities on the Vøring Margin on the central mid-Norwegian Margin. Even here, the understanding of the opening-related rocks is largely based upon a single drill hole, namely the volcanic succession recovered on the Vøring Marginal High in drill hole 642 during the Ocean Drilling Program (ODP) leg 104 (Eldholm et al., 1989a; Meyer et al., 2009). The Møre Margin, located south of the Vøring Margin, has received significantly less attention, and the petrological and geochemical nature of the igneous rocks here is yet unknown. This study presents the first documentation of volcanic rocks emplaced on this poorly studied part of the Norwegian Margin. Thus, a study of the nature and petrogenesis of the volcanic succession,

and its relationship to the magmatism recorded at the Norwegian and the conjugate Greenland margins, may be of significant interest considering the magmatic evolution of the Norwegian Margin.

1.2 Aim and objectives of the study

The overall aim of this study is to investigate the nature, composition and emplacement mechanisms of the volcanic succession in drill hole 6403/1-U-1 on the Møre Marginal High. This is in order to provide new knowledge of the rift-to-drift-related volcanic activity along the Norwegian Margin.

The specific objectives of this study are to:

- Provide a description of the cored volcanic succession and an interpretation of the environment of emplacement
- Provide a detailed petrographic and geochemical characterisation of samples collected from the volcanic succession in order to clarify its formation and sources
- Compare the samples to other igneous rocks that previously have been reported from the region, and to evaluate their relationship

To substantiate the listed objectives, a brief interpretation of two seismic lines located over the study area has been carried out as part of this study in order to further constrain the emplacement history of the volcanic succession.

1.3 Study area

In 2014, the NPD contracted Fugro Seacore to conduct shallow drilling operations at extreme water depths of 2130 m, in the easternmost part of the Norwegian Sea. The drill hole, 6403/1-U-1, is located on the northernmost part of the Møre Marginal High on the Møre Margin, just southwest of the Faeroe-Shetland Escarpment, close to the Jan Mayen Fracture Zone (figs. 1.1 and 1.2). At this scientific cruise the vessel Greatship Manisha was mobilised with the Fugro owned mobile rig “R100” to perform the drilling operations. After several attempts, the drill hole 6403/1-U-1 proved to be a success. The drilling operations started at the 19th of May and reached TD at 170 m below seafloor the 5th of June.

A thin cover of Cenozoic sediments overlies the cored succession on the marginal high. The cored section of the borehole extends from 110-170 m below the sea floor (mbsf) (fig. 1.2). The scientific well had a core recovery of 50 m (83%), and the cored succession consists of approximately 12 m of sediments and 38 m of igneous rocks, in which the drill hole terminates. The overlaying, brownish-black, silty sediments are interpreted to represent marine deposits eroded from central volcanoes located in the rift zones during continental breakup (N.R. Sandstå, personal communication, 2016). Palynological analysis of one sediment sample from the base of this overburden suggests an Early Eocene (Early Ypresian) age (55 Ma) (R.W. Williams, personal communication, 2017).

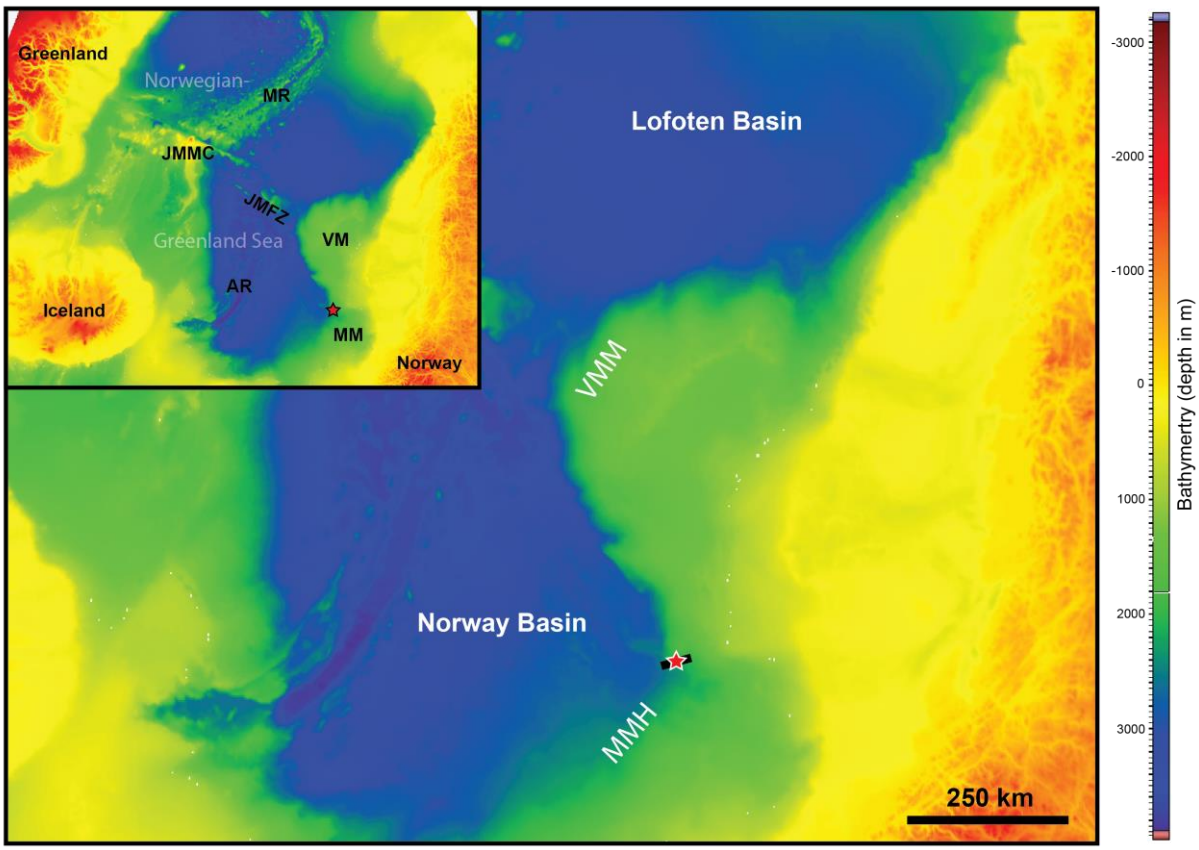

Figure 1.1: Bathymetric map over the study area. A red star marks the shallow borehole 6403/1-U-1. The black line underlying the star shows the position of the seismic line in fig. 1.2. MM: Møre Margin; VM: Vøring Margin; JMFZ: Jan Mayen Fracture Zone; JMMC: Jan Mayen Microcontinent; AR: Aegir Ridge; MR: Mohns Ridge; MMH: Møre Marginal High; VMM: Vøring Marginal High.

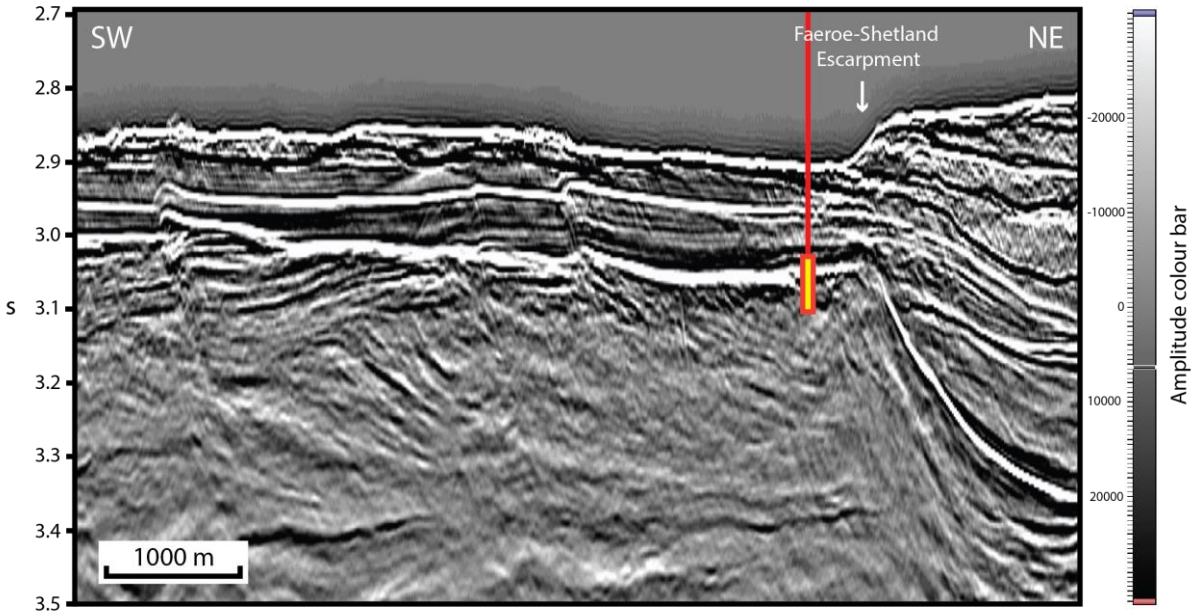

Figure 1.2: Seismic line (NPD_MB-11-05) displaying the targeted dipping and prograding reflectors along with the position of the 6403/1-U-1 borehole. The area of the borehole filled with yellow represent the cored succession.

2 Regional geology and previous studies

This chapter focuses on the geological framework of the mid-Norwegian Margin, situated between 62–69°N (fig. 2.1), with emphasis on the volcanic succession emplaced during the Paleocene–Eocene transition. This area comprises two main segments, namely the Møre Margin to the south and the Vøring Margin to the north, each between 400–500 km long (Faleide et al., 2008). The margin borders to the elevated Norwegian mainland to the east, the Lofoten-Vesterålen Margin to the north, the Norwegian-Greenland Sea to the west, and has its southern boundary at around 62°N, near the Faeroe Islands (Planke et al., 1991). The Norwegian-Greenland Sea is the result of continental separation, and subsequent seafloor spreading, which occurred between Eurasia and Greenland close to the Paleocene–Eocene transition (~56 Ma), and is bounded by passive volcanic margins (Eldholm et al., 1987a; Eldholm et al., 1987b; Eldholm et al., 1989b) such as the Møre, Vøring and Greenland margins.

2.1 Geological evolution of the mid-Norwegian Margin

The generation of seafloor in the area represents the final result of several extensional events and the formation of sedimentary basins since the end of the Caledonian Orogeny, lasting over a period of about 350 Ma (Doré et al., 1999). The rifting episodes in the area can be divided into three main phases: the Late Paleozoic, the late Mid-Jurassic to Early Cretaceous and the Late Cretaceous to Early Eocene rifting phases (Brekke, 2000). At the onset of the final rifting phase in the Late Cretaceous, the mid-Norwegian Margin was part of an epicontinental sea situated between Eurasia and Greenland (Hjelstuen et al., 1999). In the Paleocene to Earliest Eocene the area experienced uplift caused by the increased heat flow associated with the severe rifting event (Brekke, 2000). The final rifting phase occurred within a region of extensively stretched and thinned lithosphere, causing continental separation of Greenland and Eurasia, and subsequent propagation of seafloor spreading from the central North Atlantic.

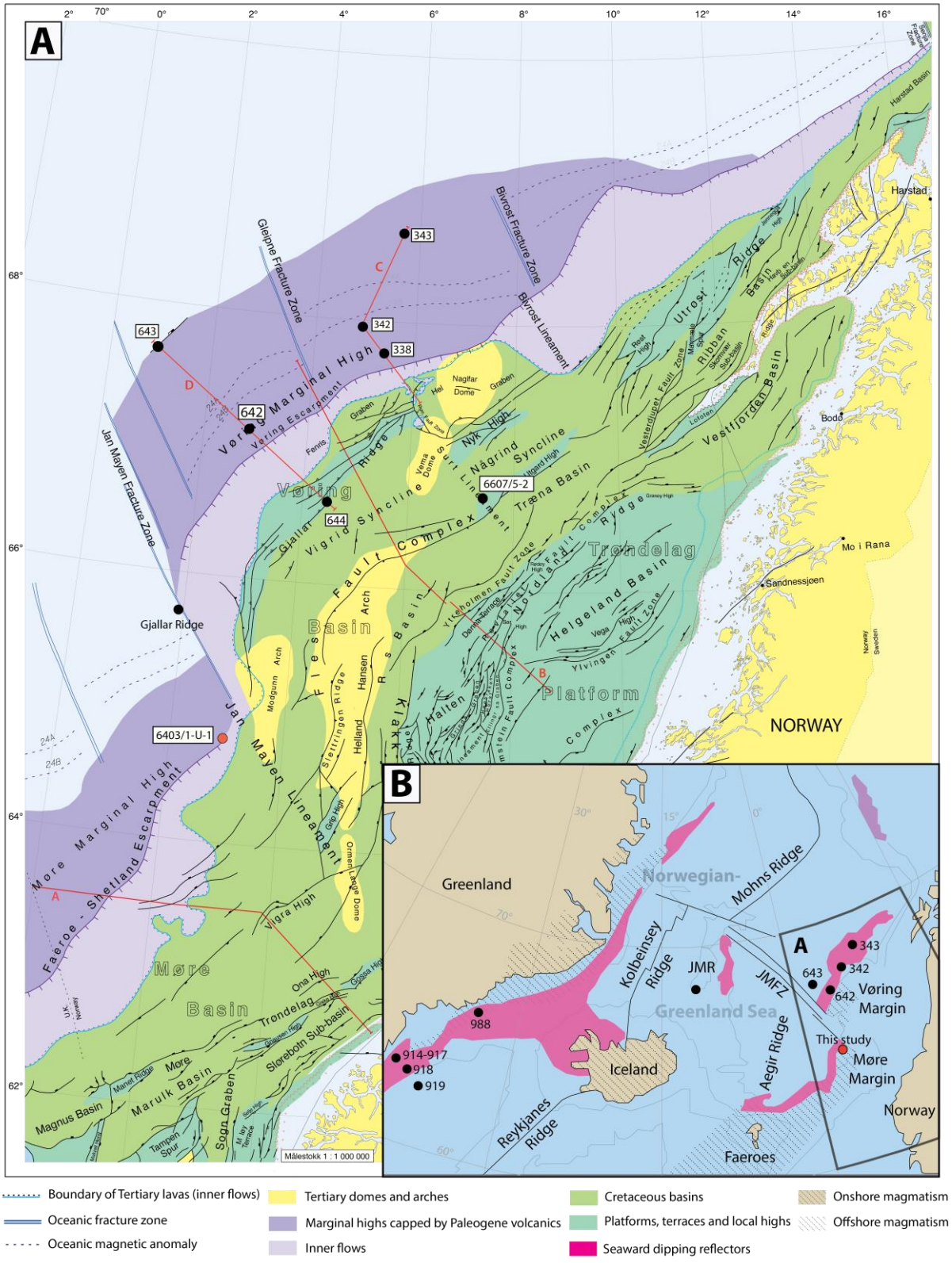

Figure 2.1: (A) Main structural elements of the mid-Norwegian Margin, modified and simplified from Blystad et al. (1995), displaying the profiles (red lines) and drill and sampling sites addressed in the thesis. The study area (drill hole 6403/1-U-1) is shown as a red circle; other drill holes and sampling sites are displayed as black circles. **(B)** Map of the Norwegian-Greenland Sea and its passive volcanic margins, displaying drill and sampling sites, modified from Larsen et al. (1994a). The black box represents the area of fig. A. JMR: Jan Mayen Ridge; JMFZ: Jan Mayen Fracture Zone.

The magmatic activity in the Northeast Atlantic area was initiated at about 62 Ma, by small volume, continent-based magmatism (Saunders et al., 1997). The continental breakup and the earliest seafloor spreading were accompanied by a period of 2–3 million yeas of voluminous and regional magmatism, forming the North Atlantic Igneous Province (NAIP) (Eldholm et al., 2002). The conventional model for the NAIP, and the resulting magmatic activity, is that it is caused by elevated mantle temperatures induced by the Icelandic mantle plume (e.g. Eldholm et al., 2002). However, other models have also been proposed to explain its formation, including mantle heterogeneities (Korenaga, 2004; Foulger and Anderson, 2005; Foulger et al., 2005) and small-scale convection cells in the mantle (King and Anderson, 1995; King and Anderson, 1998; King, 2005).

The NAIP have left imprints on the mid-Norwegian Margin in the form of buried marginal highs, capped by magmatic extrusive complexes, including wedges of basalt flows, seen as Seaward Dipping Reflectors (SDRs) in seismic records (e.g. Eldholm et al., 1989b). Seismic surveys have also identified so-called high-velocity lower crustal bodies (LCBs) beneath the margin, generally interpreted to represent mafic intrusions in the lower crust (underplating) (Mjelde et al., 2002; Mjelde et al., 2009a; Mjelde et al., 2009b), and sills intruding into sedimentary basins (e.g. Planke et al., 2005).

After the continental breakup, the mid-Norwegian Margin evolved in response to subsidence and sediment loading, as the Norwegian-Greenland Sea progressively became wider and deeper (Eldholm et al., 2002). At Miocene times, the area underwent compression, probably related to changes in relative plate movements, leading to the formation of domes and aches on the margin (Doré et al., 1999; Brekke, 2000).

2.2 Main structural setting

The main structural setting of the margins is displayed in figs. 2.1 and 2.2, and consist of a central area of NE–SW trending, deep Cretaceous basins, namely the Møre and Vøring basins, which are flanked by paleo-highs and the elevated mainland (Brekke, 2000). Other structural features, such as marginal highs and escarpments, are common for the Møre and Vøring margins.

The marginal highs to the west of the basins are termed the Møre Marginal High to the south, and the Vøring Marginal High to the north. The Faeroe-Shetland Escarpment and the Vøring Escarpment separate the marginal highs from the basins, respectively. The area east of the escarpments is characterised by structural elements typically formed before mid-Cretaceous time (Eldholm and Mutter, 1986), whereas the area west of the escarpment is related to the Cenozoic passive margin formation (Eldholm et al., 1987a).

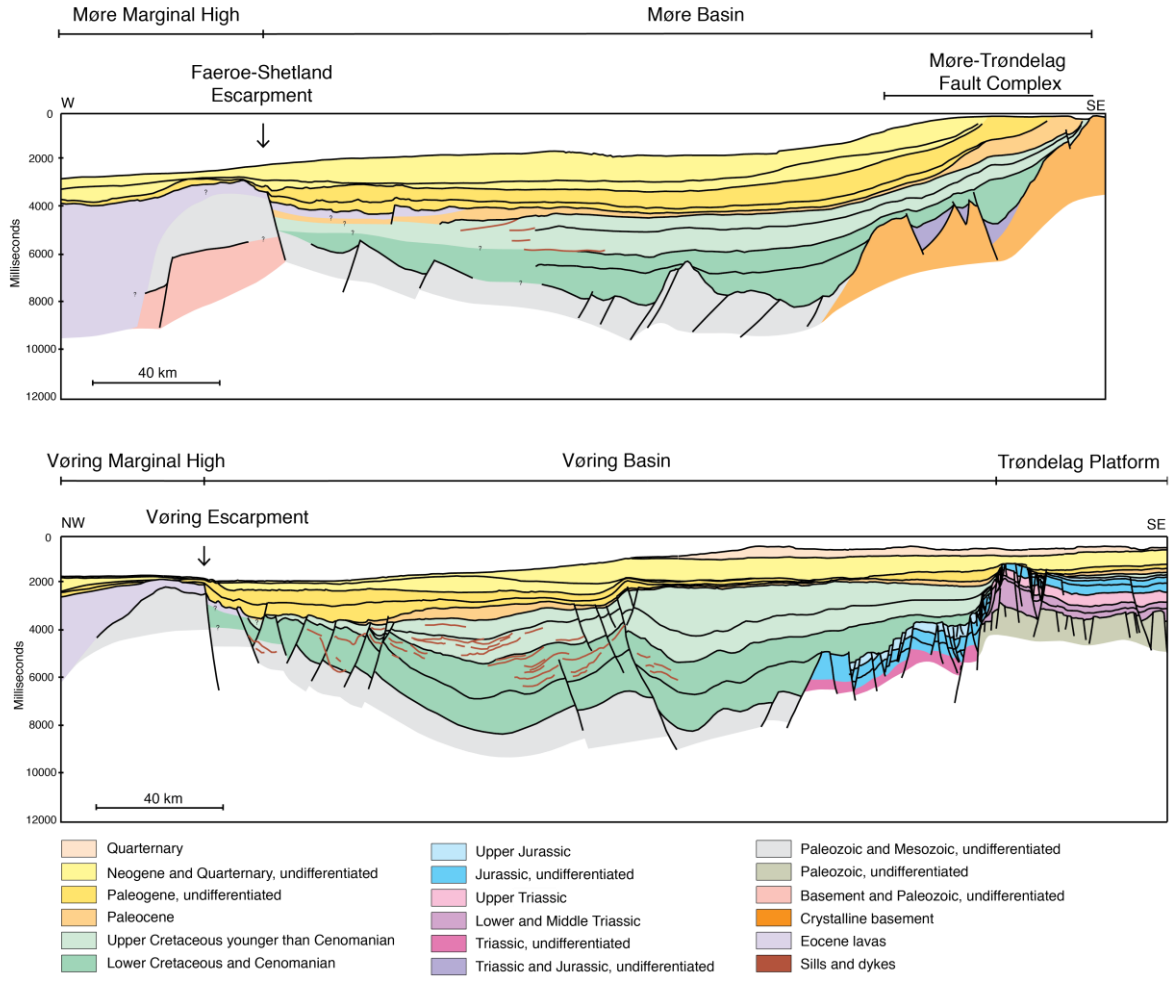

Figure 2.2: Interpreted geoseismic profiles of the Møre (upper profile) and Vøring (lower profile) margins, slightly modified from Blystad et al. (1995). The locations of the profiles are seen respectively as line A and B in fig. 2.1A.

The area east of the escarpments is dominated by the Late Jurassic–Early Cretaceous rift episode, forming the deep Cretaceous Møre and Vøring basins. The Møre Basin is relatively unstructured, and has acted as a major depocenter since the Late Jurassic (Eldholm et al., 1987a). An exception is the Møre-Trøndelag Fault Complex, located at the eastern flank of

the basin, consisting of a system of fault-controlled ridges, highs and minor basins (Brekke, 2000). The fault complex probably originated in Triassic times, but was greatly reactivated during the Late Jurassic–Early Cretaceous extensional episode (Brekke, 2000). The Vøring Basin, on the other hand, is more structured, containing grabens, sub-basins and structural highs (Blystad et al., 1995).

Two NW–SE trending lineaments segment the provinces, as the Jan Mayen Lineament separates and offsets the Møre and Vøring margins, and the Bivrost Lineament marks the northern extent of the Vøring Margin. The lineaments continue oceanward into the oceanic crust as the Jan Mayen and Bivrost Fracture Zones respectively, and they probably represent an old, structural grain in the crystalline basement (Brekke, 2000).

2.3 Marginal highs and associated breakup related igneous rocks

The Møre and Vøring marginal highs were first identified as buried acoustic basement highs in single-channel seismic profiles by Talwani and Eldholm (1972), found at the outer parts of the Møre and Vøring margins, respectively. The marginal highs are bounded to the east by the escarpments, and to the west by the transition into "normal" oceanic crust (Blystad et al., 1995). The continent-ocean boundary has typically been placed landward of the oldest seafloor spreading anomaly in the Norwegian-Greenland Sea, 24B, just seaward of the termination of reflector K (fig. 2.4) (e.g. Smythe, 1983; Eldholm et al., 1989a).

The Vøring Marginal High is accessible for drilling investigations as it is buried below a thin cover of Cenozoic sediments at relatively shallow water depths. It has therefore been a target area for studying the early stages of the formation of passive volcanic margins. The volcanic succession on the Møre Marginal High has not, until now, been drilled. Thus, chemical data of the opening-related magmatism on the mid-Norwegian Margin is limited to drill cores collected on the Vøring Margin. This area has been investigated by scientific drill holes during the Deep Sea Drilling Project (DSDP) leg 38 (sites 338, 342 and 343) (figs. 2.1 and 2.3), during the Ocean Drilling Program (ODP) leg 104 (sites 642, 643 and 644) (figs. 2.1 and 2.4) and by a commercial drill hole (the Utgard borehole 6607/5-2) (fig. 2.1). The ODP leg 104 site 642 has in particular provided key data on the early volcanic passive margin history.

The top of the basement highs is marked by a smooth, strongly reflecting horizon, termed EE (Eldholm et al., 1989b). This horizon was confirmed to consist of basalt, as the DSDP Leg 38 penetrated the horizon, by drilling on top of the Vøring Marginal High (sites 338 and 342) and at the base of the slope towards the Lofoten Basin (site 343) (Talwani and Udintsev, 1976). Kharin (1976) reported the basalt from site 343 and 342 to be of alkaline and sub-alkaline composition, and the basalt from site 338 as low-alkaline tholeiites. The basalts from site 338 and 342 have been dated to be of late/middle Eocene age, and are interpreted to represent thick basalt flows, sills or dikes (Kharin, 1976; Kharin et al., 1976). The basalts at site 343 are considerably younger (28.5±2 Ma), indicating that the basalts are either later formed intrusives, or that their high amount of alteration have changed the K/Ar data (Kharin et al., 1976).

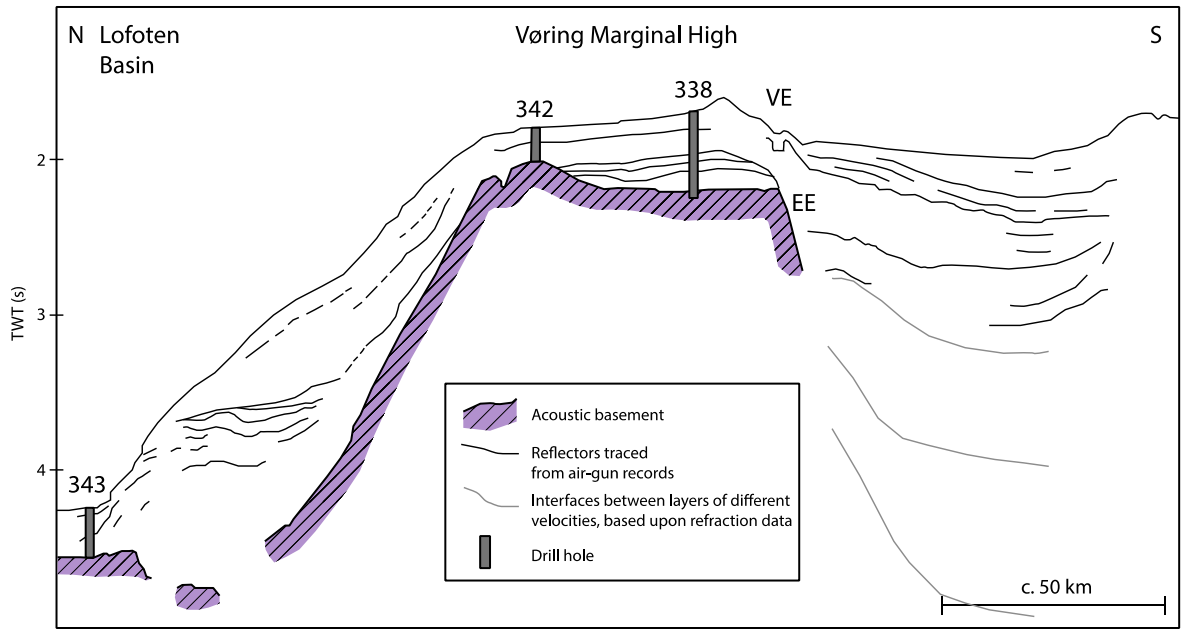

Figure 2.3: Interpreted seismic-reflection profile across the Vøring Marginal High (line C in fig. 2.1A), displaying the locations of DSDP sites 338, 342 and 343, modified from Eldholm et al. (1987a). VE: Vøring Escarpment; EE: basement reflector.

EE is partly underlain by seaward-dipping reflector sequences, where the inner part of the SDRs rest on a base reflector, named K (e.g. Talwani et al., 1983). During the ODP Leg 104 the borehole 642 was drilled on the Vøring Marginal High, where a 910 m-thick volcanic succession was collected, and further divided into an upper (US) and lower series (LS) (Eldholm et al., 1987b). The upper and lower series are separated by a 13.2 m-thick sediment bed, which corresponds to reflector K (Eldholm et al., 1989b).

Eldholm et al. (1987b) revealed that the Vøring upper series corresponds to the SDRs. Their study reported that the unit is composed of mainly subaerially emplaced lava flows and interlayered volcaniclastic sediments of late Middle to Early Eocene age. The lava flows´ composition has been described as normal mid-ocean ridge basalt (N-MORB) by Eldholm et al. (1987b), and as transitional-type, i.e. slightly enriched in LRE-elements, mid-ocean ridge tholeiitic basalt (T-MORB) (Viereck et al., 1988; Viereck et al., 1989; Meyer et al., 2009), and are generally considered to be uncontaminated by the continental basement. The succession has strong affinities to other plateau basalts within the NAIP and MORB basalts from the Reykjanes Ridge (Eldholm et al., 1987b; Viereck et al., 1989).

The Vøring lower series is more heterogeneous, consisting of rhyolitic ignimbrites, dacites and basaltic andesites (Eldholm et al., 1987b; Parson et al., 1989). Eldholm et al. (1987b) subdivided the lower series flows into two chemically distinct groups. The upper part of the series, group B, consists of dacitic peraluminous flows, believed to originate from partial melting of upper crustal sedimentary or metasedimentary rocks. The lower part of the series, group A, is composed of basaltic andesites, and is thought to be the result of mixing of MORB-type tholeiitic melts with group B melts. In addition, Parson et al. (1989) further subdivided group A, where A2 share the characteristics of the former group A, and where A1 has a chemically composition intermediate between A2 and B. This may point to a repetition of, or a transition phase in, the melt mixing process (Parson et al., 1989).

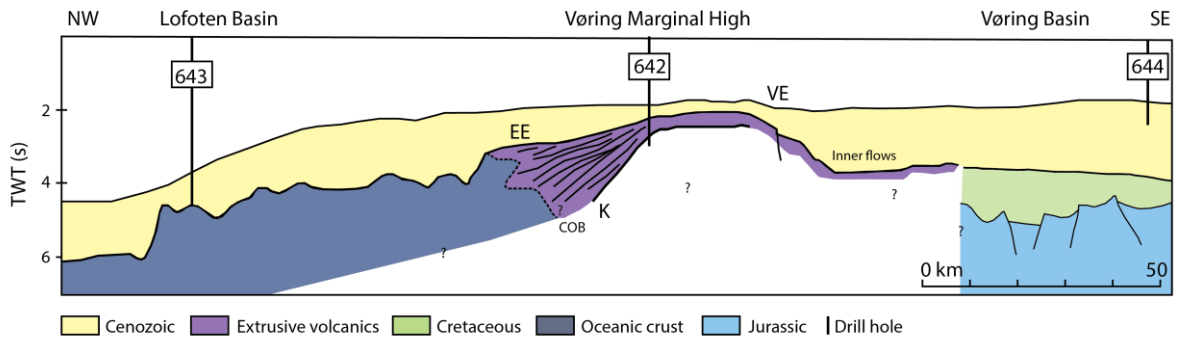

Figure 2.4: Interpreted multichannel seismic reflection profile of the outer Vøring Margin (line D in fig. 2.1A) displaying the drill sites of the ODP leg 104, modified from Eldholm et al. (1989b). EE: top of the lower Eocene flow series; K: reflector K; COB: Continent-Ocean Boundary; VE: Vøring Escarpment. The SDRs are expressed as dipping reflectors between reflector EE and K.

Meyer et al. (2009) restudied the ODP Leg 104 site 642 core, and based on a new and improved sample set, they extended the subdivision of the lower series to four groups; A1, A2, B1 and B2, where B2 represent the most silicic magmas of the lower series.

The lower series is also intruded by two tholeiitic dikes of a N-MORB character, termed D5 and D6. These have been interpreted to derive from an extremely depleted mantle source, and show evidence of assimilation of upper crustal material (Viereck et al., 1989). The trace element pattern of the dikes reveals that they do not originate from the same source as the upper series, thus they cannot represent feeder dikes. As a result, this fact rather points toward spatial or temporal heterogeneities in the mantle during the time of emplacement of the upper and lower series (Meyer et al., 2009).

Although this chapter focuses on the Norwegian Margin, it is relevant to address the nature of the rift-related rocks on the conjugate SE Greenland Margin. The margin has been investigated by drilling operations during the ODP leg 152 (sites 914–919) and 163 (sites 988–990). The most successful penetration was at site 917, located close to the inner part of the SDRs on the margin. The succession has been divided into three different series based on petrography; the upper, middle and lower series (Larsen et al., 1994b). The lower series varies from picrite to evolved tholeiite, the overlying middle series is more evolved and comprises dacites and evolved tholeiites, and the upper series consist of olivine basalt and picrite (Fitton et al., 1998b). The upper series is largely uncontaminated, whereas chemical and isotopic data of the lower and middle series provides clear evidence of crustal assimilation, where the lower and middle series seems to be affected by mainly the lower and upper crust, respectively (Fitton et al., 2000). The entire succession is mainly believed to originate from a depleted mantle source (Fitton et al., 2000).

Following the pioneering work of the ODP Leg 104, more recent work has been done to improve the understanding of breakup-related magmatism on the mid-Norwegian Margin. Neumann et al. (2013) reported geochemical analyses of two breakup-related sills of doleritic composition from the commercial Utgard borehole (6607/5-2) in the Vøring Basin. Their study concluded that the sills originated from partial melting of a depleted mantle source, and that the magma underwent extensive fractional crystallisation in the lower crust along with minor assimilation of crustal melts. In addition, *in-situ* sampling of igneous rocks by a Remotely Operated Vehicle (ROV) has been conducted along the southern extension of the

Gjallar Ridge in the western Vøring Basin, and along the southern Jan Mayen Ridge (JMR) in the Norwegian-Greenland Sea, in 2013 and 2011-2012 respectively (fig. 2.1). Microgabbros and rocks of dacitic compositions were collected at the Gjallar Ridge. The microgabbros have been described as tholeiitic N-MORB to E-MORBs that have been contaminated by crustal material, and the dacitic rocks are interpreted to largely be derived from partial melting of upper crustal material (Styve, 2015). The igneous rocks collected on the southern JMR has been described as tholeiitic MORBs, characterised by abnormally depleted trace element signatures, with no sign of continental influence (Haaga, 2014). The southern JMR, which was located adjacent to the Møre Margin at breakup time, is thus believed to represent the earliest seafloor-spreading phase in the area.

2.4 Escarpments and associated lava delta

The Vøring and Faeroe-Shetland escarpments are distinctive NE–SW trending features found along the Møre and Vøring margins. The escarpments are characterised by a sharp landward increase of the depth of the acoustic basement (i.e. reflector EE) (figs. 2.3 and 2.4) (Hinz et al., 1984). Thus, the escarpments represent the edge of the thick pile of Early Eocene flood basalts found at the marginal highs. The Vøring Escarpment is more prominent in the southern than the northern part, and the Faeroe-Shetland Escarpment is generally less poorly defined than the Vøring Escarpment (Talwani et al., 1983).

The nature and origin of the escarpments has been a subject of debate for decades. They were originally interpreted to represent the continent-ocean boundary (COB) (Talwani and Eldholm, 1972). Others have suggested that the escarpment is mainly a fault-controlled feature (e.g. Skogseid and Eldholm, 1989; Brekke, 2000). Smythe et al. (1983) suggested that the Faeroe-Shetland Escarpment marked the temporary shoreline separating subaerially emplaced basalt flows from a restricted shallow-water shelf. More recently, is has been documented that the escarpments mark the boundary of subaerially and subaqueously emplaced lava flows, and that they represent the termination of a unit seen as prograding reflectors in seismic records, interpreted as prograding lava-fed deltas (fig. 2.5) (e.g. Planke et al., 2000; Berndt et al., 2001; Abdelmalak et al., 2016).

The lava delta unit is associated with the landward and inner flows (fig. 2.5). The landward flows are commonly located landward or below the inner SDRs on seismic profiles, and are

interpreted to represent subaerially erupted and emplaced lava flows (Abdelmalak et al., 2016). Upon contact with the sea at the paleo-shoreline, the flows undergo quenching and fragmentation into basalt fragments, a deposit termed hyaloclastite. The fragments are rapidly being deposited downslope by gravitational processes, constructing inclined foresets (Abdelmalak et al., 2016). The inner flows are found landward or below the lava delta unit, and is also generally interpreted to represent submarine hyaloclastite deposits (Planke and Alvestad, 1999). Planke et al. (2000) and Abdelmalak et al. (2016) interpret the inner flows to have formed simultaneously with the landward flows and the lava delta, sourced by fissures in the area of continental breakup. Due to this, the units have been compared to coarse-grained, siliciclastic Gilbert-type deltas, where the landward flows and inner flows represent the top and bottom set of the delta respectively (e.g. Planke et al., 2000). This contradicts the model presented by Brekke (2000) where the inner flows represent the first flood basalts emplaced on the margin, separated from the marginal highs when faulting initiated along the escarpments. Thus giving accommodation space for the build out of a lava delta system. The geometry of the lava delta will depend of factors such as lava supply, relative sea level changes and the vertical tectonic movement as demonstrated in fig. 2.5.

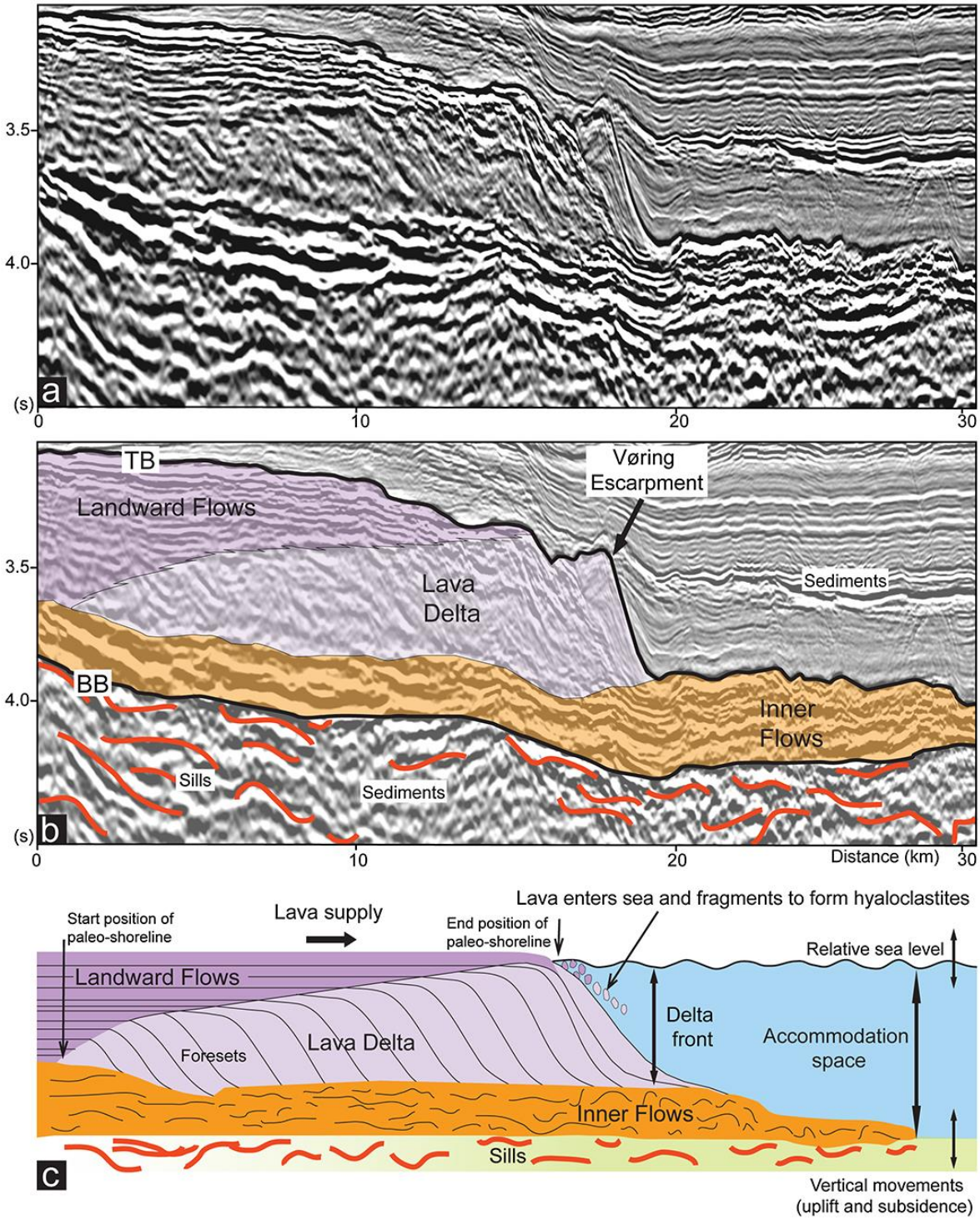

Figure 2.5: Figure from Abdelmalak et al. (2016): **(a)** An uninterpreted and **(b)** interpreted seismic section from the Vøring Margin displaying the key seismic facies units of the lava delta system. **(c)** Schematic illustration (not to scale) showing the development of a lava-fed delta. TB: top basalt; BB: base basalt.

3 Methods

3.1 Core description

The description of the volcanic succession in core 6403/1-U-1 was carried out during two periods, 30–31th of March and 3–7th of October 2016, at the Norwegian Petroleum Directorate (NPD) in Stavanger. The description followed standard logging procedures, where different lithological units of the core was described for primary volcanic features, grain size, structures, contacts and alteration characteristics. Due to its fragile nature, the core had not been split in two halves, which made the investigation of the core more challenging. Samples were collected by the criteria of covering the different lithologies observed in the core, as well as from different depths. One mineral sample was analysed by a Bruker Eco D8 Advanse X-ray Powder Diffraction (XRD) instrument, to identify its composition.

3.2 Petrographic observations

Eight samples, C.10, C.15, C.20, C.21, C.23, C.28, C.31 and C.34, were prepared for petrographic observations. A section of the sample, slightly less than a thin section glass (27*46 mm), was cut by a diamond saw at the University of Bergen (UiB) for further thin section preparations. The diamond saw was cleaned with water and dried with compressed air between each sample preparation. The surface of the sample was then smoothened by the use of a diamond and aluminium-grinding instrument. The sample was further cut with a linear precision mini saw to a 2 mm thickness, before optimal thickness was reached (30 μm) by grinding. Subsequently, it was polished with a diamond spray.

The petrographic observations were carried out using a Nikon Eclipse E200 polarising microscope. Optical properties such as colour, relief, birefringence, mineral habit etc. were considered during the process of identifying the mineral assemblage of the samples, along with other important properties, such as texture.

A Zeiss Supra 55VP Scanning Electron Microscope (SEM) was used to supply and confirm the interpretations made by the polarising microscope. Thin sections were coated with graphite by using an Agar Turbo Carbon Coater, before they were ready to be analysed in the SEM. The anorthite (An) content of plagioclase and forsterite (Fo) content of olivine for two samples, C.23 and C.28, were determined using the SEM. The standardisation and analysis

procedures were the same as for the major element analysis described below, except that the USNM 113716 basalt glass standard was not used during this standardisation. Internal forsterite and fayalite mineral standards were measured to address the precision and accuracy of the results at the time of analysis (Appendix C). In addition to this, a Horiba LabRAM HR Spectrometer was used to detect the type of zeolite present in some samples.

3.3 Major elements

Thin sections where fresh glass was observed (samples C.23, C.28, and C.31) were prepared for *in situ* major element analysis. The analyses were carried out by the same SEM using an accelerating voltage of 15kV. A mixture of minerals, synthetic oxides, pure metals and the USNM 113716 basalt glass standard was applied during standardisation. A working distance of 9 mm, at a magnitude of 4800X, was used during standardisation and analyses. The analysing area varied between 2–5 μm, and the counting times were 50 s. A ZAF-correction (atomic nr., absorption, fluorescence) was applied, and a minimum of nine points were analysed per sample.

A SEM uses a focused beam of high-energy electrons to form a variety of signals on the sample surface. The elemental concentration data were acquired by Energy-Dispersive X-Ray Spectrometry (EDS) equipped with a Silicon Drift Detector (SDD), which measures the x-rays generated from the electron beam-sample interaction. The elemental concentrations of the samples were subsequently normalised to 100%.

The recent improvements in EDS performance with the SDD (SDD-EDS) provides an accuracy and precision equal to that obtained by an electron microprobe and high spectral resolution wavelength-dispersive spectrometry (Newbury and Ritchie, 2015). The USNM 113716 basalt glass standard was used to evaluate the precision and accuracy of the results. The precision varied between 1.44–5.29% for most oxides. Two oxides had considerable higher values, K_2O and MnO, with a precision of 29.46% and 32.52% respectively. The accuracy of the results (REC%) was quantified by how many per cent of the standard value that was recovered during analyses, and ranged from 96.59–110.08% for all elements, except K_2O, which had a recovery of only 66.67%. The precision and accuracy, along with the recommended values for the USNM 113716 standard, are listed in Appendix D.

3.4 Trace elements

Samples where fresh volcanic glass was observed, or could possibly be present (C.18, C.20, C.23, C.28, C.31 and C.33), were prepared for trace element analysis. The sample material was crushed with a hammer to a size ranging from about 1–0.25 mm. The sample was packed in hardwearing plastic bags during hammering. In addition, the hammer and the surface of hammering were cleaned with water and ethanol and dried with compressed air between the preparations of each sample to avoid contamination. The crushed sample material was then sieved to fractions of 1–0.5 mm and/or 0.5–0.3 mm depending on the sample quality. The sieving equipment was washed with water and ethanol and thereafter dried with compressed air between each sample to limit contamination.

Visible alteration and phenocrystals were avoided by handpicking fresh glass from the sample factions using a Leica MZ6 modular stereomicroscope and standard picking equipment. The freshest samples (C.23, C.28 and C.31) were mostly picked from the 1–0.5 mm fraction, and more altered samples (C.18, C.20 and C.33) were picked from the finer 0.5–0.3 mm fraction. It should be noted that it generally was hard to pick fresh material from these samples, as they had suffered more alteration than expected. Many of the picked glass pieces contained filled vesicles and fractures, and some resembled palagonite (altered glass), rather than fresh glass. In particular, this was the case for sample C.33. It was therefore expected that this would influence the geochemical results of these samples.

As much sample material as possible was collected from each sample (c. 200–300 mg). The picked material was weighed, and further dissolved in 3 ml concentrated HF. Thereafter it was digested on a heating plate for 72 hours and evaporated to dryness. The reaction product was added 20 ml 2 N HNO_3 and evaporated under sub-boiling conditions. The remaining soluble product was further dissolved in 0.45 N HNO_3 and diluted to 50 ml in a volumetric flask before it was ready to be analysed.

Trace elements were analysed using a Thermo Scientific Element XR Inductively Coupled Plasma Mass Spectrometer (ICP-MS) at the University of Bergen. The ICP-MS instrument consists of a sample introduction system, an ion source, a mass spectrometer and a detector. The sample is being ionised by the ion source (ICP-source), usually by argon as the carrier gas. The ions are then being focused into the mass spectrometer by a set of electrostatic

lenses, where they are separated by their mass-to-charge ratio, so that only specific ions strike the detector. The detector translates the number of ions hitting the detector into a signal that can be measured.

The precision and accuracy of the results were evaluated by repeated measurements of the BCR-2 geostandard during analyses. The precision of the results (RSD%) was calculated from the variation of values during the repetitive standard runs, and varied from 1.80–3.41% for the different trace elements. The accuracy of the results (REC%) was quantified by how many per cent of the standard value that was recovered during analyses, and ranged from 83.96–108.41% for the different trace elements. The precision and accuracy, along with the recommended standard values, are listed in Appendix E.

3.5 Isotopes

To avoid isobaric interferences during analysis of isotopic ratios, the solutions prepared for ICP-MS analysis were further processed through chromatography in a clean lab environment at the University of Bergen.

The extract remaining from the ICP-MS-analysis was evaporated to dryness, and re-digested with 3 ml concentrated HF. The digestion product was transferred to centrifuge tubes, and the fluoride precipitate was separated from the HF-supernatant.

The dry fluoride residue was dissolved in 20 ml 3 N HNO_3. Pb and Sr were separated by specific extraction chromatography using a modified version of the method described by Deniel and Pin (2001). The residual effluent were dried in PFA vials, re-dissolved in 1.5 ml 2 N HNO_3, and REE-separation was preformed by a modified version of Pin et al. (1994). Nd was subsequently separated using a modified version of the method described by Winchester (1963). The Hf-supernatant was evaporated to dryness, re-dissolved and subsequently dried three times in 1 ml 6 M HCl, before it was taken up in 1 ml of 1 M HCl+0.15 M HF. Hf was subsequently separated using the method described in Hamelin et al. (2013).

The Sr isotopes were measured on a Finnigan MAT262 Thermal Ionization Mass Spectrometer (TIMS) at the University of Bergen. The TIMS differ from the previously described ICP-MS by Thermal Ionization (TI) of atoms prior to entering the mass

spectrometer, and by a series of collectors allowing for several ion beams to be measured simultaneously. Sr isotopic ratios were corrected for mass fractionation using $^{88}Sr/^{86}Sr$ ratio of 8.375209. Ten measurements on the SRM 987 Strontium Carbonate Standard at the time of analyses yielded an average $^{87}Sr/^{86}Sr$ ratio of 0.710229±8(2σ).

The Pb, Nd, and Hf isotopes were measured on a Plasma 2 Multicollector Inductively Coupled Plasma Mass Spectrometer (MC-ICP-MS) at the University of Bergen. This instrument differs from the previously described ICP-MS by multiple collectors (MS) allowing for measuring several ion beams simultaneously.

Instrumental mass fractionation of Pb was corrected for using a Tl doping. Eleven replicates of the international Pb isotope standard, NBS981, over the time of analyses gave an average of 16.931±4, 15.481±5 and 36.67±2 for $^{206}Pb/^{204}Pb$, $^{207}Pb/^{204}Pb$ and $^{208}Pb/^{204}Pb$ respectively. The Pb ratios were normalised to the NBS981 standard ratios of 16.9371, 15.4913 and 36.7213, for $^{206}Pb/^{204}Pb$, $^{207}Pb/^{204}Pb$ and $^{208}Pb/^{204}Pb$ respectively. Sixteen replicates of the Bergen internal Hf standard yielded an average $^{176}Hf/^{177}Hf$ ratio of 0.282125±5. The Hf ratios were normalised to a $^{176}Hf/^{177}Hf$ ratio of 0.282127, which corresponds to the ratio of the international Hf standard, JMC475, of 0.282157. Four replicates of the international Nd standard, JNdi, gave an average $^{143}Nd/^{144}Nd$ ratio of 0.512058±1. The Nd ratios were normalised to the JNdi $^{143}Nd/^{144}Nd$ ratio of 0.512115.

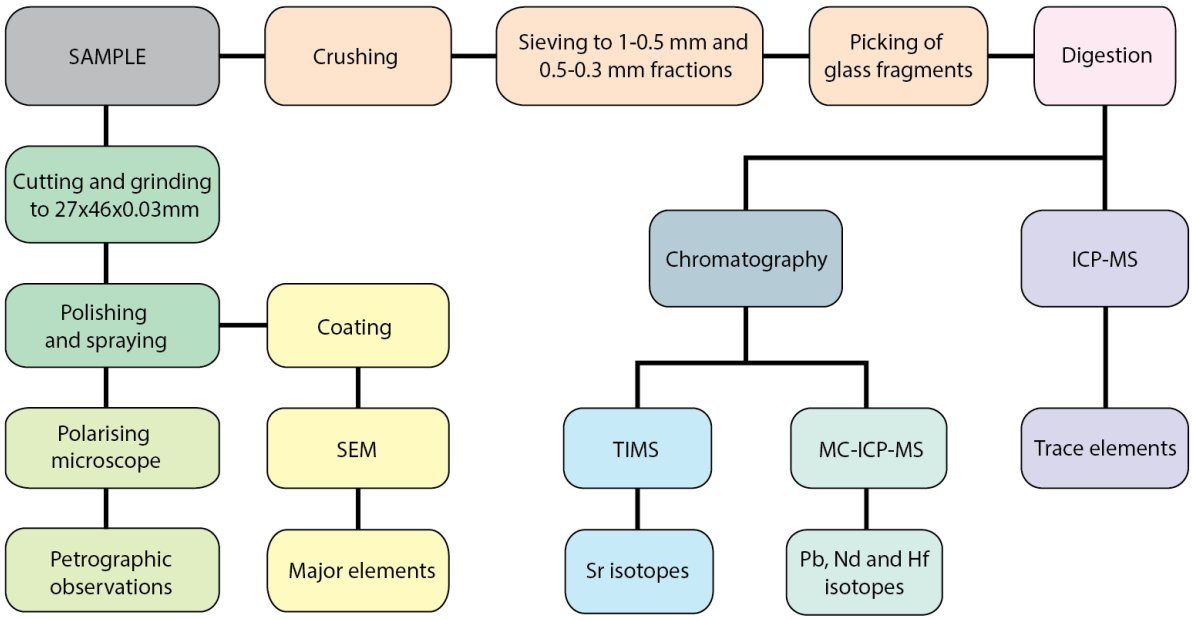

Figure 3.1: Simplified, schematic flow chart covering the sample preparation steps for the petrographic observations and the geochemical analyses performed during the study.

3.6 Seismic observations

As a supplement to the project, a brief interpretation of two 2-D seismic lines, NPD_MB-11-05 and MNR11-90369A, was performed during one of the visits at the Norwegian Petroleum Directorate (NPD) in Stavanger. The high quality lines were required in 2011 by the NPD and TGS respectively, and cover the Møre Marginal High and the westernmost part of the Møre Basin. NPD_MB-11-05 covers the drill site of 6403/1-U-1, and MNR11-90369A includes the exploration well 6403/6-1; the exploration well located closest to the study area. One known lithostratigraphic top (top Tang Formation) from the well was correlated to the study area.

4 Results

This chapter has been organised into four different subchapters. The first part addresses the description of the cored volcanic succession, and is followed by the petrographic observations of the different lithologies identified in the core. Thereafter, the results obtained from the geochemical analyses will be presented. Finally, the observations performed during the investigation of two seismic lines located over the study area, are addressed.

4.1 Core description

A simplified log of the volcanic succession in the core is presented in fig. 4.1, and a more detailed log is included in appendix A. The succession is essentially composed of two lithologies – massive basalt and hyaloclastite breccia. The entire succession seems to be affected by alteration, ranging from severe in the uppermost meter, to high in the upper ~20 m, and to typically high to moderate in the lower ~20 m of the core. The term hyaloclastite includes a variety of fragmented rock types derived from lava-water or lava-ice interactions. This study has therefore used the definition provided by Watton et al. (2013), where hyaloclastite is defined as the glassy material derived from passive quench fragmentation of coherent lava, with only mild explosive interactions.

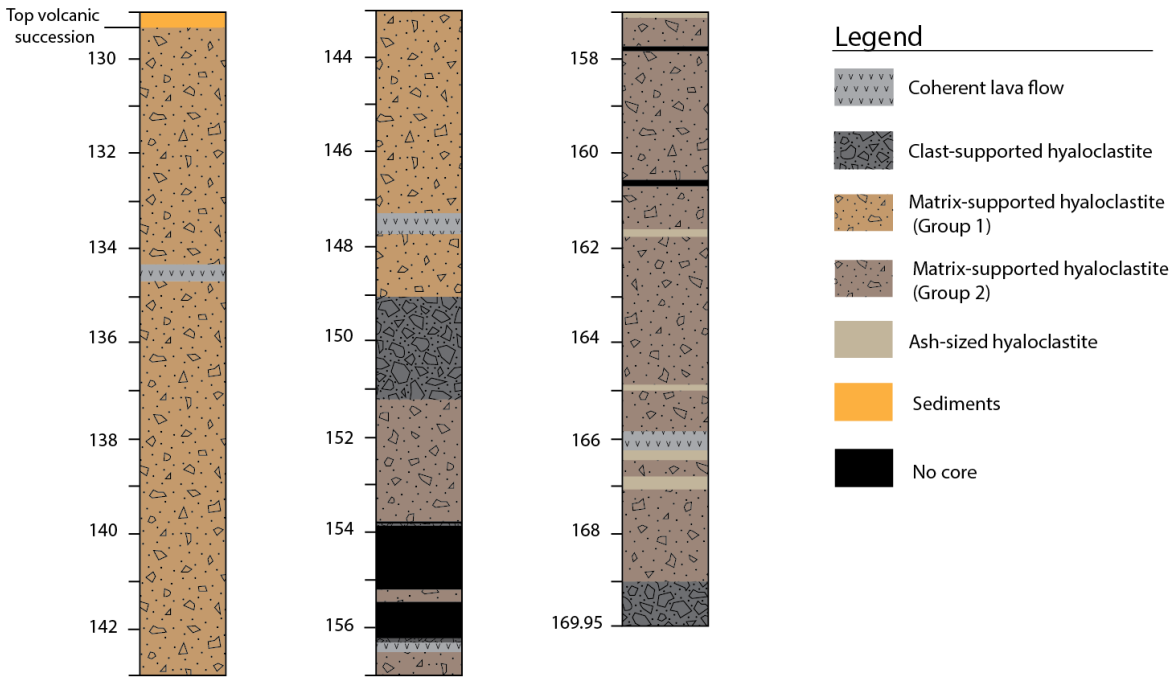

Figure 4.1: Simplified log of the volcanic succession in core 6403/1-U-1.

Different lithofacies have been proposed based on the coherence of the massive basalt, the amount of massive basalt versus hyaloclastite, and grain size. The brecciated hyaloclastite deposits have been divided into clast-supported hyaloclastite breccia, matrix-supported hyaloclastite breccia and fine-grained hyaloclastite ash. It is important to stress that the identified lithofacies represent different end-members, and some of the cored succession lies somewhere in between the different lithofacies, which will be described further.

4.1.1 Coherent lava flow

This lithofacies consists of coherent, massive and microcrystalline basalt (figs. 4.2A and 4.3A). The units of this lithofacies have a dark grey colour, are typically sparsely vesicular and phyric, and range from 20–40 cm in thickness. The vesicles are typically less than 1 mm, rounded, have a high sphericity, and are evenly distributed through the unit. The units are altered, and vesicles are filled in by calcite, zeolite and a green coloured clay mineral. Fractures are typically filled with calcite. The units are separated from the hyaloclastite breccia by irregular contacts. They typically "fill in" the underlying irregular contacts and display altered, glassy margins as upper contact. Some units show a concentration of bigger vesicles in the upper part; in these cases, the vesicles are rounded to elongated and are up to 2–3 mm in length.

4.1.2 Clast-supported hyaloclastite breccia

This lithofacies is characterised by >50% of massive basalt clasts in a matrix of coarse-grained hyaloclastite. The basalt clasts are angular to subangular, and are of the same characteristics as the coherent lava flow lithofacies. The clasts range from about 1–15 cm in diameter. Typically, the clasts have glassy margins and a fractured, closely spaced jigsaw-fit texture (fig. 4.3F). The matrix is composed of palagonite and minor sideromelane. In addition, the secondary minerals, mainly zeolites, a white amorphous mineral and minor calcite, are filling in intergranular spaces.

4.1.3 Matrix-supported hyaloclastite breccia

The units of this lithofacies are poorly sorted, and consist of isolated, massive basalt fragments in a matrix of hyaloclastite. Based on the nature of the massive basalt fragments, this lithofacies has been further divided into two groups.

Figure 4.2: Figure displaying the different lithofacies observed in the core. **(A)** Matrix-supported hyaloclastite breccia (Group 1) and coherent lava flow facies. Note the irregular upper contact between the units in the lower left part of the figure. **(B)** Matrix-supported hyaloclastite breccia grading into clast-supported hyaloclastite breccia (from right to left in the picture). (**C)** Fine-grained hyaloclastite ash (dark area to the upper left) grading into more coarse-grained, matrix-supported hyaloclastite breccia (Group 2). Note the dark indistinct lamination in the upper part of the unit.

Group 1

Within this group, two types of massive fragments are identified (fig. 4.3B). The first fragment type has the same characteristics as the coherent lava flow lithofacies. These fragments have a dark grey colour, and are angular to subangular, sparsely vesicular and phyric, and range in size from 2–12 cm. The second type of fragments has a slightly paler colour and is generally more altered than the first fragments type. They are more vesicular, slightly less crystalline and are typically rimmed by dark, altered glass. They are smaller (approximately 1–4 cm in size) and have a rounded to fluidal morphology. The hyaloclastite matrix is heavily altered and consists of devitrified glass fragments (palagonite) ranging from mm-scale up to about 1 cm, and intergranular secondary zeolite. Several filled sub-horizontal veins confirmed to consist of smectite and minor calcite by XRD-analysis, cut the units.

Group 2

This group contains basalt fragments with similar characteristics as the coherent lava flows in terms of being sparsely vesicular and phyric. However, these clasts are microcrystalline to glassy and have a sub-angular to fluidal outline (fig. 4.3D). Some of the clasts show inclusions of hyaloclastite and contain voids, either within or around, filled with secondary zeolite, a white amorphous mineral and/or pale green clay mineral. The clasts range in size from approximately 2–10 cm, where the degree of crystallinity decreases from the bigger to the smaller clasts. The glassy margins have a brown palagonite rim. The clasts are set in a matrix consisting of sideromelane and palagonite shards, ranging from mm-scale to approximately 1 cm in size. The secondary minerals zeolite, a white amorphous mineral and minor calcite are present as intergranular material in the matrix. The group is generally less altered than Group 1, and are typically highly to moderately altered (~40–90 vol%).

4.1.4 Fine-grained hyaloclastite ash

This lithofacies is fine-grained (ash-sized, i.e. <2 mm) and consists of massive and well-sorted hyaloclastite (fig. 4.2C). The units of this lithofacies are found in the lower ~13 m of the core (fig. 4.1), are typically heavily altered and range in thickness from around 5 to 20 cm. They generally show a gradual transition into the more coarse-grained, matrix-supported hyaloclastite lithofacies, and some units show indistinct lamination (fig. 4.2C).

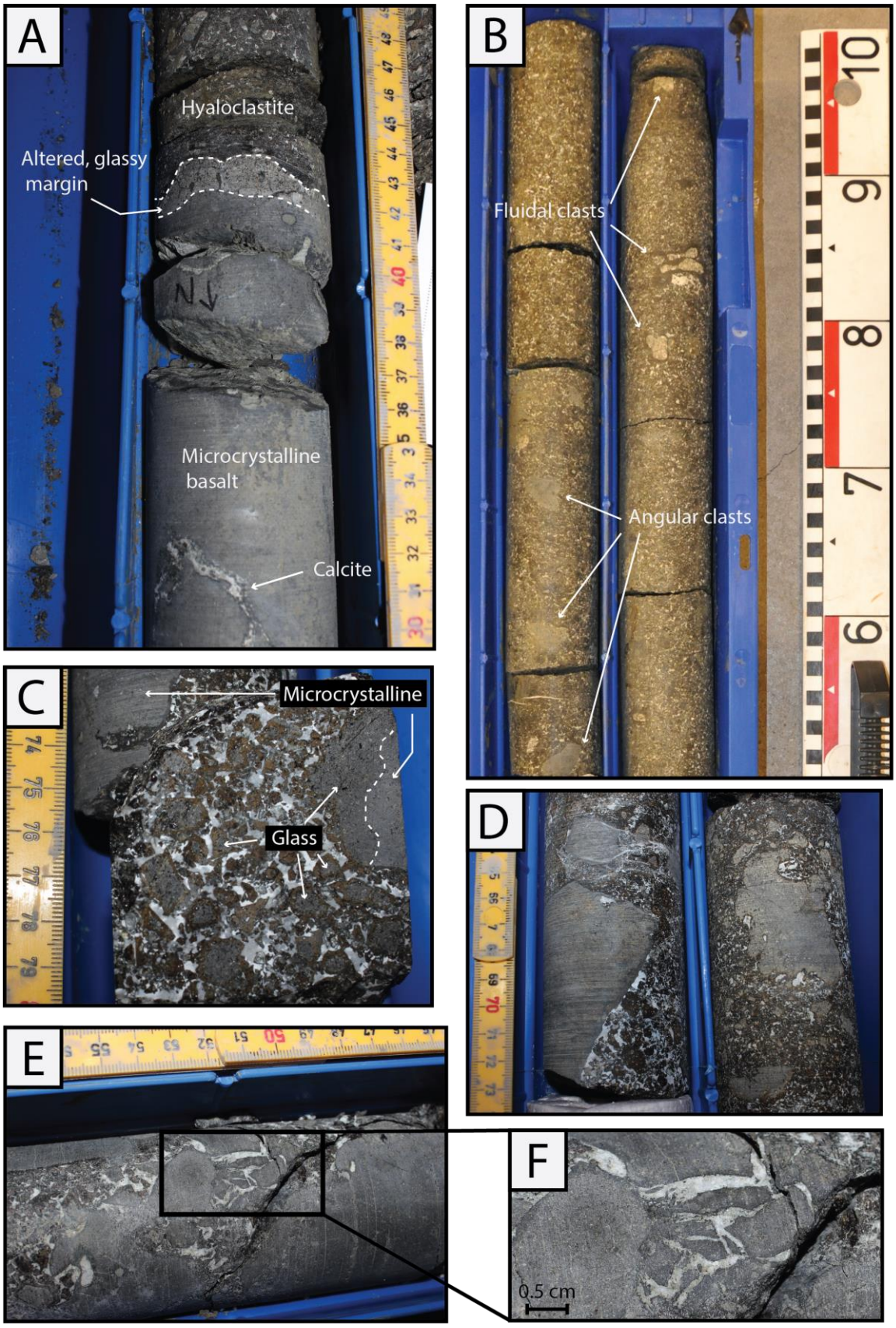
A
Hyaloclastite
Altered, glassy margin
Microcrystalline basalt
Calcite
B
Fluidal clasts
Angular clasts
C
Microcrystalline
Glass
D
E
F
0.5 cm

Figure 4.3 (previous page): Examples of key observations from the core. **(A)** Irregular boundary between matrix-supported hyaloclastite breccia (Group 1) and coherent lava flow lithofacies. **(B)** Two different types of isolated, basaltic clasts in a matrix of altered glass and intergranular secondary minerals (Group 1). **(C)** Close-up picture of matrix-supported hyaloclastite breccia (Group 2). Bigger clasts typically display glassy margins and a microcrystalline interior. Brown palagonite rinds rim the glassy margins, along with the matrix glass shards, and smaller glass shard are completely palagonitised. Intergranular secondary zeolite (pale grey-white) and a bright white amorphous mineral are present in the matrix. **(D)** Example of the variation in clast morphology and crystallinity of the Group 2 matrix-supported hyaloclastite breccia. **(E)** Clast-supported hyaloclastite breccia. **(F)** Close-up of black box in fig. E displaying closely spaced, so-called jigsaw-fit texture. Intergranular areas are filled by zeolite and minor calcite.

4.2 Petrographic observations

As indicated in the previous subchapter, the cored section essentially consists of two different lithologies; the hyaloclastite breccia and the massive microcrystalline basalt units and clasts. This section will address the petrographic observations of these lithologies.

4.2.1 Hyaloclastite (glass-breccia)

Five samples, C.10, C.20, C.21, C.28 and C.31, of this lithology were studied petrographically. Overall, the samples have the same petrographic characteristics. Although all samples show evidence of alteration, it varies in the degree. This is from samples with complete devitrification and abundant dissolution of glass shards (fig. 4.5A), to samples where cores of relatively fresh glass are still present (figs. 4.4A and 4.5C).

Texture

The hyaloclastite breccia is predominantly made up of volcanic glass shards. Fresh glass is observed in two samples (C.28 and C.31). The glass is clear and pale coloured in plane polarised light (PPL) and isotropic in cross polarised light (XPL). Therefore, it is termed sideromelane (e.g. McPhie et al., 1993). The glass shards are generally fractured. They are typically angular, and some show splinty edges. They have a porphyritic texture and are moderately phyric, with phenocrystals sitting in a groundmass of sideromelane glass and/or palagonite (fig. 4.4). The phenocrystals often occur in clusters, giving the rock a partly glomeroporphyritic texture. The glass shards are typically sparsely to non-vesicular, with a vesicle abundance up to ~1% of individual glass shards. The vesicles are rounded and have a high sphericity.

Primary minerals

Olivine, plagioclase and chrome-spinel are the primary minerals and phenocrystals identified in the hyaloclastite unit (fig. 4.4B). A distinct difference in size of the phenocrystals indicates two different generations formed at different stages and depths in the melt evolution.

Olivine represents the biggest, and thus the first generation of phenocrystals. They generally range from 0.1–0.8 mm and make up around 3–5% of the glass shards. The olivine crystals are euhedral to subhedral and often appear as glomerocrysts. Typically, they are fractured and contain chrome-spinel inclusion (figs. 4.4B and 4.4C). Less frequently, glass inclusions occur

in the olivine crystals (fig. 4.4C). The first generation of olivines in sample C.28 has a forsterite content of 83% (Fo_{83}).

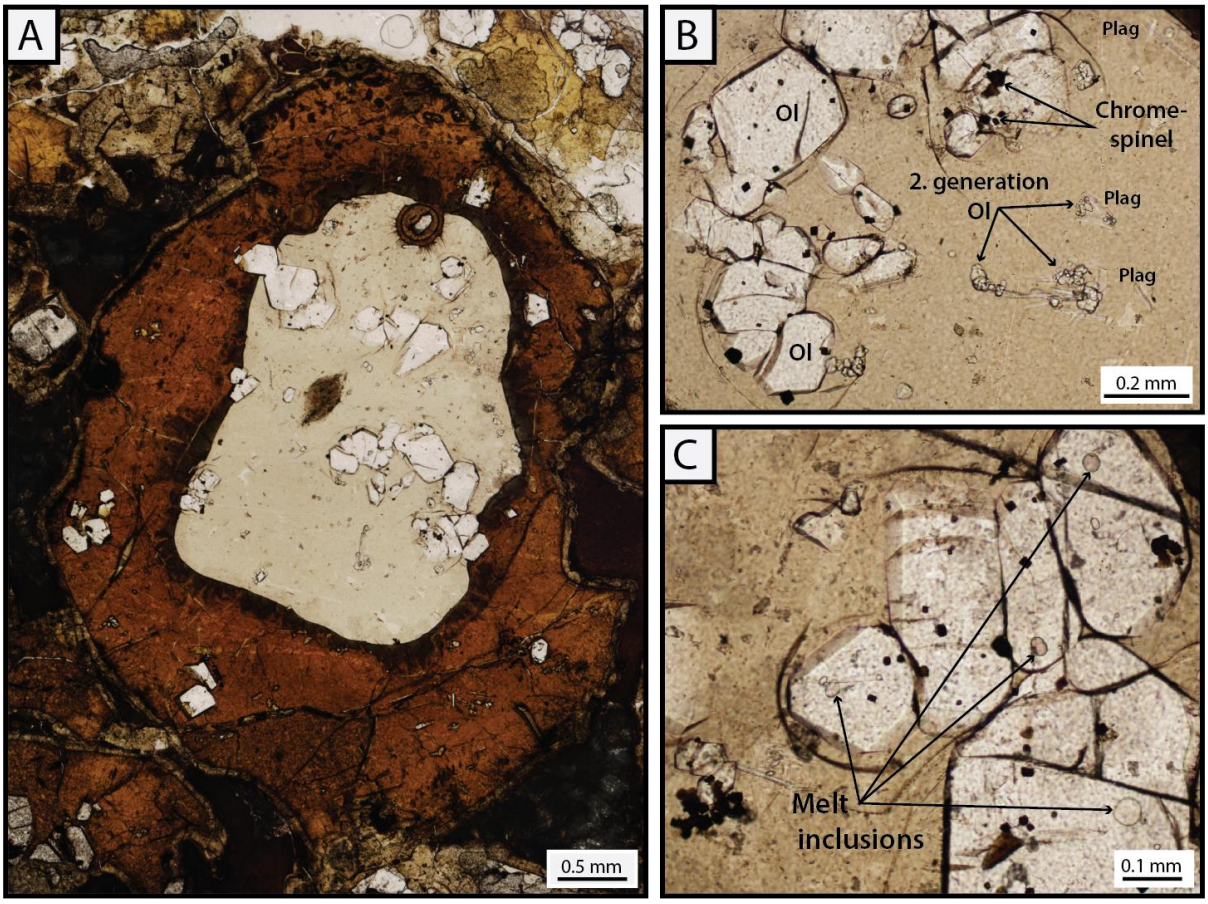

Figure 4.4: Photomicrographs illustrating the primary textural features and mineral assemblage present in the hyaloclastite unit. **(A)** Angular shard displaying a core of clear, pale coloured and relatively fresh sideromelane glass, rimmed by dark brown palagonite. Note the porphyritic and glomeroporhyritic texture of the unit, where phenocrystals are partly clustered and sitting in a groundmass of glass. **(B)** Close-up showing the primary minerals present in the unit. The first generation of phenocrystals are represented by big olivines (ol) containing opaque to dark brown chrome-spinel inclusion. The second generations of phenocrystals are considerable smaller and consist of olivine and plagioclase (plag). **(C)** Melt inclusions in first generation olivines. Note also the fractured nature of the crystals. All pictures are from sample C.28 and are taken in plane polarised light.

Smaller olivine phenocrystals are also observed in the samples, and are part of the second generation of phenocrystals (fig. 4.4B). They are typically less than 0.05 mm in size, have a euhedral to subhedral shape, and predominantly appear in glomerocrysts, often along with plagioclase. They constitute less than 1% of the glass shards, and have a chemical composition of Fo_{82} (sample C.28). This indicates that the second generation of phenocrystals are slightly more evolved than the first generation.

The plagioclase phenocrystals appear as laths, and typically vary in length from 0.03–0.2 mm. They have also a euhedral to subhedral morphology, constitute less than 1% of glass shards, and are part of the second generation of phenocrystals. The plagioclase composition in sample C.28 is An_{76}.

The chrome-spinel crystals are opaque to dark brown in PPL, have an equant shape and are typically around 0.01–0.03 mm. They constitute less than 1% of individual glass shards. Chrome-spinel appear as inclusions in the first generation of olivine phenocrystals and in the glass. In the glass, they often form separate clusters or are clustered around the second generation of phenocrystals (olivine and plagioclase).

Alteration characteristics and secondary minerals

Sideromelane is especially prone to alternation. Even in young sideromelane deposits, it has often altered to palagonite, resulting from low-temperature hydration and alteration of sideromelane (McPhie et al., 1993). Even in the samples containing relatively fresh sideromelane (C.28 and C.31), most of the glass fragments are completely palagonitised. Also sideromelane displays signs of some alteration, shown by the formation of palagonite around, and in, vesicles and fractures. In addition to palagonite, the secondary minerals observed in the rock are clays (chlorite and probably smectite), phillipsite (a zeolite) and calcite. An amorphous phase, high in Si and Ca, similar to what have been described as a Ca-silicate by Walton and Schiffman (2003), is also present. This study has therefore adopted this term for the amorphous phase.

Zonal rinds of palagonite always rim the sideromelane cores in C.28 and C.31, and the boundary between the sideromelane and the palagonite is abrupt (fig. 4.4A). Different colours indicate the zonal rinds, ranging from dark green closest to the sideromelane, to red-brown, which is the most abundant type of palagonite. The palagonite is slightly birefringent in XPL indicating that it at least consists of some crystalline material. Palagonite is also replacing vesicles and some phenocrystals. A pale-green to beige pore-lining rim is present at the margins of all shards, and is birefringent in XPL (fig. 4.5E). This indicates that it consists of a crystalline clay mineral, probably smectite (Walton and Schiffman, 2003). It is very likely that the different zones in the palagonite reflect different stages in the palagonite formation, starting from the edge of the shard, and moving inwards over time.

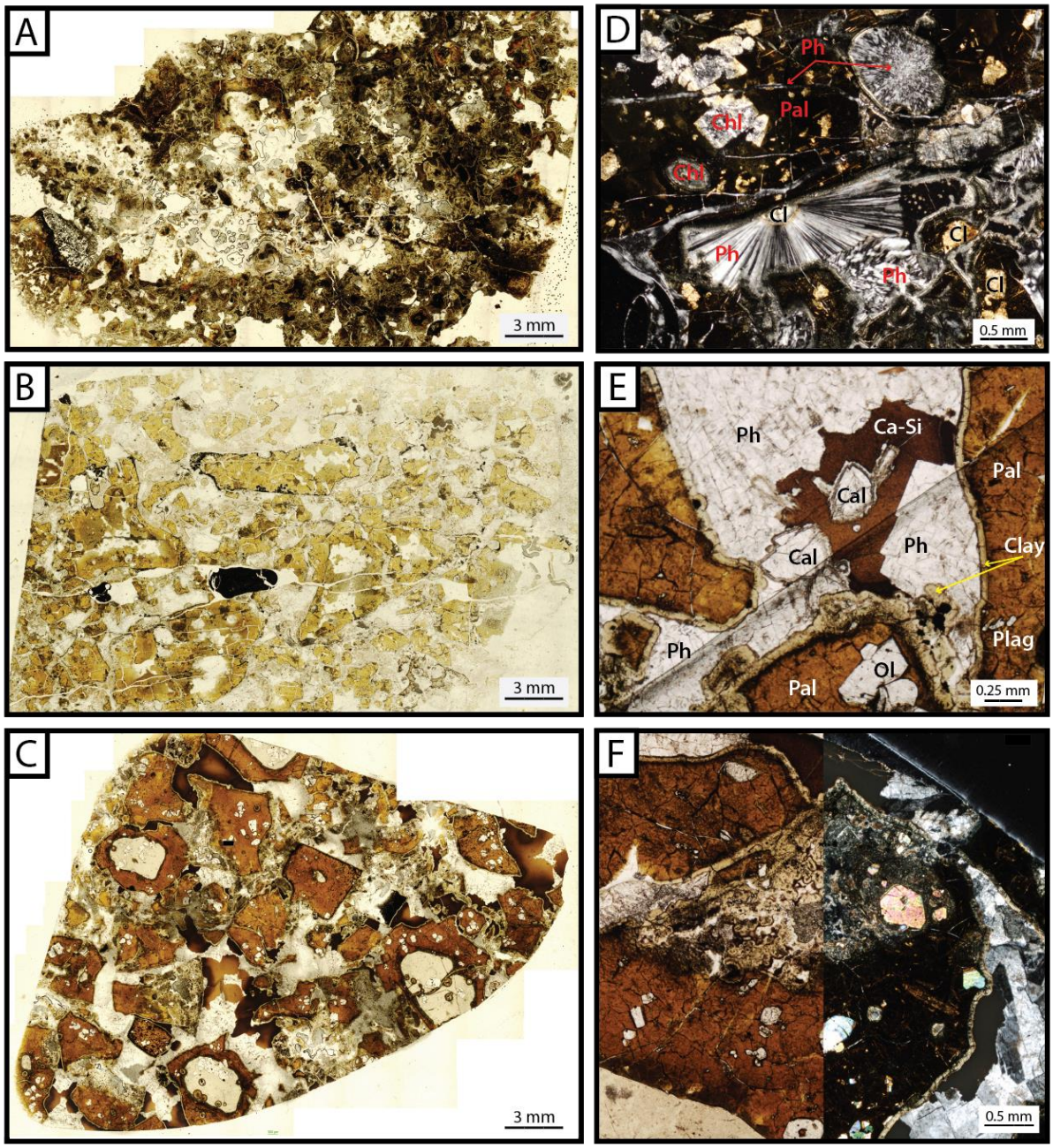

Figure 4.5: Photomicrographs describing the alteration features of the hyaloclastite unit. **(A)** Sample C.10 displaying complete alteration and dissolution of former glass shards. The alternation products consist of clays, Fe-hydroxides and intergranular zeolites. **(B)** Sample C.21 where all glass shards are palagonitised and partly dissolved (high grade of alteration). **(C)** Sample C.28 displaying four cores of relatively fresh sideromelane (pale beige) present in the bigger shards, rimmed by palagonite (brown). Note that smaller shards are completely palagonitised, but the phenocrystals are often relatively fresh (bright white crystals in palagonite). **(D)** Picture from sample C.21 showing the two different habits of phillipsite present in vesicles and intergranular areas. Chlorite and clays have replaced former olivine phenorystals. **(E)** Close-up of the secondary mineral assemblage from sample C.28. Primary olivine and plagioclase are also present. **(F)** Close-up of a partly dissolved glass shard, which has been replaced by clays of the same characteristics as the pore-lining clay, clearly shown by the change in birefringence. **A, B, C, E** and half of **F** are taken in PPL and **D**, and half of **F**, are taken in XPL. Pal: Palagonite; Ph: phillipsite; Chl: Chlorite; Cl: Clay; Cal: Calcite; Ca-Si: Ca-silicate; Ol: Olivine; Plag: Plagioclase.

For the more altered samples, all of the glass has undergone alteration (C.10, C. 20 and C.21). Sample C.10 are completely devitrified to Fe-hydroxides and clays, and the glass shards are partly or fully dissolved (fig. 4.5A). In sample C.20 and C.21, the glass shards are altered to palagonite (fig.4.5B). Some of the glass fragments have kept their original shapes, and some have partly or fully been dissolved and disintegrated. In this case, clay of the same characteristics as the pore-lining clay, found at the margins of shards in samples C.28 and C.31, have replaced the shards (fig. 4.5F). In sample C.21, the olivine phenocrystals have been replaced by clays (including chlorite) (fig. 4.5D), indicating more advanced alteration than the palagonite replacement of crystals which are seen in some areas in sample C.28 and C.31.

Phillipsite, Ca-silicate and minor calcite are found as intergranular and cementing secondary minerals in all hyaloclastite samples (fig. 4.5E), and phillipsite and clays are present in fractures and vesicles in shards. Phillipsite appears in two different habits, as radiating and fibrous spherulites, and as more blocky, prismatic crystals (fig. 4.5D). In many areas, intergrowth of spherulitic phillipsite and brown coloured clay occur. In this case, phillipsite is nucleating from a centre consisting of clay, close to margins of glass fragments (fig. 4.5D). This implies that the clay phase formed before phillipsite. The blocky phillipsite fills pores remaining after the formation of spherulitic phillipsite, clays and Ca-silicate. The Ca-silicate is characterised by a dark brown colour in PPL and XPL. It is often intergrown with phillipsite, resulting in irregular boundaries between the phases. Minor calcite is present and is typically associated with Ca-silicate (fig. 4.5E). The textural relationship between the phases indicates that calcite has formed after the Ca-silicate, by filling in the remaining pore space.

Based on the observations made for the secondary minerals, it is clear that the clay phase found at glass margins and in cores of spherulitic phillipsite probably formed first. This was followed by formation of spherulitic phillipsite, Ca-silicate, blocky phillipsite and calcite, respectively. All of these phases formed simultaneously with the palagonitisation process. More advanced alteration manifests as chlorite and clay replacement of phenocrystals and extensive dissolution of glass shards. This secondary mineral assemblage indicates that the hyaloclastite has undergone low-temperature alteration by seawater-rock interactions (e.g. Walton and Schiffman, 2003).

4.2.2 Microcrystalline, massive basalt

Three samples of this lithology have been petrographically studied (C.15, C.23 and C.34). Overall, they show the same characteristics, dominated by alteration. Fortunately, one sample (C.23) had a margin of relatively fresh sideromelane present. This made it possible to more precisely decide the primary mineralogy and texture of the massive basalts.

Texture

All samples have porphyritic and hypocrystalline textures, where phenocrystals sit in a groundmass of microliths and glass (fig. 4.6A). The phenocrystals occur often in clusters, giving the rock a partly glomeroporphyritic texture. The phenocrystal abundance varies from ~3 % (sample C.23) to ~10 % (sample C.34), making the rock moderately phyric, and not sparsely phyric, as apparent from the core description. The samples are sparsely vesicular (1–5% abundance), with generally rounded and highly spherical vesicles. The quality of the thin section of sample C.15 makes it hard to precisely determine the phenocrystals and vesicle abundance. In sample C.23, a variolitic zone marks the transition from sideromelane glass to the microcrystalline interior (fig. 4.6B). The varioles are characterised by brown areas in PPL, composing fan-like arrangements of fibres nucleating from a centre, often consisting of plagioclase laths (fig. 4.6C). The presence of varioles indicates very large undercooling during the emplacement of the rock (e.g. Fowler et al., 2002).

Primary minerals

The microcrystalline basalts have undergone alteration and, apart from the sideromelane margin of sample C.23, the only primary mineral that clearly can be identified in the samples is plagioclase. They occur as laths and are interlinked in the groundmass along with interstitial glass. They range typically between 0.1–0.25 mm in length, and show some flow alignment around phenocrystals and vesicles.

The bigger phenocrystals have been pseudomorphed by secondary minerals. However, their shape has been preserved, and based on their habit, they most likely represent former olivine crystals. The glassy crust of C.23 where fresh olivine is observed is confirming this. The olivines have a euhedral to anhedral shape and contain opaque inclusions. They can be divided into two different generations based on their size. The first generation range from 1.5–0.5 mm in diameter, whereas the second generation is typically less than 0.1 mm.

The fresh sideromelane crust of sample C.23 has the same characteristics as the fresh glass in the hyaloclastite samples (section 4.2.1). The crust contains plagioclase with An_{78}, and olivines with Fo_{84} (1.generation) and Fo_{83} (2.generation), all comparable to sample C.28.

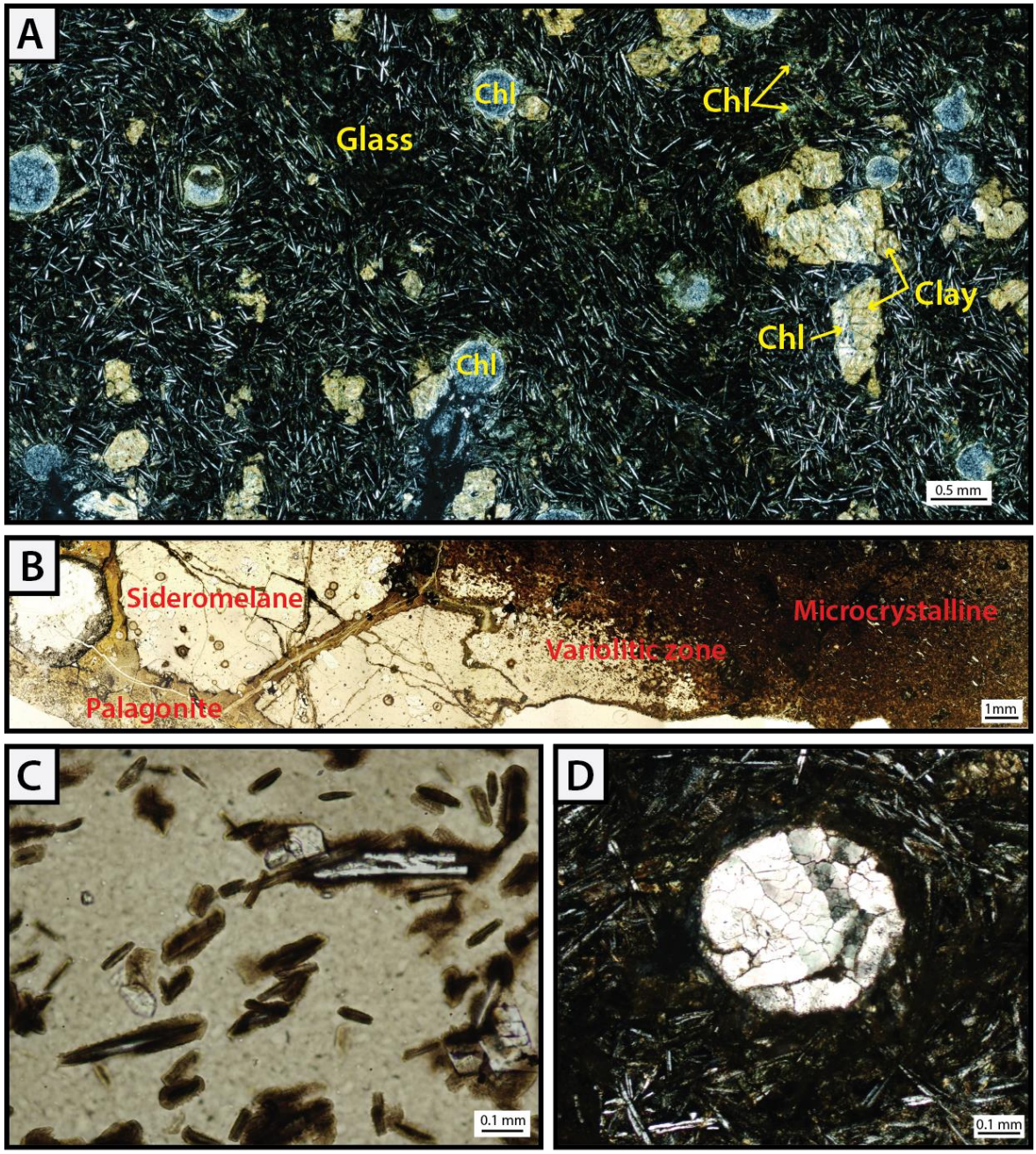

Figure 4.6: Mineralogy and characteristic features of the microcrystalline basalt unit. **(A)** Photomicrograph from sample C.34 displaying the porphyritic texture of the unit. Former olivine crystals, now replaced by chlorite and clays, are sitting in a groundmass of plagioclase laths and glass. The glass has partly altered to chlorite and clays. Chlorite is also present as vesicle fill. **(B)** Cross-section over sample C.23 showing the sideromelane margin, the microcrystalline interior and the transition marked by a variolitic zone. **(C)** Close-up of the varioltitc zone: dark brown varioles are present as radiating fibres, nucleating from plagioclase crystals. **(D)** Vesicle filled with calcite from sample C.34. Chl: Chlorite. **A** and **D** are taken in cross polarised light, **B** and **C** in plane polarised light.

This, along with the petrographic observations, indicates that the hyaloclastite and the microcrystalline basalt units are more or less similar chemically. They have most likely followed the same melt evolution and erupted from the same volcanic vent, but differ in the amount of undercooling when emplaced (apart from the glassy crust in sample C.23).

Alteration characteristics and secondary minerals

Clays, including chlorite, and calcite are the secondary minerals observed in the samples. Chlorite is partly or fully replacing vesicles, veins and parts of the groundmass in the rock, and is intergrown with clay in phenocrystals (fig. 4.6A). It has completely replaced the phenocrystals in the palagonite crust in C.23. Calcite fills a few vesicles in sample C.34 (fig. 4.6D). In these cases, chlorite and/or clay often rim the vesicles. This indicates that calcite formed after the chlorite and the clays. The clay minerals occur as very fine-grained aggregates, and have a brown-yellow colour in PPL in sample C.34. They mask most of the phenocrystals in sample C.15 and in the microcrystalline interior of C.23, making them appear nearly opaque when observed in the microscope. The clay mineral is rich in Mg, as expected; since it is replacing olivines rich in Mg. Clays (including chlorite) dominate the secondary mineral assemblage, indicating that the microcrystalline basalts have undergone low-temperature seawater alteration (e.g. Alt, 2004).

4.3 Geochemistry

4.3.1 Major Elements

In situ major element analysis was conducted for the three samples where fresh glass was observed from the petrographic observations (C.23, C.28 and C.31). To supplement the sparse amount of samples, it was decided to add analyses of melt inclusions present in the first generation of olivine phenocrystals in the samples as this could provide useful information on the melt evolution.

The *in situ* technique allows for spot analyses of small domains of fresh glass within the samples. Therefore, it should be noted that the data presented for the major elements are not entirely comparable to the trace element and isotope data presented later in the thesis. This is because the trace element and isotope data are based on hand picked glass from the samples where some of the picked pieces have undergone at least some alteration (see section 3.4 in Methods).

Due to the glassy nature of the samples, it is not possible to quantify their precise modal mineral content. The rocks have therefore been classified according to the chemical classification diagram by Le Bas et al. (1986), which is based on the total alkali versus silica content of rocks (TAS-diagram) (fig. 4.7). All samples plot within the basalt field in the diagram, and there is minor variation in the composition of the samples, and in the composition of the matrix glass and the melt inclusions. This indicates that the cored volcanic succession is more or less indistinguishable chemically, as there seem to be no, or only minor, variation related to different depths or lithologies.

Figure 4.7 also shows the studied samples plotted in the TAS-diagram from Irvine and Baragar (1971). This diagram distinguishes between alkaline and tholeiitic (subalkaline) rocks. As seen in the diagram, all samples plot below the alkaline–tholeiitic division line, clearly classifying the rocks as tholeiites.

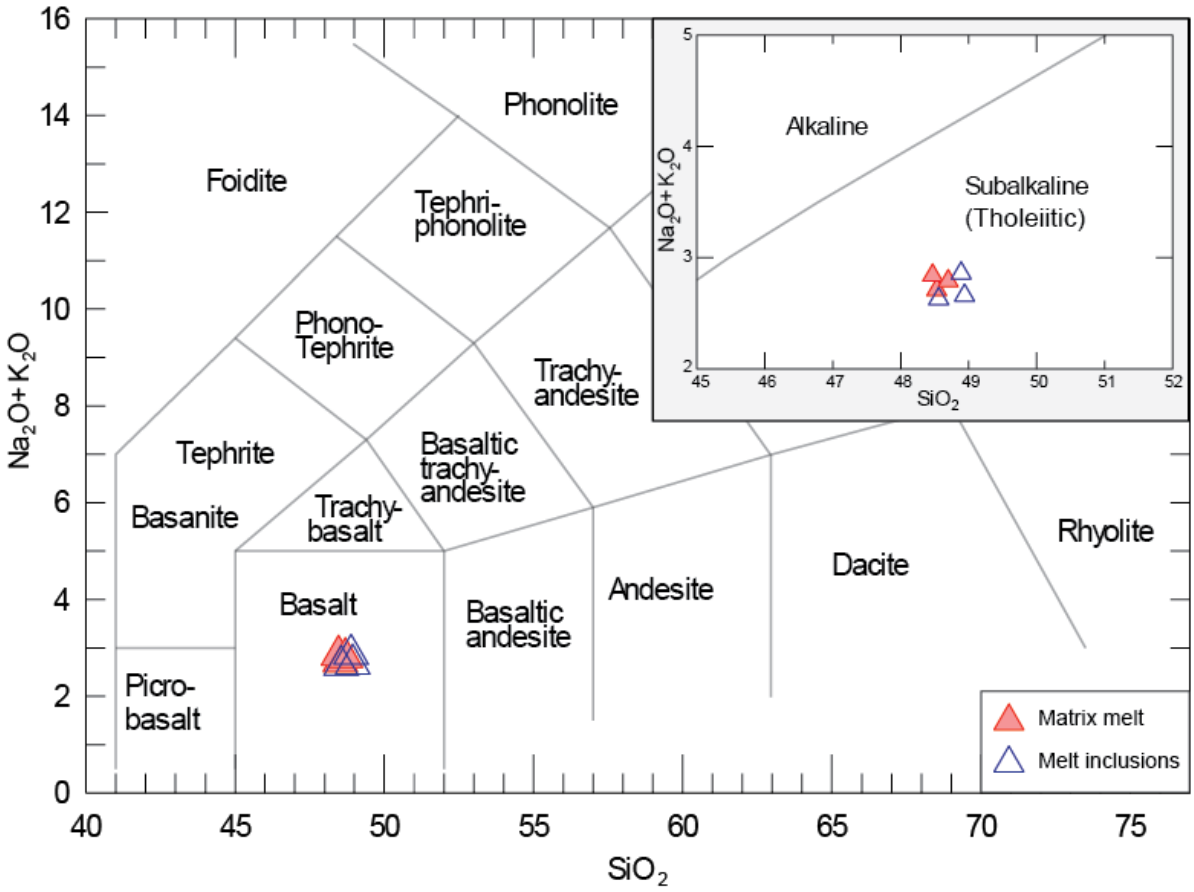

Figure 4.7: Total alkali versus silica (TAS) diagram from Le Bas et al. (1986) and from Irvine and Baragar (1971) (upper right corner). All samples and melt inclusions plot within the basalt field, and there is no significant chemical variation in the samples, and matrix glass and melt inclusions. The samples are clearly classified as tholeiites, as all samples plot below the alkaline–tholeiite division line.

Variation diagrams provide a chemical signature of magmatic differentiation as the chemical composition of a melt will evolve with time as a result of removal or addition of different mineral phases (Sen, 2014). Olivine is usually the first mineral to crystallise from a melt and its formation will deplete the melt in MgO. Therefore, MgO is a useful marker for differentiation, and is here plotted against eight major element oxides for the matrix melt and melt inclusions (fig. 4.8). During progressive crystallisation from a basaltic magma, the concentration of CaO, MgO and Al_2O_3 will typically decrease as they enter the early crystallising mineral phases. On the other hand, it is expected that SiO_2, TiO_2, FeO* (total iron as FeO), MnO, Na_2O and K_2O will increase during progressive crystallisation. In order to estimate how evolved the samples are, the data have also been plotted along with tholeiitic mid-ocean ridge basalt from the Northeast Atlantic Ocean.

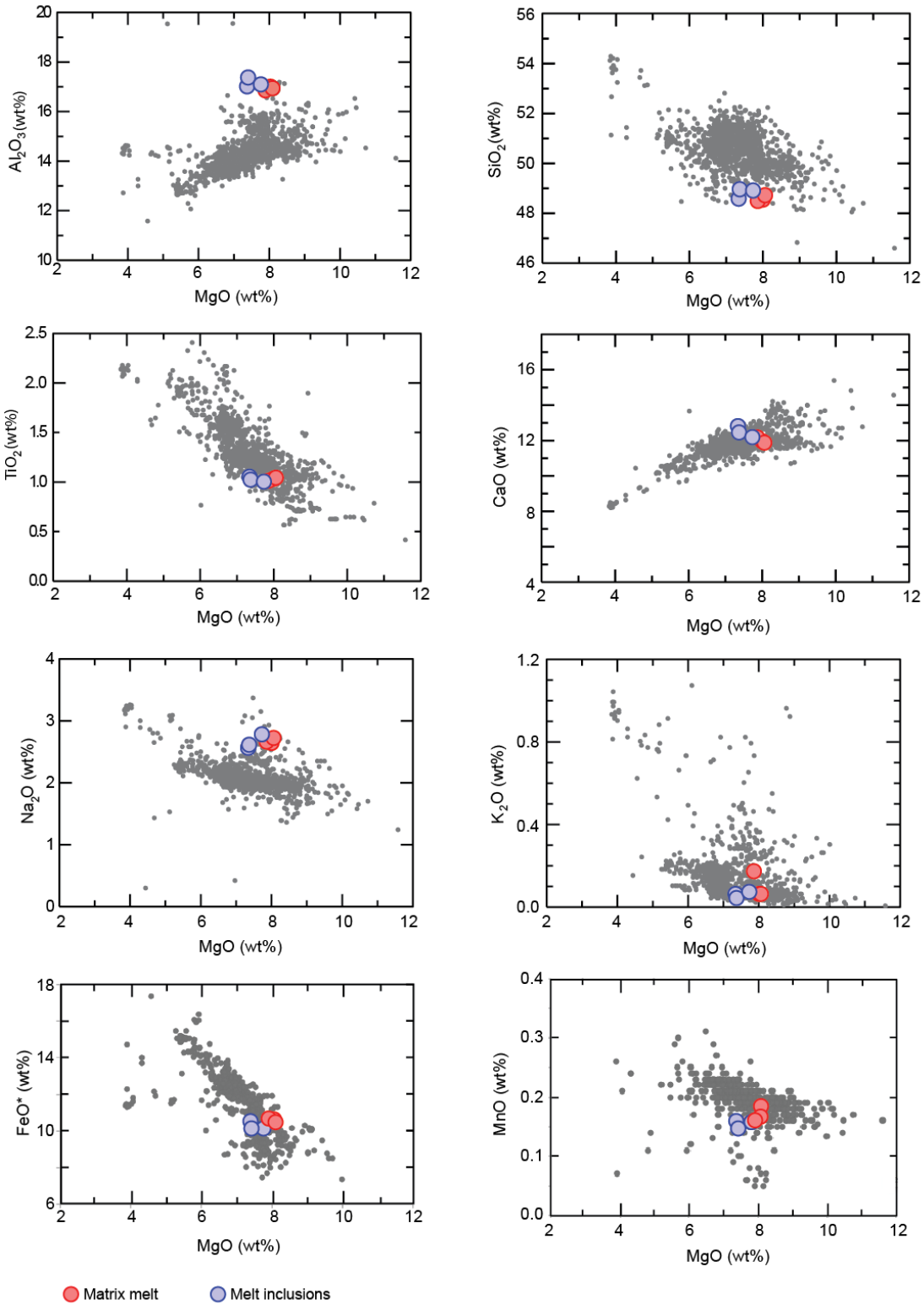

Figure 4.8: Various major oxides versus MgO. Background data: Northeast Atlantic MORB (data retrieved from the PetDB petrological database). All samples and melt inclusions plot within the tholeiiitc differentiation trend.

It is also evident from fig. 4.8 that there is little variation in the chemistry of the samples, and between the matrix glass and the melt inclusions. The matrix glass and the melt inclusions in the samples have MgO concentrations ranging from 7.88–8.08 wt% and 7.36–7.75 wt%, and Mg-number (molar $Mg/(Mg+Fe^{2+})$) ranging from 57–58 and 56–58, respectively. This indicates that neither the matrix melt nor the melt inclusions are in equilibrium with typical peridotite mantle sources (Mg-number>70 (Sen, 2014)). Therefore, the samples do not represent primary melts derived from direct melting of the mantle source. The samples have typical MORB compositions (Mg-number=55±7.6 wt% (Klein, 2003)). However, the samples display relatively low SiO_2 concentrations (48.47–48.70 wt% and 48.56–48.94 wt% for the matrix melt and melt inclusions respectively) and low TiO_2 concentrations (1.01–1.04 wt% and 1.00–1.05 wt% for the matrix melt and melt inclusions respectively). In addition, the samples show relatively low FeO* concentrations (10.45–10.66 wt% and 10.12–10.50 wt% for the matrix melt and melt inclusions respectively) and high Al_2O_3 concentrations (16.83-16.98 wt% and 16.99–17.35 wt% for the matrix melt and melt inclusions respectively). This indicates that the samples are intermediate to slightly primitive in the Northeast Atlantic MORB-evolution trend (fig. 4.8).

Even though there is little chemical variation between the matrix melt and the melt inclusions, minor differences exist between them. It is expected that the melt inclusions represent magma which is less evolved than the matrix glass. It is therefore contradicting that the melt inclusions all have lower MgO concentration than the matrix glass (fig. 4.8). This feature can be related to post-entrapment processes, and diffusive Mg-exchange between the inclusion and the host olivine crystal (e.g. Newcombe et al., 2014). Originally, the MgO concentrations of the inclusions were likely similar, or possibly higher, than in the matrix melt. This is supported by the fact that the inclusions generally have slightly higher CaO and Al_2O_3 concentrations than the matrix glass. This can represent plagioclase crystallisation, agreeing with the observation of plagioclase phenocrystals in the matrix melt.

4.3.2 Trace Elements

Trace elements can be divided by their relative affinity for crystalline minerals or the melt phase, during partial melting of the mantle and subsequent fractional crystallisation processes. Incompatible elements represent elements that have affinity for the melt, rather than the crystalline mantle minerals during such processes. Compatible elements, on the other hand, are preferentially incorporated in the crystalline minerals than the melt. Thus, incompatible elements have been proved to be useful "fingerprints" when distinguishing different types of basalts, as their abundances vary along with their mantle source (e.g. Hofmann, 2003).

As part of this study, handpicked glass chips from six samples (C.18, C.20, C.23, C.28, C.31 and C.33) were analysed for trace elements. The chondrite-normalised diagram for the rare earth elements (REE) of the samples is displayed in fig. 4.9A. Here, the relative incompatibility of the elements increases from the right to the left (from Lu-La). As shown in the diagram, there is little variation between the samples, as the REE patterns are more or less parallel to each other. The samples show a flat pattern for the heavy REEs (HREEs) an increase in the middle REEs, followed by a depletion of the lightest and most incompatible REEs (LREEs), shown as a slightly concave downward REE pattern. One exception is sample C.33, which shows an increase in the most incompatible REEs.

The samples in fig. 4.9A are also compared to the compositions of average "normal" MORB (N-MORB) and "enriched" MORB (E-MORB), from Sun and McDonough (1989), to easier establish their mantle source. N-MORBs are characterised by depleted LREE patterns and are interpreted to derive from depleted mantle sources. E-MORBs, on the other hand, are characterised by enriched LREE patterns, and can be generated by melting of enriched mantle sources or by low degrees of melting. Samples C.18, C.20 and C.23 show typical N-MORB patterns for the LREE, where C.18 and C.20 are slightly more depleted in the most incompatible LREEs compared to average N-MORB composition. Samples C.28, C.31 and C.33 have LREE patterns lying between average N-MORB and E-MORB. Samples C.28 and C.31 are characterised by chondrite-normalised REE pattern that are slightly enriched in LREEs compared to the N-MORB pattern, whereas sample C.33 seems to be considerably more enriched in LREEs, and are lying closer to typical E-MORB patterns.

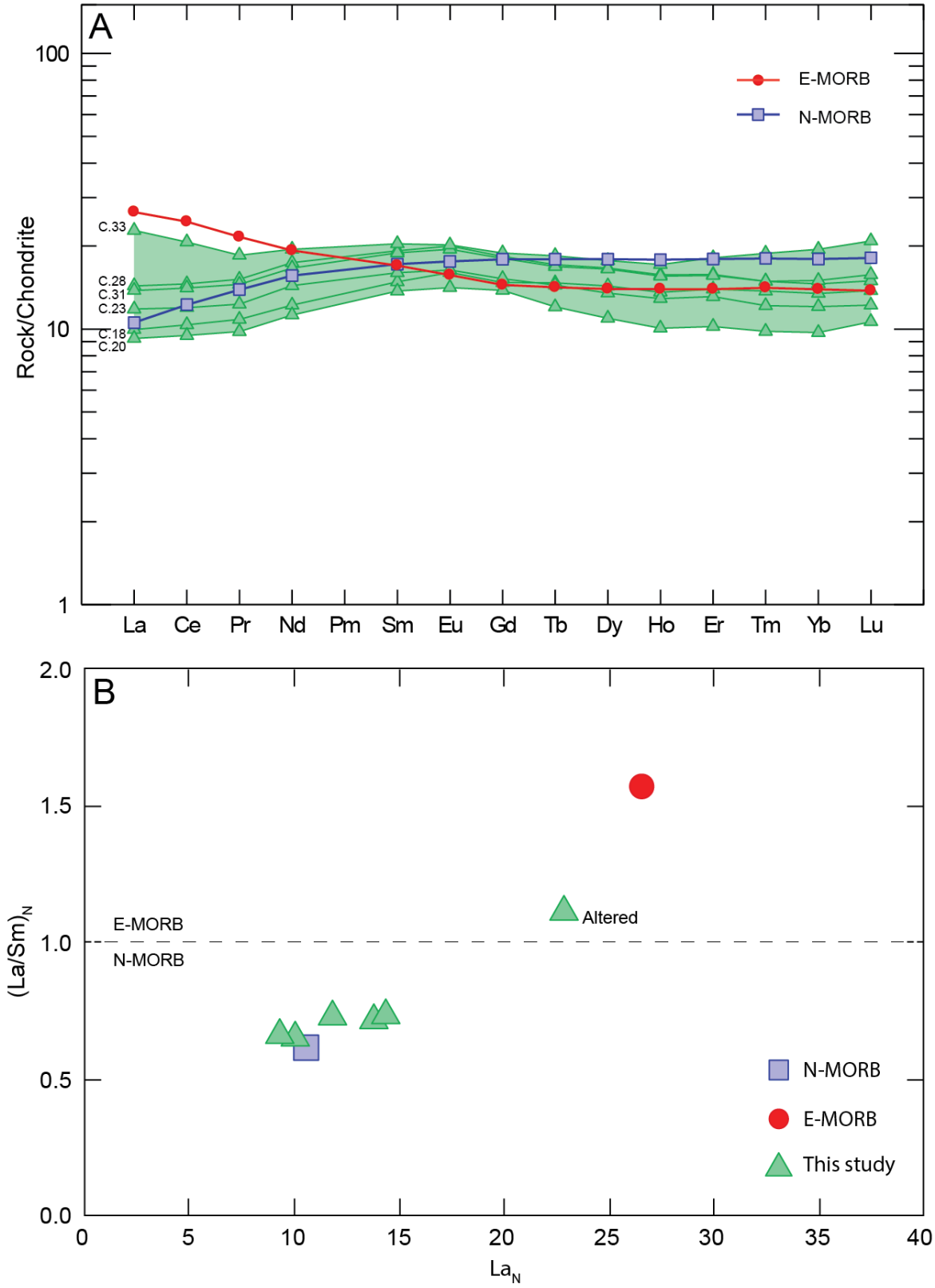

Figure 4.9: (A) Chondrite-normalised diagram showing the REE abundances of the samples of this study (marked in green). **(B)** Chondrite-normalised La/Sm $(La/Sm)_N$ versus La (La_N) plot. All samples except C.33 plot below the N-MORB–E-MORB division line, indicating a typical N-MORB source for the samples of this study. The average N-MORB and E-MORB compositions and the normalising values for both diagrams are from Sun and McDonough (1989).

By addressing the chondrite-normalised La/Sm-ratio ($(La/Sm)_N$) of the samples, their mantle source become clearer (fig. 4.9B). The $(La/Sm)_N$ ratio can be used as an indicator for mantle source, as N-MORB are typically defined by $(La/Sm)_N<1$, and E-MORB by $(La/Sm)_N>1$ (Arevalo and McDonough, 2010). Samples C.18, C.20, C.23, C.28 and C.31 have $(La/Sm)_N$ ratios ranging from 0.67–0.75 (fig. 4.9B), pointing to a LREE depleted N-MORB source. In contrast, sample C.33 has a $(La/Sm)_N$ ratio of 1.12, indicating a more enriched source. However, this enrichment is probably not primary, as this sample is regarded as the most altered one (see section 3.4 in Methods). It is therefore more likely that the enrichment of the LREEs is the result of seawater alteration. This is because it is known that the most mobile REEs, such as La, Ce and Pr, can enrich volcanic glass during seawater-rock interactions (e.g. Jochum and Verma, 1996).

The fact that all samples show relatively flat HREE patterns ($(Dy/Lu)_N$ ratios from 0.85–1.11) indicates that the melts are not derived from deep melting of a source with residual garnet, as the HREEs are retained in garnet and melting of such a source results in melts depleted in HREEs (e.g. Hirschmann and Stolper, 1996). Thus, the formation of the melts must have occurred above the spinel-garnet transition in the mantle (depths <85 km) (Robinson and Wood, 1998).

The primitive mantle-normalised diagram for trace elements is shown in fig. 4.10, where the samples are plotted along with average N-MORB and E-MORB compositions from Sun and McDonough (1989), and the composition of the upper continental crust from Rudnick and Gao (2014). Also in this diagram, the incompatibility of elements increases from the right to the left. The samples show typical MORB compositions for the most compatible trace elements (Lu–Sm), where some samples seem to be slightly less depleted than average MORB. The pattern for the most incompatible elements (Cs–Ce) is very scattered, partly lying in between average N-MORB and E-MORB compositions.

It is evident from the diagram that all samples show a relative enrichment of Pb, Th and U, and a relative depletion of Nb and Ta, compared to average N-MORB composition. These features can be correlated to the trend of the upper continental crust which may suggest that the melts have undergone assimilation of crustal material (fig. 4.10) (e.g. Hofmann, 1997). These features could also, however, be caused by post-emplacement seawater-rock

interactions. All samples display varying degrees of enrichment or depletion of the most incompatible elements (Cs–U). These elements, along with Pb, are very susceptible to mobilisation during alteration (Verma, 1992). Thus, the higher enrichment in Cs, Rb, Th and U, and the depletion of Ba, seen in the most altered samples (C.18, C.20, C.33), but also partly in C.31, compared to sample C.28 and C.31, is most likely an alteration feature.

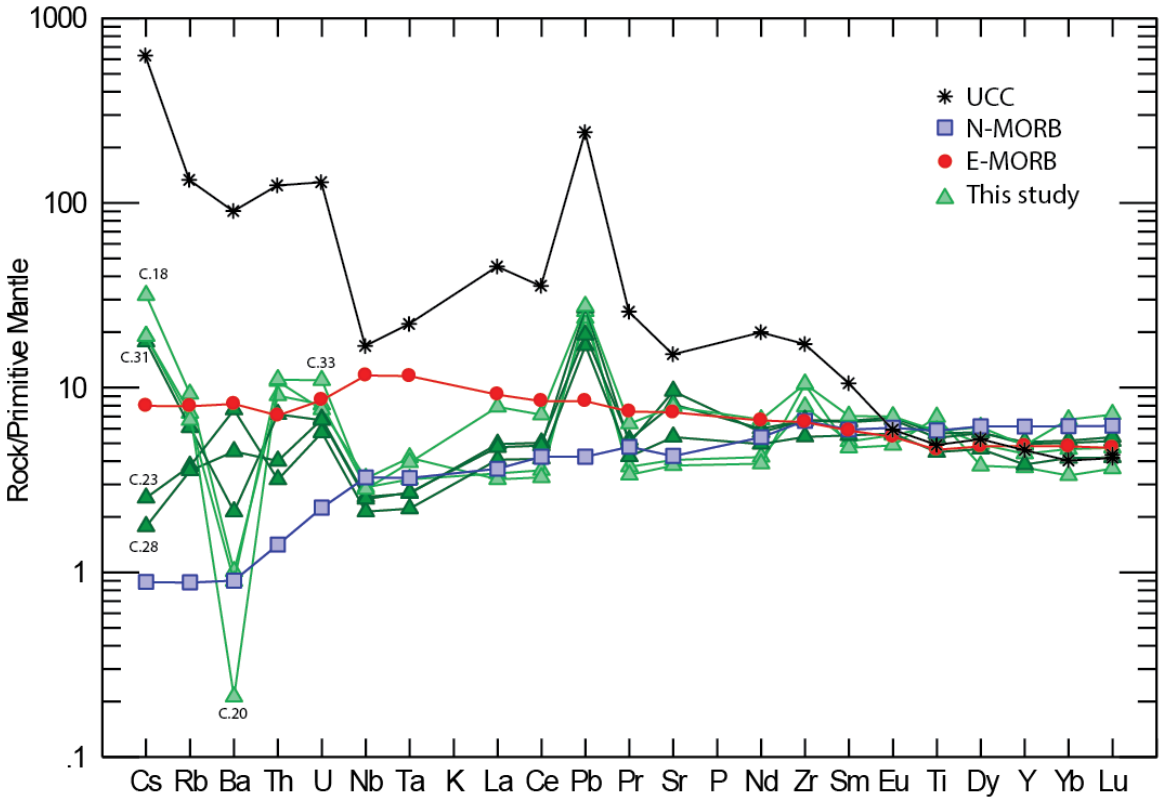

Figure 4.10: Primitive mantle-normalised diagram displaying the trace element abundances for samples of this study. The samples that are considered to be relatively fresh (C.23, C.28 and C.31) are in dark green; whereas the more altered samples (C.18, C.20 and C.33) are in pale green. Note that values for potassium (K) and phosphorous (P) are not included. Average N-MORB and E-MORB compositions, and normalising values, are from Sun and McDonough (1989), and the composition of the upper continental crust (UCC) from Rudnick and Gao (2014).

4.3.3 Isotopes

Isotopes of heavy elements do not fractionate significantly during magmatic processes. Radiogenic isotope ratios are therefore a unique tool to study the source characteristics for magmatic melts. This subchapter will address the results for the $^{87}Sr/^{86}Sr$, $^{143}Nd/^{144}Nd$, $^{176}Hf/^{177}Hf$, $^{206}Pb/^{204}Pb$, $^{207}Pb/^{204}Pb$ and $^{208}Pb/^{204}Pb$ composition for six samples (C.18, C.20, C.23, C.28, C.31 and C.33).

The isotopic compositions are presented in fig. 4.11 and listed in appendix F. In fig. 4.11 the results are plotted along with the trend for Northeast Atlantic MORB, which range from depleted to more enriched MORB compositions. The samples of this study show a wide range in the $^{87}Sr/^{86}Sr$ ratio (from 0.704380–0.707950). The samples, which have suffered the most alteration, C.18, C.20 and C.33, have the highest ratios of 0.707443, 0.707950 and 0.707362 respectively, and approach the $^{87}Sr/^{86}Sr$ ratio of seawater (~0.709) (e.g. Kruber et al., 2008). This alteration effect is indicated as a straight line in fig. 4.11A.

The samples show a narrower range in the $^{206}Pb/^{204}Pb$, $^{207}Pb/^{204}Pb$ and $^{208}Pb/^{204}Pb$ ratios (from 17.9140-18.2541, 15.5197-15.5298 and 37.8717-38.2554 respectively). There seem to be no clear increase, or decrease, in the ratios of the more altered samples (C.18, C.20 and C.33) compared to the samples that have suffered noticeably less alteration (C.23, C.28 and C.31). The $^{208}Pb/^{204}Pb$ versus $^{206}Pb/^{204}Pb$ plot shows a good correlation (fig. 4.11D). This is also the case for the $^{207}Pb/^{204}Pb$ versus $^{206}Pb/^{204}Pb$ plot, except for one sample (sample C.23) (fig. 4.11C). All samples have a systematically higher $^{208}Pb/^{204}Pb$ and $^{207}Pb/^{204}Pb$ ratios for a given $^{206}Pb/^{204}Pb$ ratio compared to the Northeast Atlantic MORB.

There is a very limited variation in the $^{143}Nd/^{144}Nd$ and $^{176}Hf/^{177}Hf$ ratios of the samples, ranging from 0.512824–0.512833 and 0.283111–0.283120, respectively (fig. 4.11B). Both the $^{143}Nd/^{144}Nd$ and $^{176}Hf/^{177}Hf$ ratios are low and comparable to the lowermost values (enriched end) of the compositions for the Northeast Atlantic MORB. This indicates that the samples are either derived from an enriched mantle source, or that the magma has experienced contamination and enrichment subsequent to melt formation by the continental crust, forming a source that has lower $^{143}Nd/^{144}Nd$ and $^{176}Hf/^{177}Hf$ ratios than the typical MORB source.

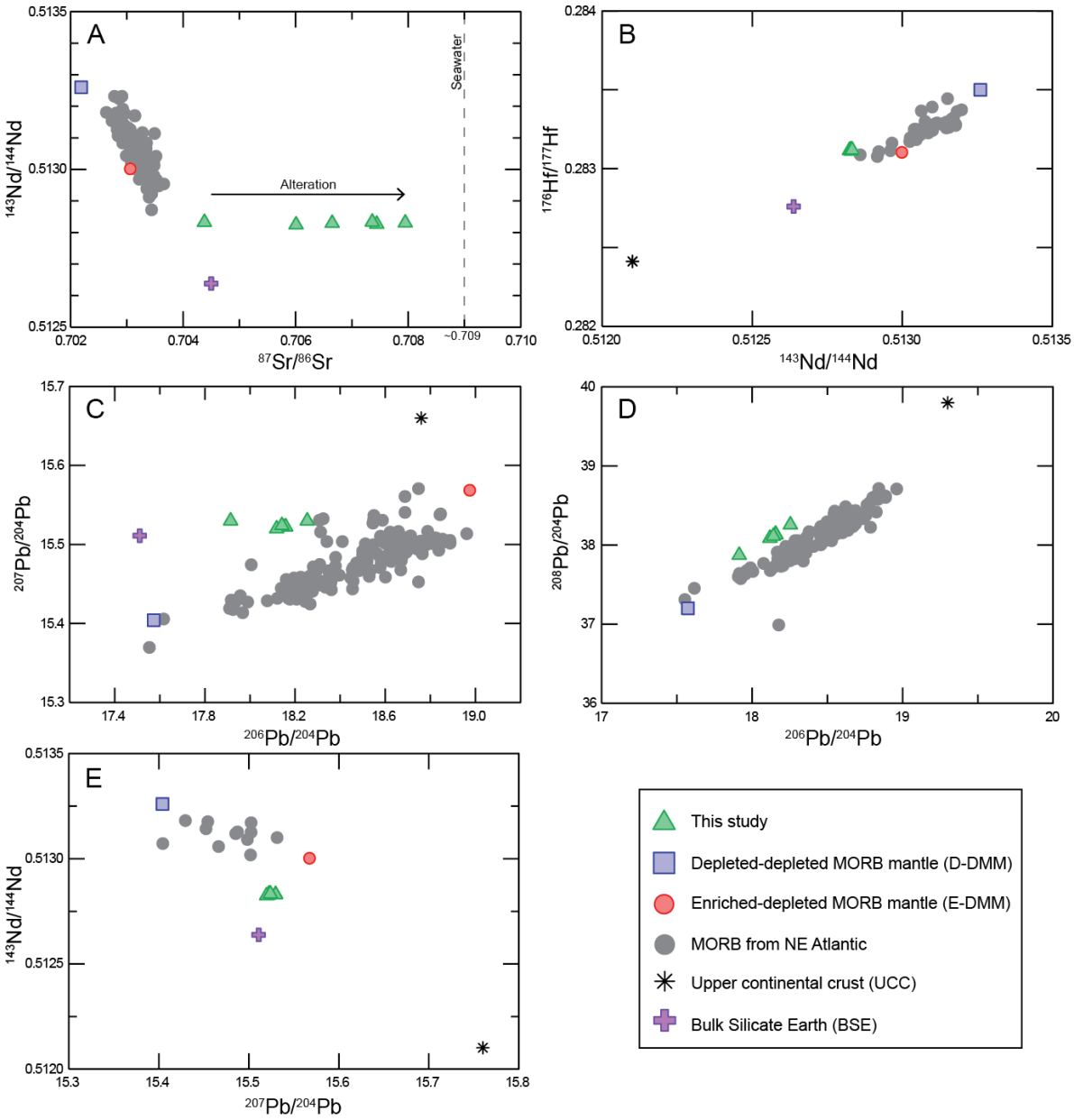

Figure 4.11: (A) $^{87}Sr/^{86}Sr$ vs. $^{143}Nd/^{144}Nd$, **(B)** $^{143}Nd/^{144}Nd$ vs. $^{176}Hf/^{177}Hf$, **(C)** $^{207}Pb/^{204}Pb$ vs. $^{206}Pb/^{204}Pb$, **(D)** $^{208}Pb/^{204}Pb$ vs. $^{206}Pb/^{204}Pb$ and **(E)** $^{143}Nd/^{144}Nd$ vs. $^{207}Pb/^{204}Pb$ diagrams for the samples of this study. The data are plotted along with MORB from the Northeast Atlantic (data retrieved from the PetDB petrological database). The BSE, D-DMM and E-DMM ratios are from Workman and Hart (2005), and the $^{208}Pb/^{204}Pb$ ratio for D-DMM are from Salters and Stracke (2004), where it is termed Extreme D-MORB. The UCC values in fig. 4.11B and the UCC $^{143}Nd/^{144}Nd$ ratio in fig. 4.11E are from Chauvel et al. (2014) and the UCC ratios in figs. 4.11C and 4.11D are from Newsom et al. (1986) and Asmerom and Jacobsen (1993), respectively. The $^{207}Pb/^{204}Pb$ ratio in 4.11E is from Asmerom and Jacobsen (1993).

4.4 Seismic observations

In order to get a better understanding of the emplacement history of the drilled lava delta succession, two seismic lines that are located over, and in the vicinity of, the drill site have been studied to supplement to the petrological and geochemical findings of the study.

4.4.1 Observed volcanic units

Below the thin cover of Eocene–Present sediments, three volcanic seismic facies units have been identified; the landward flows, lava delta and inner flows. The three facies units are all associated with the Faeroe-Shetland Escarpment (fig. 4.13), and have previously been described in literature (e.g. Planke and Alvestad, 1999; Planke et al., 2000; Berndt et al., 2001; Abdelmalak et al., 2016). Subparallel reflectors overlaying the lava delta characterise the landward flows. The lava delta is identified as prograding clinoforms and disrupted reflectors. The inner flows are identified below and landward of the lava delta, and are characterised by chaotic and disrupted, subparallel reflectors. The boundary between the lava delta and inner flows is generally hard to identify and is therefore marked with a dashed line in fig. 4.13. This is also the case for their lateral boundary, indicated by an overlap of the colour codes in the figure.

4.4.2 Emplacement of the volcanic units

Figures 4.12 and 4.13 show that the volcanic succession builds out from west to east. The lava delta terminates at the escarpment, indicating that the escarpment represents the paleo-shoreline at the time of emplacement. There appears be a lateral continuity between the lava delta and inner flows which may indicate that these units have formed simultaneously.

4.4.3 Time of emplacement

The sediments immediately overlying the lava delta in the drill hole 6403/1-U-1 are of an Early Eocene age (55 Ma) (see Introduction), thus representing the minimum age of the volcanic succession. In order to make further constrains on the time of emplacement, a correlation from the well 6403/6-1 to the study area was preformed for one horizon of known age, namely the top Tang Formation, which corresponds the latest Paleocene (~56 Ma) (Dalland et al., 1988; NPD, 2014).

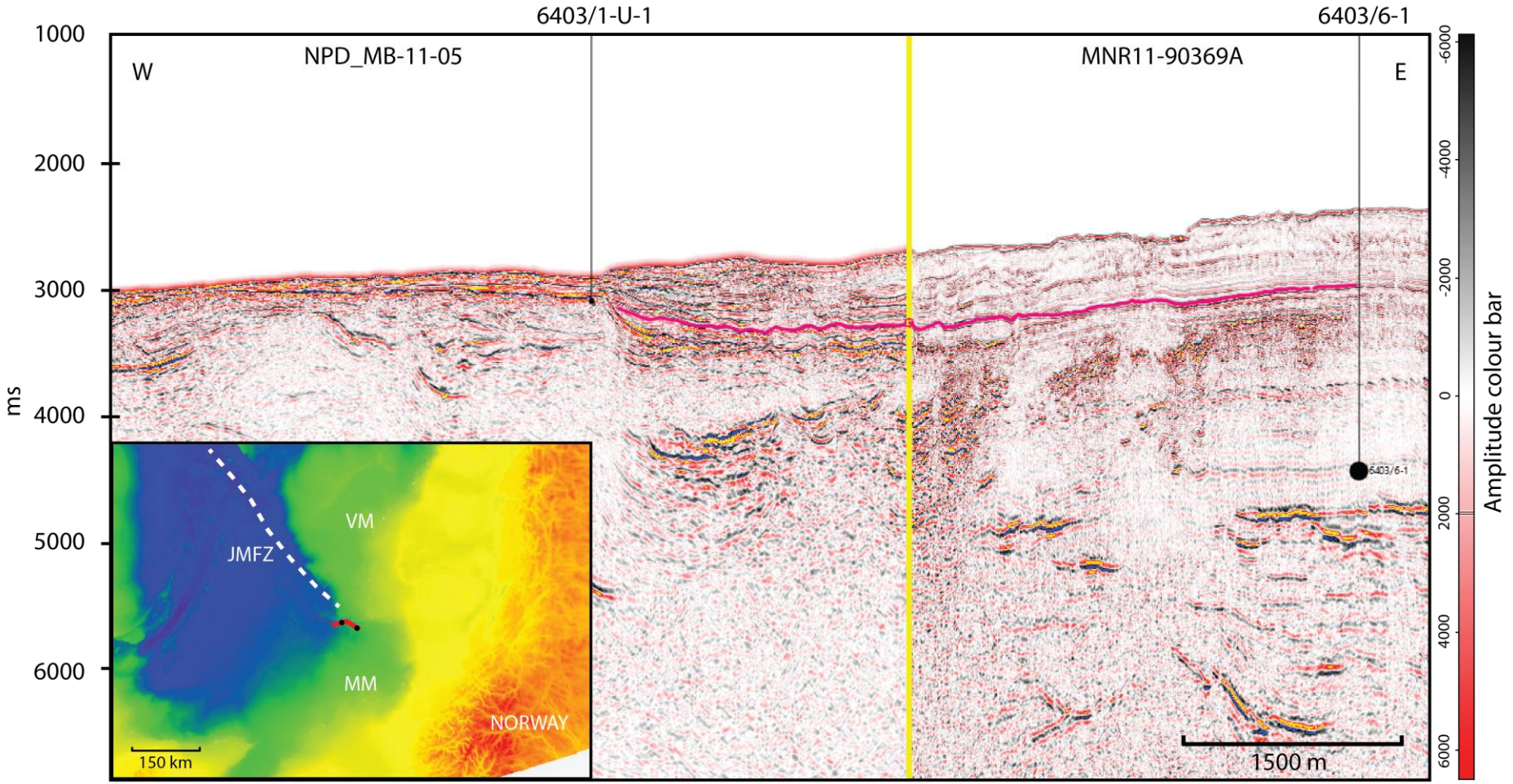

Figure 4.12: The uninterpreted seismic lines NPD_MB-11-05 and MNR11-90369A. The yellow line in the figure represent the intersection point for the respective lines. The location of the profiles is indicated as red lines in the lower left frame of the figure, where NPD_MB-11-05 is found to the west, and MNR11-90369A to the east. The location of the wells on the seismic lines are marked as black circles. MM: Møre Margin; VM: Vøring Margin; JMFZ: Jan Mayen Fracture Zone.

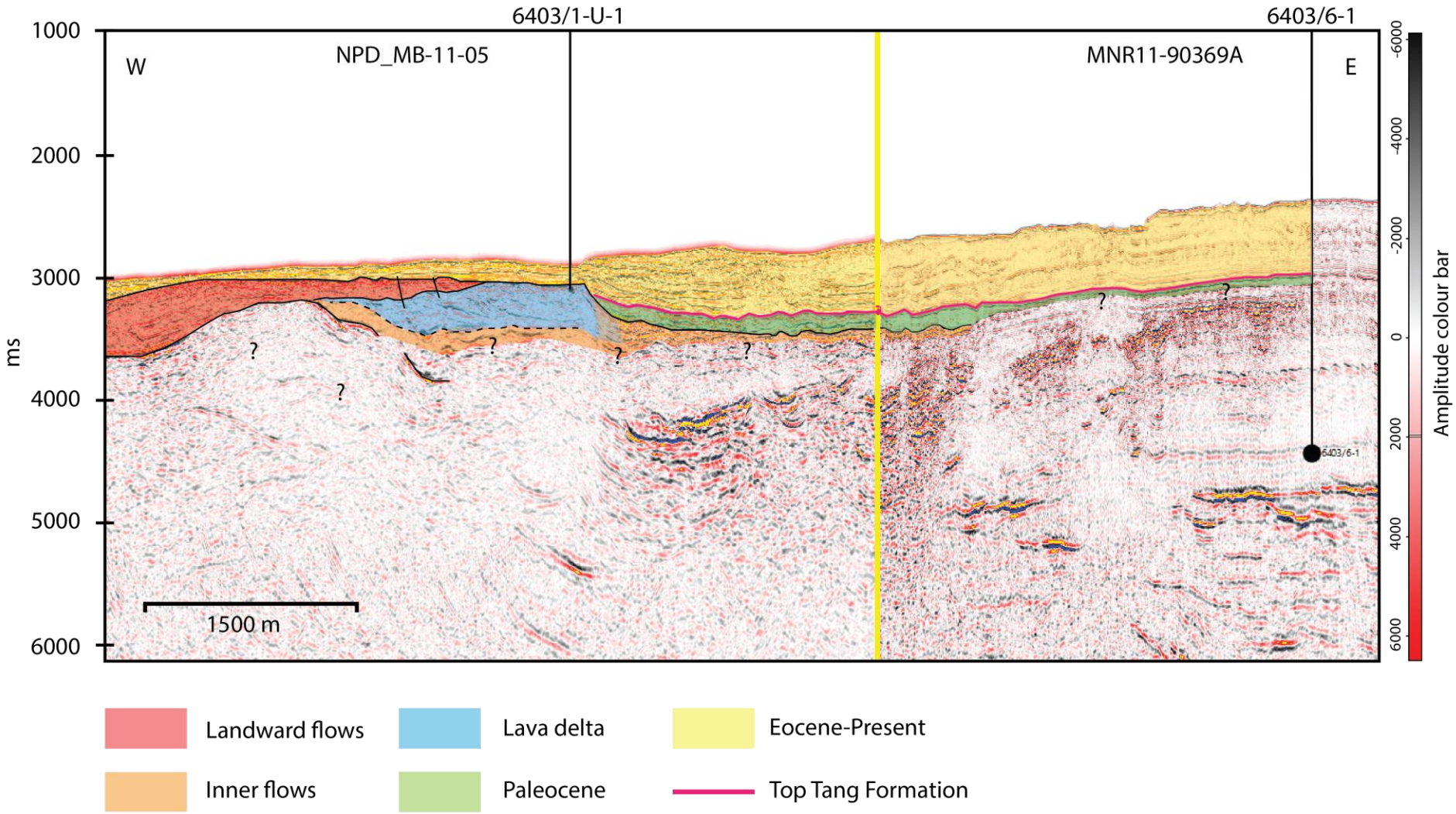

Figure 4.13: Interpretation of the seismic lines NPD_MB-11-05 and MNR11-90369A. Note that the top of the Tang Formation laps onto the lava delta which proves that the volcanic succession must be older than ~56 Ma. The landward flows are lacking ~700 m west of the escarpment, indicating that the volcanic succession must have experienced erosion and possibly uplift some time after emplacement.

As seen in fig. 4.13, the horizon onlaps the delta slope, proving that the volcanic succession of the study area must be older than ~56 Ma. Efforts were made to correlate the top of an older formation as well (i.e. top Springar Formation), which unfortunately turned out to be too difficult during the limited time available for performing the seismic observations, as the inner flows and related intrusions complicated a deeper correlation from the 6403/6-1 well.

It should also be noted that the landward flows, which normally overlie the lava delta, are not present ~700 m west of the escarpment. This observation agrees with the fact that no upper subaerial lava flow layer was identified in the core. The lava delta must therefore have experienced erosion and possibly uplift subsequent to emplacement, and the dated sediments from the core must overlie a hiatus of unknown age.

5 Discussion

The chapter firstly addresses the interpretation of the described lithofacies and the environment in which they are interpreted to have formed. This is followed by an assessment of the reliability of the chemical and isotopic data presented in the study. Thereafter, the role of crustal contribution to the rocks, and a comparison of this study´s rocks with other igneous rocks formed during the opening of the Norwegian-Greenland Sea, are addressed. This is followed by some constraints on the time of emplacement of the succession. Finally, the chapter addresses the proposed eruption history and petrogenesis of the igneous rocks of this study.

5.1 Environment of emplacement

The ~40 m thick volcanic succession in drill hole 6403/1-U-1 confirms that the prograding clinoforms observed in seismic records of the study area, as well as in adjacent areas along the Norwegian Continental Margin (e.g. Planke et al., 2000; Abdelmalak et al., 2016), have a volcanic origin. The volcanic succession consists of brecciated material, comprising hyaloclastite and incorporated microcrystalline basalt clasts, and interlayered coherent lava flows. It is therefore evident, by combining these findings with the observations made during investigations of the seismic lines, that the prograding reflectors observed in the seismic record correspond to brecciated sheets of volcanic material. From this, it is also clear that the subaerial landward flows have been feeding the lava delta unit, by fragmentation upon contact with water at the paleo-shoreline, forming material that have constructed the lava delta. This interpretation supports the previous model presented by Smythe et al. (1983); that the Faeroe-Shetland Escarpment marks the temporary shoreline at the time of emplacement. The cored part of the volcanic succession has been divided into four different lithofacies. The following will address the interpretation of these facies, and the environment in which they are interpreted to have formed.

5.1.1 Interpretation of described lithofacies

Coherent lava flow

The preferred interpretation of this lithofacies is that it represents coherent lava flows. This interpretation is supported by concentration of vesicles in the upper part of some flows, and that the coherent flows seem to “fill in” the contacts to underlying hyaloclastite units. The

presence of reddened flows tops, resulting from subaerial weathering, can indicate that lava flows have been emplaced subaerially (e.g. Viereck et al., 1988). Due to the lack of such tops, along with the fact that the coherent lava flows are closely associated with hyaloclastite deposits, the lava flows are interpreted to have been emplaced subaqueously. Likely, the lava flows originated on land, sustained when flowing into water, thus continued to flow down the subaqueous slope (process 1 in fig. 5.1). Such deposits have previously been observed both *in situ* by active lava-fed deltas on Hawaii (Moore et al., 1973) and in ancient lava delta deposits (e.g. Skilling, 2002). Upon entry to water, the physical parameters of the lava can either promote or inhibit fragmentation (Watton et al., 2013). Coherent lava flows can develop if the volume of a flow is large and prolonged (Moore et al., 1973), or if the extrusion rate is rapid (Skilling, 2002). Other parameters, such as if the lava flow has been protected from the active surf (Moore et al., 1973), can also have impact on fragmentation. However, the possibility that the unit simply represent bigger, massive fragments incorporated in the hyaloclastite cannot be ruled out.

Clast-supported hyaloclastite breccia

The units of this lithofacies is characterised by massive microcrystalline basalt clasts, which are bounded by a matrix of hyaloclastite (<50%). The jigsaw-fit texture observed in the units is typical of *in-situ* fractionation and limited remobilisation of fragments (McPhie et al., 1993). Thus, the breccia is interpreted to have formed as a result of *in-situ* brittle processes operating on cooled and crystallised lava margins, moving down the submarine slope (process 3 in fig. 5.1). The brittle processes can involve fracturing as a result of cooling contraction from chilling of water, and/or by movement of lava beneath a chilled crust (e.g. Skilling, 2002). The interstitial hyaloclastite is interpreted to have primarily formed by mechanically fragmentation, such as spalling of glassy rinds at the margins of lava flows (e.g. McPhie et al., 1993).

Matrix-supported hyaloclastite breccia

Group 1

The angular basalt clasts present in this lithofacies are interpreted to initially been fragmented by brittle processes operating on submarine lava flows, such as the brittle processes described above. It is also possible that some of the fragmentation has occurred prior to water entry (of subaerial lavas). If so, the subaerial fragmentation must have occurred shortly before submarine deposition, as no sign of subaerial weathering is recorded for the clasts. Clasts with

fluidal outlines can also be generated during emplacement of lava delta deposits. According to Skilling (2002), fluidal clasts can be generated by ductile processes, such as gravity-driven elongation and subsequently ductile detachment at the margins of incompletely solidified lava flows (pillow lavas or sheet flows) travelling downslope (process 4 in fig. 5.1). Both clast types have likely experienced further fragmentation and modification resulting from other processes, such as downslope push from either active lavas, or mass flows, further up on the delta slope, or other processes such as wave activity (Skilling, 2002). The hyaloclastite matrix is interpreted to have formed mostly by quench fragmentation, occurring upon initial lava-water contact at the shoreline (process 2 in fig. 5.1). This process is favoured by small-volume lava streams, where the lava immediately will quench and shatter to glassy fragments (Moore et al., 1973).

Destabilisation of hyaloclastite deposits on unstable slopes of submarine volcanic constructions can lead to downslope reworking and formation of a matrix-supported breccia (e.g. Watton et al., 2013). This poorly sorted lithofacies contains two morphologically different types of basaltic clasts, formed by different fragmentation processes. The clasts have been incorporated in the hyaloclastite matrix, suggesting that the unit must have undergone at least some reworking. The lithofacies resemble deposits described in literature (e.g. Bergh and Sigvaldason, 1991; White, 2000; Watton et al., 2013), interpreted to have been emplaced by gravity-driven avalanching of debris (mass flows), along steep delta slopes.

Group 2

This group is interpreted to have formed by much of the same processes as Group 1. However, the presence of only one type of clasts in the group (although different degree of crystallinity) implies that it may have undergone less reworking than Group 1. The morphology of the clasts suggests that they have been formed by fragmenting processes operating on flows of a variable degree of crystallinity.

Fine-grained hyaloclastite ash

The fine-grained and well-sorted lithofacies is interpreted to represent pauses in the supply of hyaloclastite material to the system. The deposits could be the result of fall out from buoyant suspension plumes generated over more coarse-grained lithofacies during remobilisation and transportation of material downslope, or from settling of fine-grained fragments from the water column during pauses in, or ceasing of, the volcanic activity (process 7 in fig. 5.1) (e.g.

Fisher, 1984; Skilling, 2002; Watton et al., 2013). The units of this lithofacies typically transitions into the more coarse-grained, matrix-supported hyaloclastite breccia lithofacies. This association may point to cycles in the supply of material to the system.

5.1.2 Emplacement model

A simple, schematic model of the interpreted environment of emplacement for the cored volcanic succession is presented in fig. 5.1, where the different processes of emplacement is annotated 1–7. The model differentiates between the coherent lava flow facies (1), primary fragmentation processes (2, 3, 4 and 5), gravity-driven processes leading to the incorporation of fragments into the matrix-supported breccia units (6) and the fall-out deposits from the water column (7).

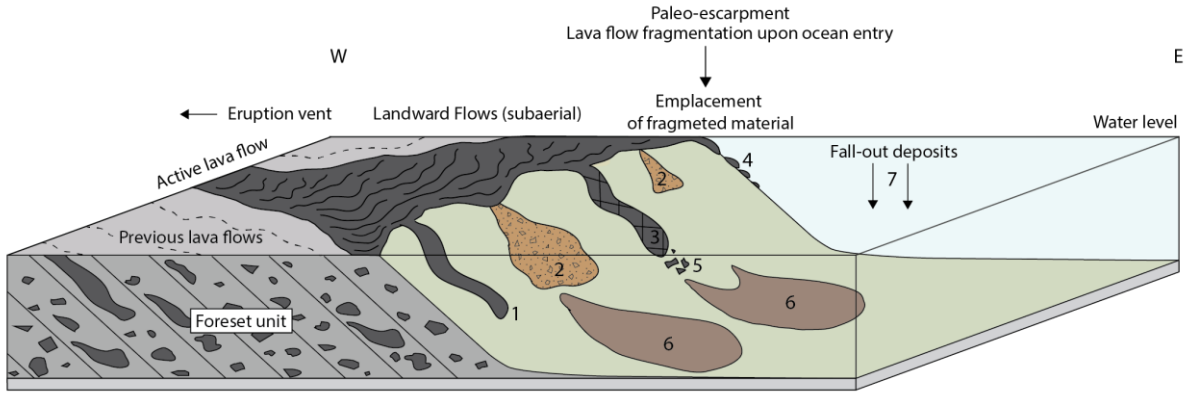

Figure 5.1: Schematic illustration of the interpreted depositional environment for the cored succession. The deposits are interpreted to derive from a lava-fed delta, formed by fragmentation of subaerial lava flows upon contact with water at the paleo-shoreline, which is marked by the present-day Faeroe-Shetland Escarpment in the seismic record. 1: coherent lava flow which have maintained continuity when flowing into water; 2: quench-fragmentation of lava flows upon initial lava-water contact; 3: *in-situ* brittle fragmentation of subaqueous lava flow; 4: ductile elongation and detachment of incompletely solidified lava flow; 5: angular detritus derived from brittle fragmentation processes; 6: gravity-driven remobilisation of fragmented material; 7: fine-grained, fall-out deposits from the water column.

5.2 Alteration effects on the geochemical data

5.2.1 Trace elements

There have been some uncertainties regarding the effect of alteration of the samples presented in this study. Due to the limited amount of sample material, the samples were not ignited, so the loss on ignition (LOI) has not been determined. This fact complicates the quantification of the alteration of the samples, and the "freshness" of samples has solely been based upon visible examination during the sample preparations (handpicking of fresh material) (see

section 3.4 in Methods). During this procedure, three samples were considered as relatively fresh (C.23, C.28 and C.31), and three samples were considered to be somewhat affected by alteration (C.18, C.20 and C.33), in particularly C.33. In addition to this, thin section analysis of sample C.20 confirms that no fresh glass is present.

The sample set, however, consisting of relatively fresh and more altered samples, provides an excellent test of the alteration effects. This is illustrated in fig. 5.2, where the ratio altered sample/fresh sample (where the fresh sample is represented by sample C.23 which has the lowest $^{87}Sr/^{86}Sr$ ratio) has been plotted for the trace elements. As a reference, the ratio C.28/C.23 (fresh/fresh) has also been included in the figure. The alteration process has clearly affected the most mobile elements. Cs is strongly enriched by a factor ranging from ~7.5–12.5. The altered samples are further enriched in Rb and Th by a factor between ~2–3.5, and highly depleted in Ba (by a factor ranging from 7-35). They also show a slight relative increase in the High Field Strength Elements (HFSE), Hf and Zr, and Ti (up to a factor of ~2). Despite the small increase in U for C.33, it is somewhat surprising that U and Pb, which are elements highly mobile during alteration, are relatively unaffected. It is therefore likely that that the peak observed for all samples for Pb (fig. 4.10) represent a crustal contribution to the magma, thus supporting the suggestion that the magma have suffered contamination from the crust. However, Pb is an element, which is susceptible for contamination during sample preparations. Thus, conclusions based solely on Pb should always be treated with care.

The REEs seem to be largely unaffected by alteration. The exception is sample C.33, which show an increase in many of the REE, and especially the most mobile LREE, La and Ce. Thus, the REE abundances of all samples, except C.33, are considered to be reliable. Note that the REEs, Gd and Tb, are not included in the figure. They are expected to behave in the same manner as other middle REE, such as Eu.

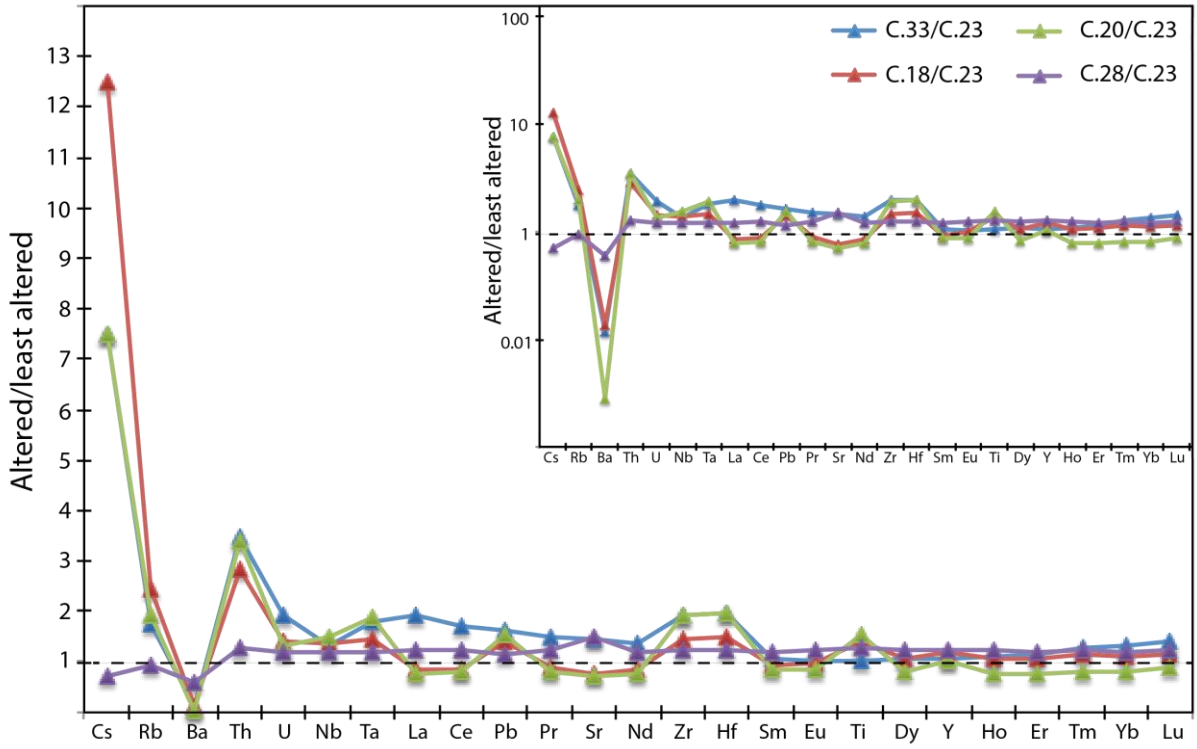

Figure 5.2: Diagram demonstrating the effect of alteration for trace element abundances of the samples presented in this study (in ordinary and logarithmic scale).

5.2.2 Isotopes

Due to the sparse amount of fresh sample material present, the samples were not subjected to acid leaching, to avoid loss of sample material. Seawater alteration effects on Sr and Pb isotope systematics have long been recognized (e.g. Verma, 1992; Krolikowska - Ciaglo et al., 2005), and acid leaching prior to dissolution of rock fragments is considered to be important to achieve accurate Sr and Pb isotopic analyses (Nobre Silva et al., 2010). It has been established that the Sr isotopes presented in this study are strongly affected by seawater alteration, as all samples plot in a straight line towards the $^{87}Sr/^{86}Sr$ ratio of seawater (~0.709) (fig. 4.11), and as the visible most altered samples plot closest to this ratio.

As addressed before, there seems to be no distinct, systematic increase in the Pb isotopic ratios of the more altered samples, compared to the fresher samples. However, all samples presented in this study have systematically higher $^{208}Pb/^{204}Pb$ and $^{207}Pb/^{204}Pb$ ratios for a given $^{206}Pb/^{204}Pb$ ratio compared to the MORB from the Northeast Atlantic (fig. 4.11). This increase in radiogenic isotopes can be related to magma contamination by a source containing

more radiogenic Pb, such as the continental crust. However, it has been reported that seawater alteration also can increase the amount of radiogenic Pb isotopes in basalt glass (e.g. Verma, 1992). Additionally, the Pb isotopic ratios for the samples varies considerably more than both the Nd and Hf isotopic ratios, which are considered to be relatively immobile during alteration (see below). Therefore, there is an uncertainty whether the measured Pb isotopic ratios represent primary compositions or not, thus the data should be treated with care.

On the other hand, the isotopic composition of relatively immobile elements, such as Nd (REE) and Hf (HFSE), are considered to be relatively resistant to alteration (e.g. Verma, 1992; Krolikowska - Ciaglo et al., 2005; Nobre Silva et al., 2010). In addition, unlike Sr, the concentration of Nd and Hf in seawater is extremely low (Faure and Mensing, 2005), thus modifications of these elements by seawater require very high seawater/rock ratios. Despite the large difference in the degree of alteration of the samples, all samples have very similar Nd and Hf isotopic ratios. This indicates that seawater alteration has had a negligible effect on these isotopic ratios. Thus, the data for all samples are regarded as reliable.

5.3 Crustal contamination

Based on major and rare earth element data, it has been established that the samples presented in this study have a tholeiitic, N-MORB composition. However, it is contradicting that the samples show a higher enrichment in other incompatible elements (e.g. Pb), along with more enriched Hf and Nd isotopic ratios, than what would be expected if the samples were derived from a depleted N-MORB source. This fact provides evidence that the samples have experienced contamination from the continental crust.

To evaluate the effect and amount of crustal contribution to the original melt, simple mass balance calculations for mixing of two different components (binary mixing) have been conducted for the REEs (fig. 5.3). To obtain the measured, present-day REE pattern of the samples of this study, a more depleted “primary” (or uncontaminated) melt is needed. Thus, a sample from the highly depleted tholeiitic MORBs acquired along the Jan Mayen Ridge (JMR) (Haaga, 2014) represents an appropriate candidate. As no data of the crustal basement beneath the Møre nor the Vøring marginal highs is available, the assimilant is represented by the total composition of the continental crust, estimated by Rudnick and Gao (2014). By

mixing the JMR magmas with the total composition of the continental crust, it is possible to generate the distinct pattern for the LREEs of the samples (fig. 5.3).

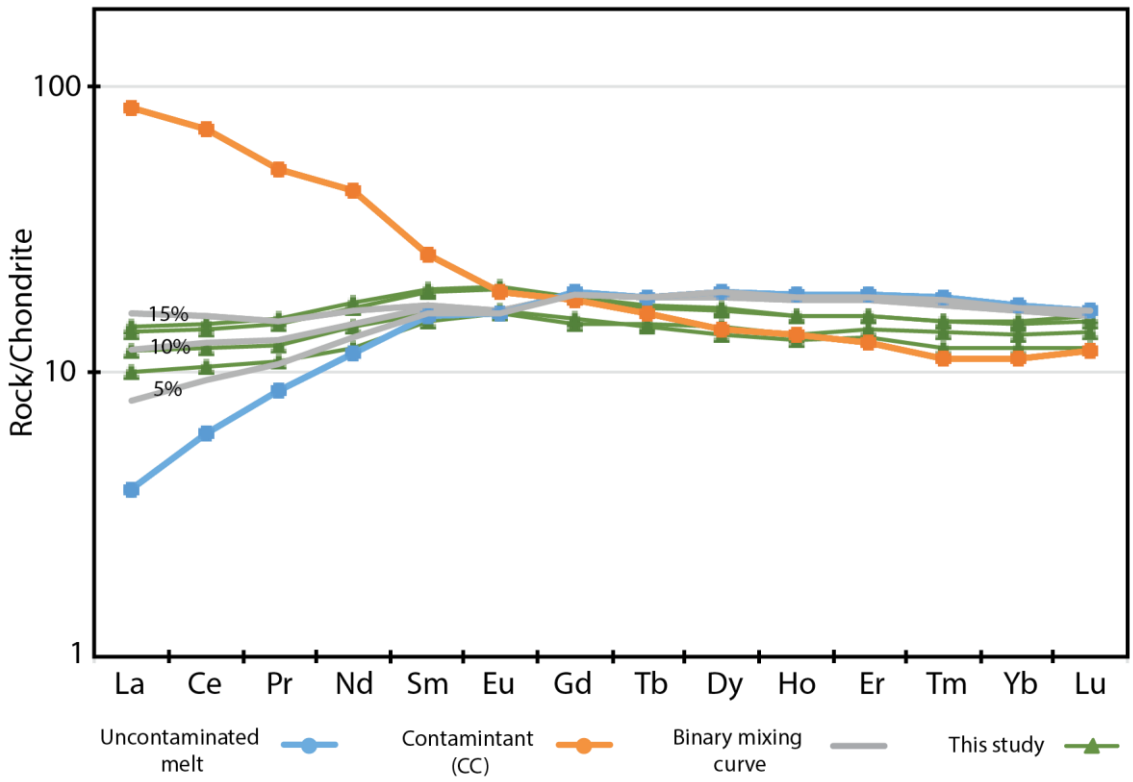

Figure 5.3: Binary mixing modelling between highly depleted MORB from the Jan Mayen Ridge (Haaga, 2014) and the continental crust (estimate from Rudnick and Gao (2014)). The best fit is achieved by adding ~10% of crustal material to the melt, resulting in the distinct bend at Pr, and the flat to slightly declining pattern for the most incompatible LREEs (Pr–La), which is characterising the samples of this study. The chondrite-normalising values are from Sun and McDonough (1989).

As seen in the figure, it is mainly the most incompatible elements (LREEs) that are affected during the process of mixing at low percentages of assimilation. The best fit is achieved by adding ~10% assimilation from the continental crust, as the samples plot on, or parallel to, this trend for the LREEs. This demonstrates that the present-day LREE patterns of the samples can be generated through crustal contamination of melts derived from a mantle source more depleted than a typical N-MORB source, like the JMR sample.

Binary mixing modelling has also been conducted for Hf and Nd isotopes (fig. 5.4), as they are regarded as the most reliable isotopic compositions presented in this study. The uncontaminated primary melt is represented by values from average depleted MORB (D-MORB) from Salters and Stracke (2004) and average N-MORB from Sun and McDonough

(1989). The contaminant is represented by the estimates of the upper continental crust by Chauvel et al. (2014) and Rudnick and Gao (2014). The samples plot perfectly on the mixing curve between these end-members (at c. 10%), providing further evidence of assimilation of crustal material to the parental melt.

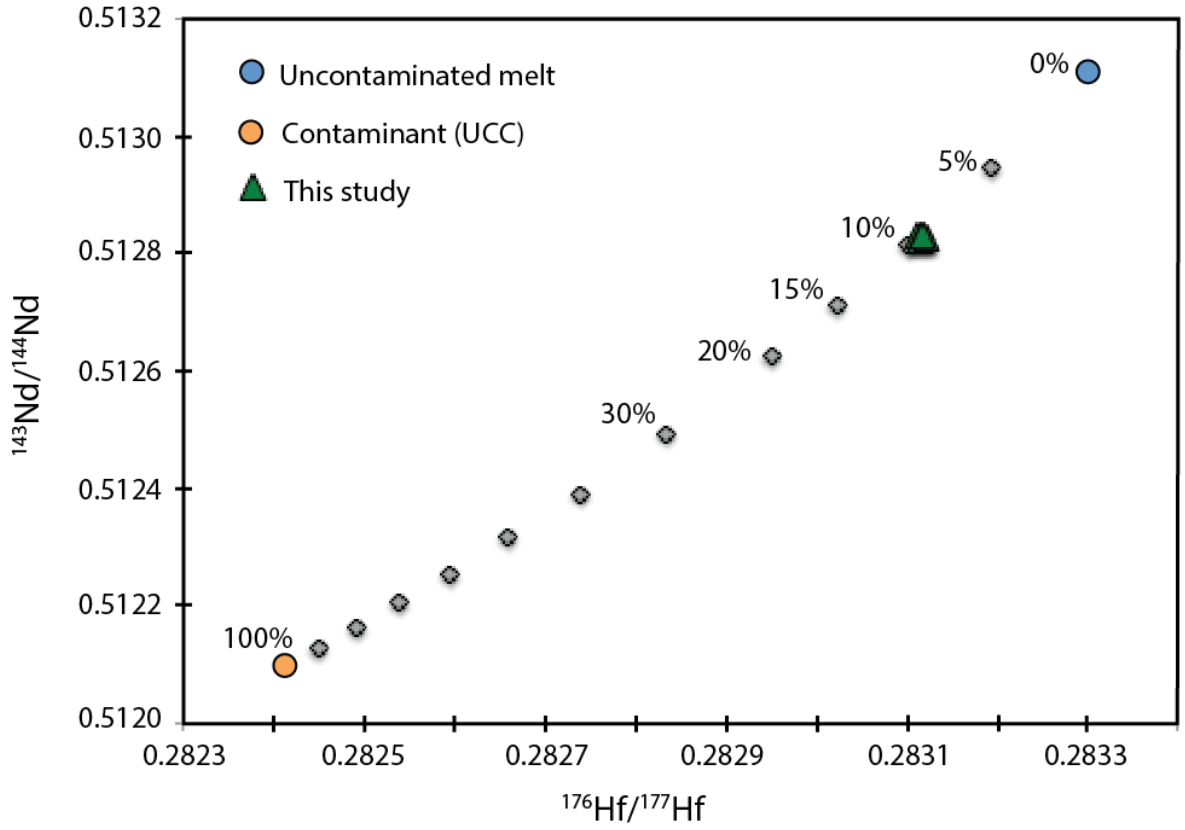

Figure 5.4: Simple binary mixing modelling based on Hf and Nd isotopes. The grey points represent the mixing product at different fractions of assimilation. The different end-members are represented by average depleted MORB from Salters and Stracke (2004) and average N-MORB from Sun and McDonough (1989) (blue circle), and the estimated composition of the upper continental crust from Chauvel et al. (2014) and Rudnick and Gao (2014) (orange circle).

5.4 Comparison to other igneous rift-to-drift related rocks

This subchapter will address the relationship between the samples of this study with other igneous rocks reported from the NAIP. More specifically, the samples are compared to the assemblage of magmatic rocks on the Vøring Margin, SE Greenland Margin and at the JMR, which previously have been described in the Regional geology and previous studies chapter.

5.4.1 Trace elements

The samples from the DSPS leg 38 sites 338, 342 and 343 on the Vøring Marginal High have been described as alkaline to sub-alkaline, and low-alkaline tholeiites, respectively (Kharin, 1976). The site 338 tholeiites have very flat REE patterns that are unfractionated relative to chondrite, whereas the sites 342 and 343 tholeiites, which are chemically indistinguishable, have LREE-enriched patterns, and are interpreted to have derived from a mantle plume source (Schilling, 1976). The samples of this study are largely comparable to the site 338 basalts, indicating that they possibly are somewhat genetically related (fig. 5.5C).

The igneous rocks drilled on the Vøring Marginal High during leg 104 at site 642 are presented in fig. 5.5B. As seen in the figure, the drilled succession is separated into two different units. The upper series tholeiites, which correspond to the SDRs, are interpreted to be mostly uncontaminated (Viereck et al., 1988; Viereck et al., 1989; Meyer et al., 2009). Their chondrite-normalised REE pattern is more enriched than typical N-MORB patterns, suggesting that they are derived from a mantle source more enriched than typical depleted N-MORB mantle (Meyer et al., 2009). On the other hand, the lower series is interpreted to have been derived from large proportions of upper crustal melts (Meyer et al., 2009). This is clearly seen by the higher amounts of LREEs and the negative Eu-anomaly in fig. 5.5B. The samples of this study are comparable to the least enriched samples of the Vøring upper series. However, as the samples of this study are interpreted to have undergone contamination of crustal material, they must essentially have been derived from a mantle source more depleted than the Vøring upper series to generate the present-day REE pattern. Hence, the rocks have likely not been derived from the same mantle source.

It rather seems that the samples of this study have been derived from a source similar to that of the Vøring lower series dikes, and the tholeiites from the Jan Mayen Ridge, both of which are interpreted to have been derived from a mantle source much more depleted than the Vøring upper series (Meyer et al., 2009; Haaga, 2014). As no sign of continental influence

has been reported from the tholeiites from the Jan Mayen Ridge (Haaga, 2014), these samples may very well be comparable to the uncontaminated parental magmas of both the samples presented in this study (as demonstrated by binary mixing in previous section), and the Vøring lower series dikes. Compared to the samples of this study, the Vøring lower series dikes are generally more enriched in the most incompatible LREEs, indicating that they have suffered a higher degree of crustal contamination than the samples of this study. The dikes are also enriched in the HREEs compared to the rocks from the Jan Mayen Ridge and this study, indicating that they are derived by smaller degrees of mantle melting (Meyer et al., 2009).

In terms of REE geochemistry, the doleritic Utgård sills show a higher REE abundance than the samples of this study. They largely fall within the range of the Vøring upper series. Their somewhat higher LREE abundances have been explained by larger amounts of the melt derived from deeper melting in the garnet stability field than the Vøring upper series (Neumann et al., 2013).

The samples of this study fall within the range of the SE Greenland upper series lavas collected during ODP leg 152. As seen in fig. 5.5A, the series ranges from depleted to strongly depleted in the most incompatible REE, and is therefore interpreted to originate from a depleted MORB mantle source (e.g. Fitton et al., 1998b; Fitton et al., 2000). Most of the lavas are uncontaminated, with the exception of some samples from the upper part of the series (i.e. most LREE enriched sample in fig. 5.5A) (Fitton et al., 2000). The samples of this study resemble this enriched sample, and differ from the rest of the samples by the relatively flat pattern for the LREE. This probably reflects the crustal contribution to these lavas. The SE Greenland middle and lower series on the other hand, have extremely enriched LREE patterns. As the Vøring lower series, they also record pre-breakup magmatism and have undergone extensive contamination from the continental crust (Fitton et al., 2000).

The tholeiitic microgabbros collected at the Gjallar Ridge on the western Vøring Margin are interpreted to be comparable to the Vøring upper series (Styve, 2015). The similarity between these rocks and the samples of this study is striking, as their REE fingerprints are more or less identical (fig. 5.5F). This strongly implies that the rocks are genetically related, and that they share a common genesis. Thus, I suggest that these rocks also have been derived from a highly depleted mantle source, followed by crustal contamination, providing the present-day REE pattern.

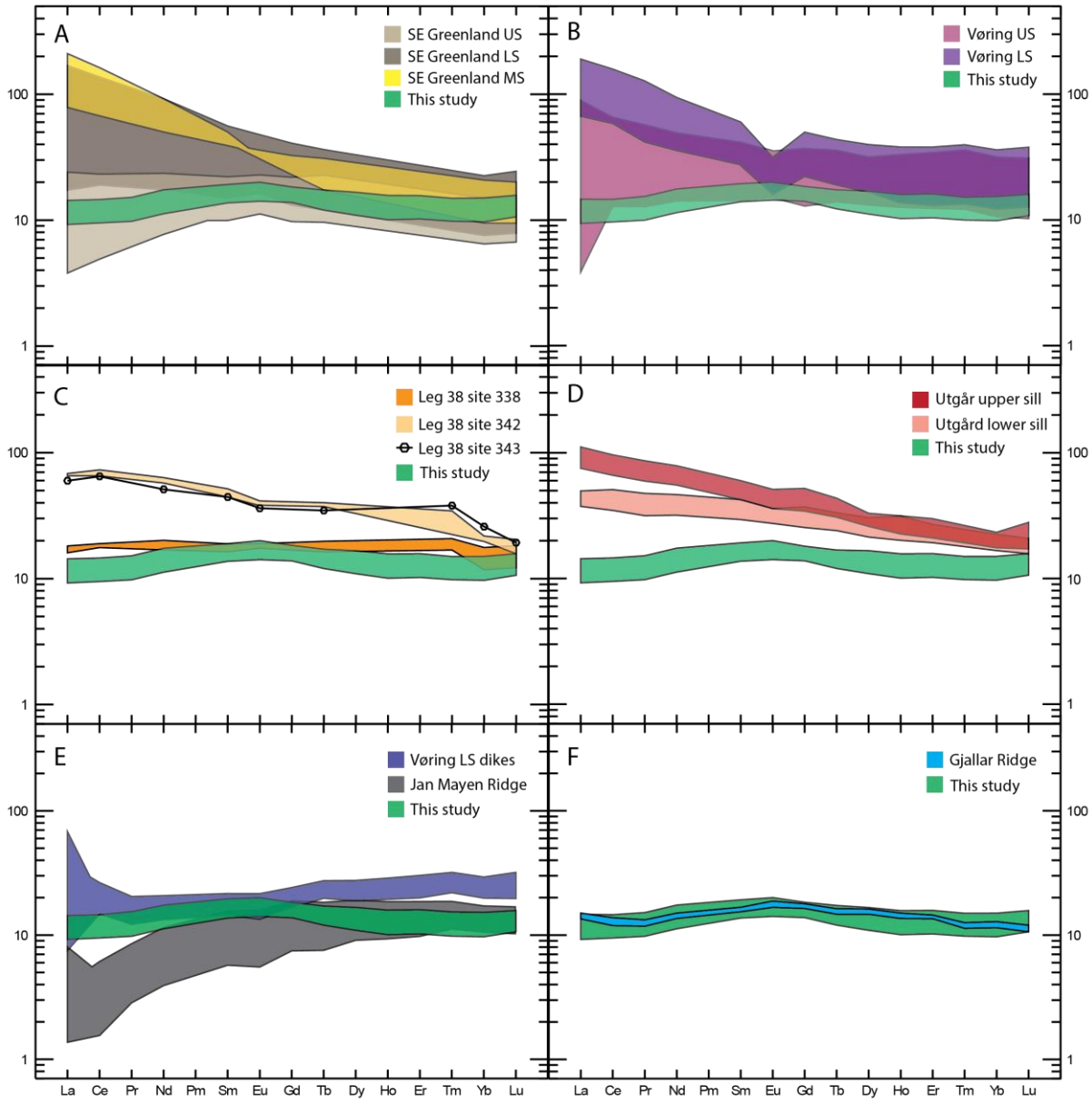

Figure 5.5: REE patterns for various rocks related to the NAIP and the opening of the Norwegian-Greenland Sea. Note the almost identical REE patterns for the samples of this study and the samples from the Gjallar Ridge. Data from: Schilling (1976); Fitton et al. (1998b); Meyer et al. (2009); Neumann et al. (2013); Haaga (2014); Styve (2015). Chondrite-normalising values are from Sun and McDonough (1989). US: upper series; MS: middle series; LS: lower series.

The variation and relationship of the opening-related rocks on the Norwegian and Greenland margins can be demonstrated in the Hf-Th-Ta discrimination diagram (fig. 5.6) by Wood (1980). The Hf-Th-Ta ratios are extremely sensitive to crustal assimilation, and melts, which have experienced contamination, typically shift toward the Th corner of the diagram. The

samples of this study, the Vøring lower series and lower series dikes, and the SE Greenland middle series, all fall on a "mixing line" between the strongly depleted tholeiites from the JMR and the upper continental crust. This indicates that the samples have experienced contamination by rocks of upper crustal composition. This is also the case for some of the rocks from the SE Greenland upper series, inferring that also parts of this unit have undergone assimilation. The SE Greenland lower series, on the other hand, plots towards the composition of the lower continental crust, indicating that the lower crust has been the main contaminant for the unit. As the diagram displays, the Vøring upper series seems to be largely uncontaminated and plots between typical N-MORB and E-MORB compositions. The two groupings displayed by the samples of this study in the diagram are most likely the result of the enrichement of Th during seawater alteration, which has affected the most altered samples.

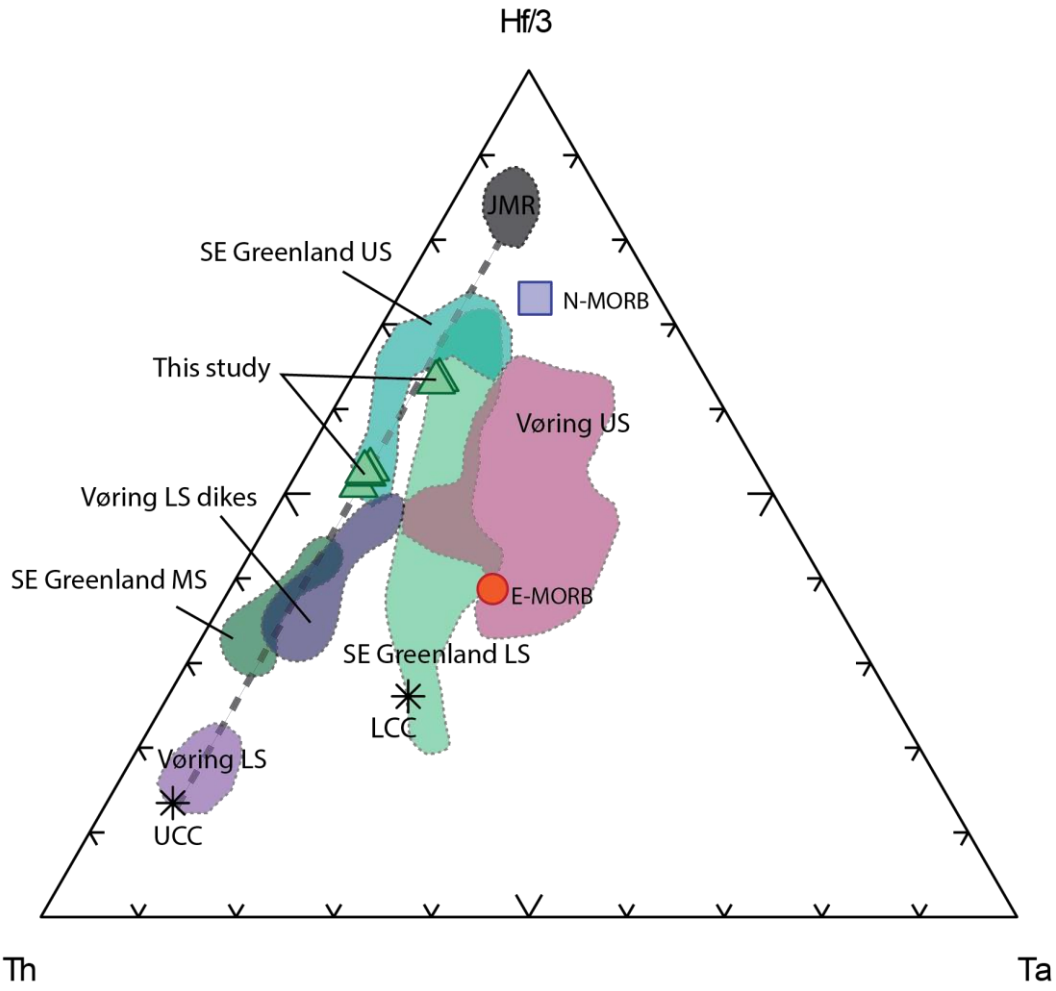

Figure 5.6: Hf-Th-Ta diagram for igneous rocks related to the NAIP. The compositions for the upper (UCC) and lower continental crust (LCC) are from Rudnick and Gao (2014), and average N-MORB and E-MORB compositions are from Sun and McDonough (1989). The data sources for the NAIP rocks are the same as in fig. 5.5. US: upper series; MS: middle series; LS: lower series

5.4.2 Isotopes

Unfortunately, no Hf isotopic data has been reported for the NAIP rifted margin rocks. The comparison is therefore based on plots containing Nd, and the less reliable Sr and Pb isotopic data from this study. Fig. 5.7 is demonstrating the wide variation in Sr and Nd isotopes of samples from the Norwegian and the conjugate Greenland margin, belonging to the NAIP. The variation mainly reflects the effect of crustal contamination (Saunders et al., 1997). As displayed in the figure, the Vøring and SE Greenland lower series are fundamentally different in terms of Sr and Nd isotopic ratios. The SE Greenland lower series is characterised by both low $^{143}Nd/^{144}Nd$ and $^{87}Sr/^{86}Sr$ isotopic ratios, whereas the Vøring lower series is characterised by low $^{143}Nd/^{144}Nd$ and high $^{87}Sr/^{86}Sr$ isotopic ratios. The different trends are believed to result from contamination of different parts of the continental crust, as the trends correlate to the lower and upper crust, respectively (Saunders et al., 1997; Meyer et al., 2009).

The Vøring lower series dikes plot intermediate between the Vøring upper and lower series (figs. 5.7 and 5.8). The differences in the isotopic ratios can either be the result of a long-term difference in the mantle source, or by contamination from the continental crust (Meyer et al., 2009). As previously addressed, the dikes show enrichment in the most incompatible REEs, La and Ce, which favour the latter explanation. As seen in figs. 5.7 and 5.8, the samples of this study also fall on this “mixing line”, intermediate between the Vøring upper series and lower series dikes. This is also the case for the rocks from the Gjallar Ridge (fig. 5.7), which is in agreement with the proposed linked genesis of these rocks with the samples of this study. This systematics make it likely that the samples of this study and the rocks from the Gjallar Ridge also have experienced assimilation by melts formed by upper crustal rocks, rather than lower crustal rocks, which mainly is the case for the SE Greenland lower series (fig. 5.7) (Fitton et al., 2000).

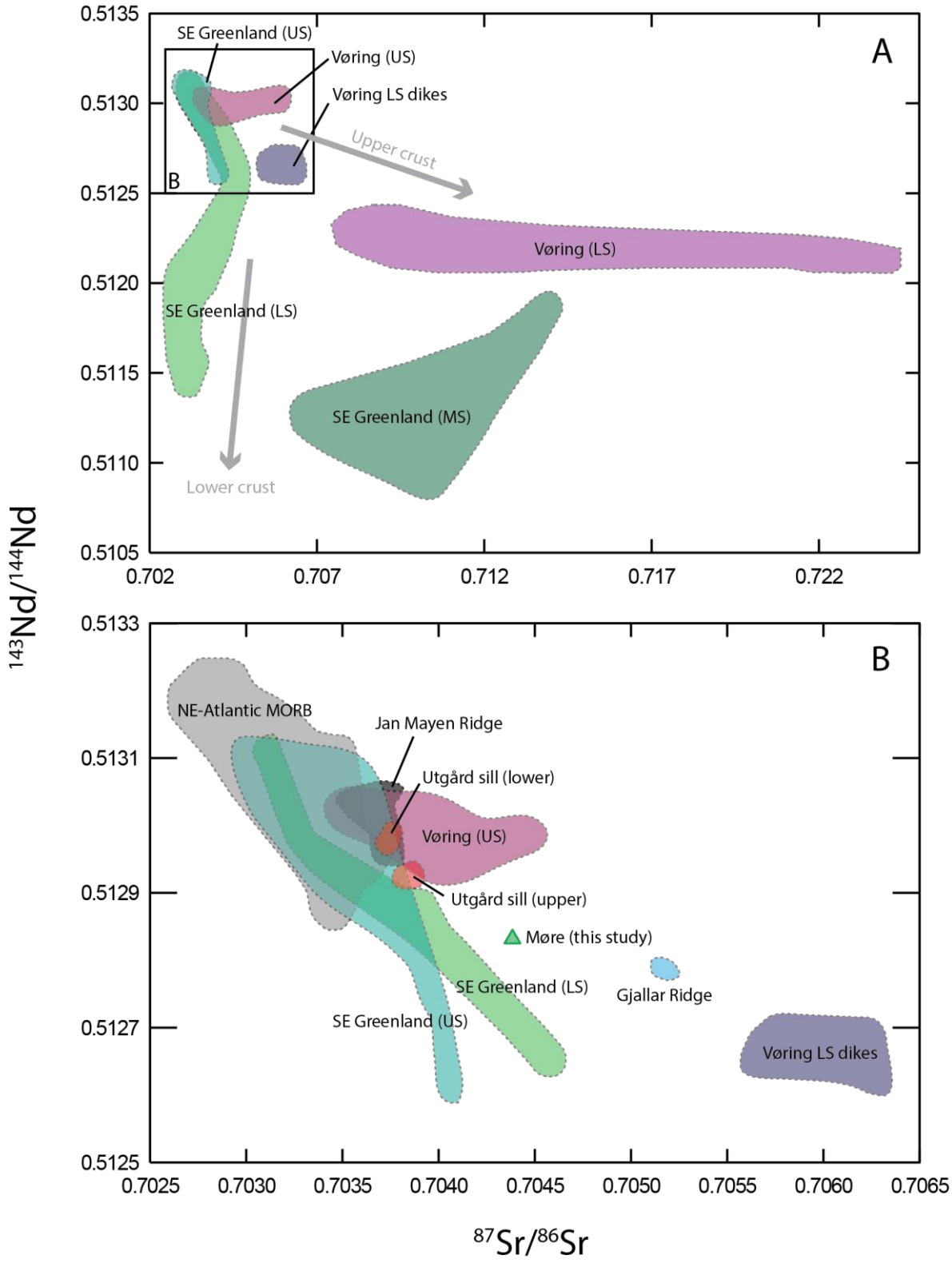

Figure 5.7: $^{143}Nd/^{144}Nd$ versus $^{87}Sr/^{86}Sr$ plot of various rocks belonging to the NAIP rifted margins. The samples of this study are represented by sample C.23, which is the least altered sample in terms of $^{87}Sr/^{86}Sr$ ratios. Data from: Fitton et al. (1998a); Meyer et al. (2009); Neumann et al. (2013); Haaga (2014); Styve (2015). The Northeast Atlantic MORB data are retrieved from the PetDB petrological database. US: Upper series; MS: Middle series; LS: Lower series.

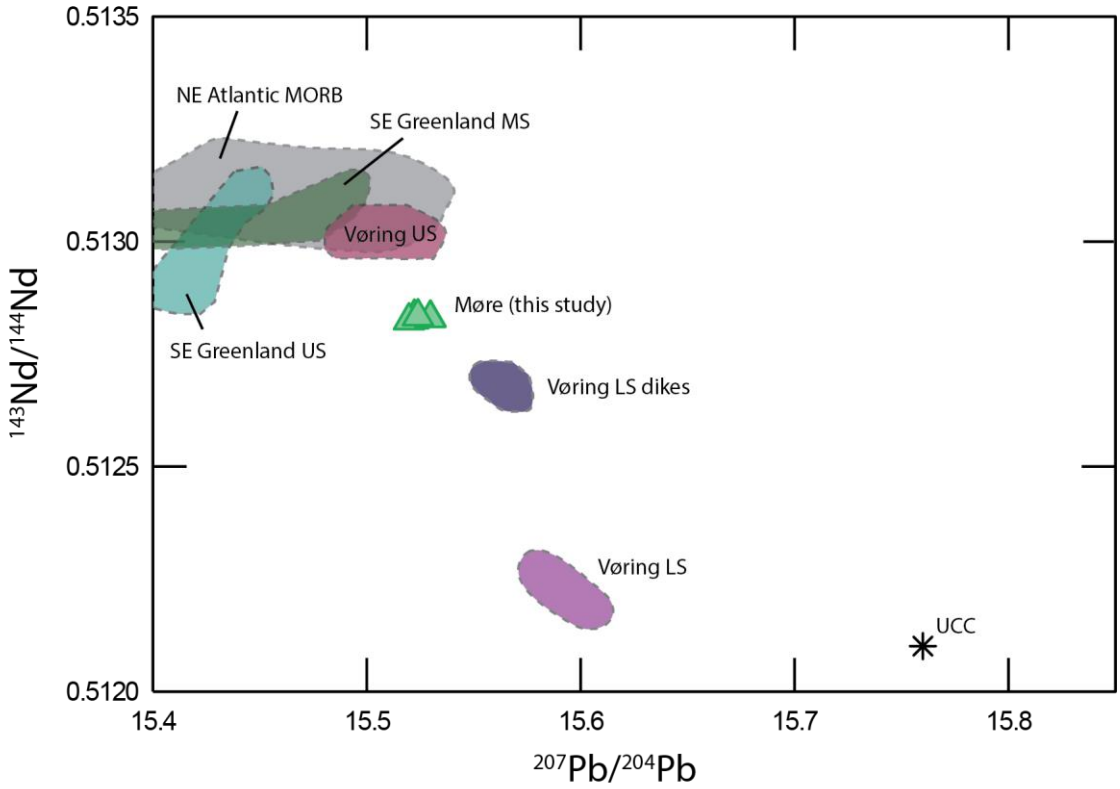

Figure 5.8: $^{143}Nd/^{144}Nd$ versus $^{207}Pb/^{204}Pb$ plot of various rocks belonging to the NAIP rifted margins. Data sources are the same as in fig. 5.7, except the Vøring LS data which are from Taylor and Morton (1989). The $^{143}Nd/^{144}Nd$ and $^{207}Pb/^{204}Pb$ isotopic ratios for the upper continental crust is from Chauvel et al. (2014) and Asmerom and Jacobsen (1993) respectively. US: upper series; MS: middle series; LS: lower series.

5.5 Time of emplacement

Based on the observations made during the study of two seismic lines located over the study area, it is evident that the volcanic succession must be older than the top of the Tang Formation (~56 Ma) (NPD, 2014) which onlaps the lava delta. Another important observation is that the subaerial landwards flows are lacking ~700 m west of the Faeroe-Shetland Escarpment, which also agrees with the core description. As mentioned, this implies that the area must have experienced erosion sometime after emplacement, and that the dated sediments (age: 55 Ma) overlying the volcanic succession likely lie on a hiatus of unknown age.

In the Norwegian Sea, the Tare Formation overlies the Tang Formation. The Tare Formation corresponds to the Paleocene–Eocene transition (56 Ma) (NPD, 2014) and correlates to the regional tuff marker, the Balder Formation, in the North Sea (Dalland et al., 1988). This tuff

marker has been related to the seaward-dipping reflectors, i.e. the Vøring upper series, and the inner flows on the Vøring Marginal High (Skogseid and Eldholm, 1989). This relationship is generally believed to also be the case for the Møre Marginal High (e.g. Blystad et al., 1995). However, as the top of the Tang Formation is not continuous with the lava delta and the inner flows at the part of the Møre Marginal High studied here, but instead onlaps the lava delta, the succession seems to be somewhat older than what generally is the consensus for the extrusive complexes on the Vøring and Møre marginal highs. Similar observations have been made from the southwestern Vøring Margin, suggesting earlier lava effusion also here (Skogseid and Eldholm, 1989; Hjelstuen et al., 1999). This study note that both areas are located close to the Jan Mayen Fracture Zone, and although highly speculative, this might suggest that the weakness zone has acted as a conduit for earlier lava flows.

It is known that the area experienced uplift in the Paleocene, presumably as the result of thermal uplift induced by the Icelandic mantle plume (Saunders et al., 1997). Based on stratigraphic data from wells located on the Møre and Vøring margins, Harald Brekke (personal communication, 2017) concluded that the uplift and erosion in the area most probably occurred in the latest Danian to earliest Selandian (~61.6 Ma). It is tempting to suggest that the hiatus between the dated sediments and the volcanic sequence is related to this phase. If so, the volcanic succession can have formed prior to ~61.6 Ma, making them considerably older than other opening-related volcanics on the Norwegian Margin (c. 55 Ma) (e.g. Eldholm et al., 1989a), in fact, one of the oldest rocks recorded within the NAIP. Following this reasoning, the volcanic succession on the Møre Marginal High studied here is likely to have been emplaced during the first major phase of igneous activity within the NAIP, beginning at about 62 Ma (Saunders et al., 1997). This contradicts the previous understanding of the magmatic development of the area, where the volcanic deposits on the marginal highs are interpreted to have formed during the second main phase of the NAIP igneous activity (peaking at about 56 Ma) (Saunders et al., 1997).

However, hiatuses occurring in lava delta systems can also be related to waning of volcanic activity, subsequent sea erosion of the shoreline and collapse of parts of the delta front, or by lobe switching with consequently removal of deposits to another location (Wright et al., 2012). In addition to this, the rocks of this study correlate to other igneous rocks from the Vøring and SE Greenland margin, which are interpreted to have formed during the second

main phase of the NAIP igneous activity. Thus, it is more likely that the lava delta unit also have formed during this phase.

The samples of this study fall within the range of the SE Greenland upper series in terms of REE patterns. The SE Greenland upper series has not been successfully dated, but are interpreted to have formed during breakup and earliest seafloor spreading stage at ~55 Ma (Fitton et al., 2000). The samples of this study have a closer affinity to the Vøring lower series dikes than the Vøring upper series, which might suggest that the deposits are coeval. Both the samples of this study and the Vøring lower series dikes are interpreted to initially derive from a mantle source more depleted than typical N-MORB sources, with later modifications due to crustal assimilation processes. The Vøring lower series, in which the dikes intrude, yield a Rb-Sr age of 57.8±1.0 Ma (LeHuray and Johnson, 1989) and a biostratigraphic age (from sediments) ranging from 57.5–59.0 Ma (Boulter and Manum, 1989), and is thus interpreted to record pre-breakup magmatism. The dikes are chemically distinct from the Vøring upper series, which have led to the conclusion that they are not the feeder dikes of the upper series lavas (Meyer et al., 2009). Apparently, the dikes post-date the Vøring lower series but must have intruded prior to the main feeder dikes of the upper series (Eldholm et al., 1989a). Unlike the SDRs on the Vøring and SE Greenland margins, both the Vøring lower series dikes and the samples of this study display evidence of crustal contamination, resulting from storage in crustal reservoirs for some time prior to eruption. Thus, it is likely that the lava delta on the Møre Marginal High also have been emplaced during the time span between the Vøring lower and upper series, at a time of progressively increasing magmatism, as asthenospheric material progressively rises to the surface. The phase culminates with the volcanic surge of crustally uncontaminated MORB-like SDRs during the continental breakup and earliest seafloor speeding at ~55 Ma.

5.6 Eruption history and petrogenesis of the igneous rocks of this study

Based on the petrological, geochemical and isotopic data, supplemented by information from the core description and the observations made during the study of seismic lines, I propose the following evolutionary history for the volcanic succession on the Møre Marginal High.

After several rift phases from the end of the Caledonian Orogeny, final breakup between Greenland and Eurasia occurred at the Paleocene–Eocene transition. Due to the heavily thinned and stretched lithosphere, the asthenosphere starts to rise into the lithosphere. Under lithospheric pressure conditions, the hot asthenosphere starts to melt by decompression, and will further intrude the crystalline crust. These crustal melts furthered weaken the lithosphere, leading to the final breakup between the continents. The rift-to-drift stage is associated with eruption of huge amounts of MORB-like melts, indicating the point where the asthenosphere reaches the surface. The volcanic succession on the Møre Marginal High has likely been emplaced just prior to the rift-to-drift stage in the Late Paleocene, as they are representative of such tholeiitic MORBs. The succession contains evidence of assimilation of crustal material, indicating that continental rupture was not complete at the time of emplacement.

The primary mineralogy of the massive microcrystalline basalt clasts and the hyaloclastite breccia from different parts of the core is very similar, indicating that they have crystallised from the same magma, and possibly during the same eruption. This is being supported by similar trace element characteristics, and close to identical Nd and Hf isotopic ratios. The first generation of phenocrystals, represented by olivines with chrome spinel inclusions, is considerably larger than the second generation of phenocrystals. Thus, they must have formed by slower cooling of the magma at greater depths, compared to the second generation of phenocrystals. Their forsterite content is also slightly higher than the second generation of olivines, indicating that they have crystallised from a less evolved magma. At this stage, magma also appears to have assimilated crustal material, which have modified its chemistry and isotopic signature. Based on geochemical modelling, the upper crust appears to be the main contaminant. This indicates that the crustal basement below the Møre Marginal High is of an upper crustal composition, consistent with what previously has been inferred from the Vøring Marginal High (e.g. Viereck et al., 1988; Meyer et al., 2009).

During the eruption, the melt travelled eastward from the volcanic vent located at the break-up axis. The lava flows were sustained until reaching the paleo-shoreline, which today is marked with the Faeroe-Shetland Escarpment. The second generation of phenocrystals, plagioclase and olivine, probably formed at this phase, i.e. during the transportation from the volcanic vent to the paleo-shoreline. Several evidences, i.e. the formation of sideromelane glass and variolitic zones, imply that both the hyaloclasite, and most of the massive basalt clasts, underwent rapid cooling in the presence of water. The quenching of the lava led to the formation of large amounts of brecciated material at the water-sea contact. Such deposits are highly unstable, and gravity-driven processes further modified most of the deposits while constructing the lava delta. The lack of the subaerial top layer of the lava delta is probably the result of waning in volcanic activity at the site of emplacement, which made room for sea erosion of the shoreline and the volcanic construction. Subsequently to emplacement, the succession experienced modifications by low-temperature, seawater alteration.

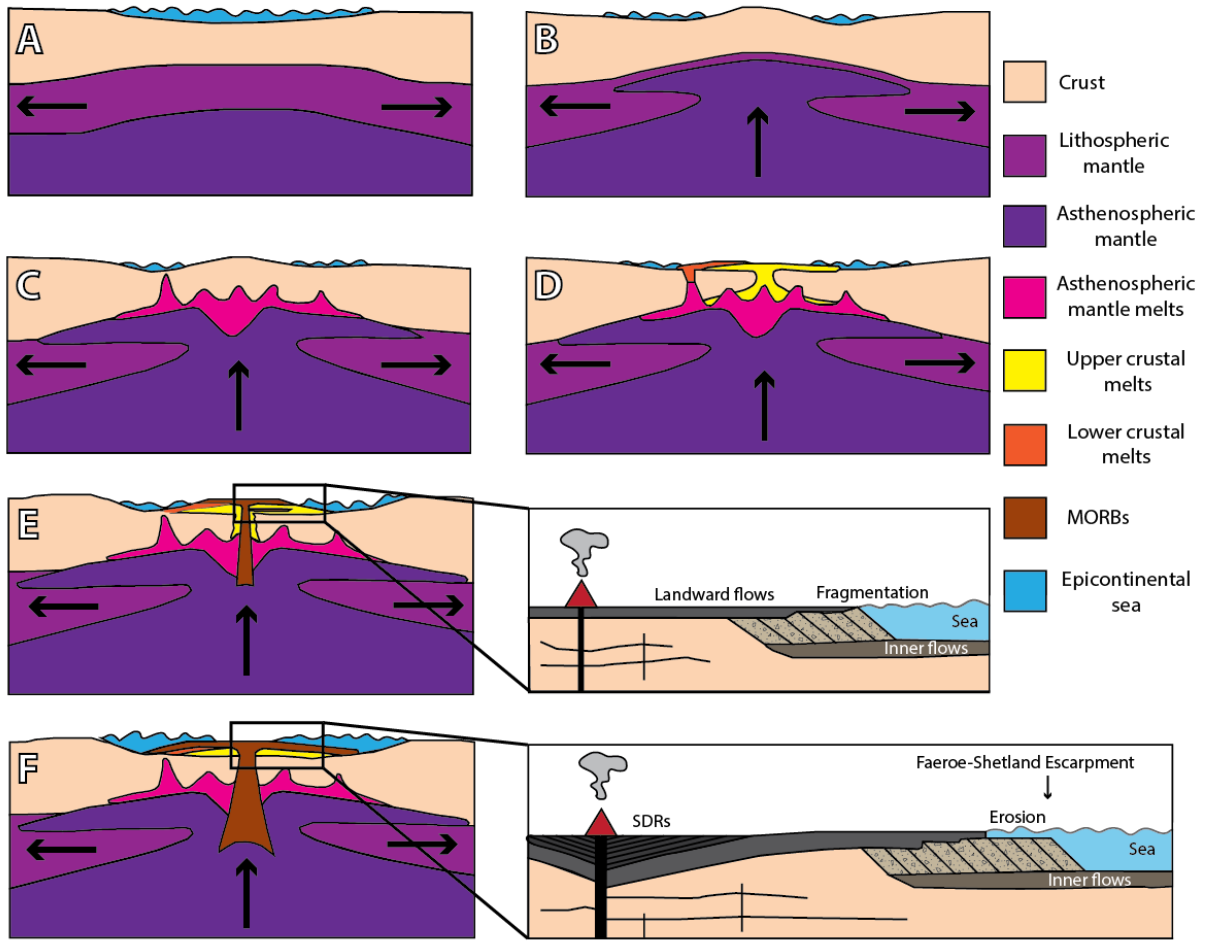

Figure 5.9: Schematic model presenting the proposed evolutionary history of the volcanic succession on the Møre Marginal High modified from Meyer et al. (2009). **(A)** Initiation of the latest rift phase between Greenland and Eurasia in the Late Cretaceous. **(B)** Paleocene uplift induced by the arrival of the Icelandic mantle plume. **(C)** The asthenosphere start to rise into the lithosphere and start to melt by decompression, and further intrudes the crust. **(D)** Increased heat transport causes partial melting of the crust. **(E)** Asthenospheric melts progressively rises to the surface resulting in the emplacement of MORB-like melt. The continental rupture is still not complete, leading to crustally contaminated athenospheric melts. The melts erupted at the surface are able to sustain until reaching the paleo-shoreline, where quenching leads to fragmentation and the formation of brecciated material that construct the lava delta. **(F)** During the rift-to-drift stage, huge amounts of uncontaminated MORB-like melts are emplaced at the surface leading to the formation of the SDRs. The lava delta experiences sea erosion that removes the subaerial top layer of parts of the construction.

6 Conclusions and future work

6.1 Conclusions

The volcanic succession in drill hole 6403/1-U-1 on the Møre Marginal High provides new knowledge of the Norwegian Volcanic Margin:

- The volcanic succession consists of brecciated material, comprising hyaloclastite and incorporated microcrystalline basalt clasts, and interlayered coherent lava flows.
- The volcanic succession is interpreted to derive from a lava-fed delta, based on the nature of the volcanic rocks and observations made from the seismic line located over the drill site. This confirms that the unit consisting of prograding reflectors in the seismic record of the area, and adjacent areas along the Norwegian Margin, have a volcanic origin.
- The magmatic samples have been classified as tholeiitic basalts with a MORB-like character.
- Clear evidence is found that the lavas have experienced contamination from the continental crust, presumably the upper continental crust.
- The succession is interpreted to derive from a mantle source more depleted than typical N-MORB sources.
- The succession has been emplaced prior to ~56 Ma, probably in the Late Paleocene.
- The lavas show affinities to other igneous rocks on the Vøring Marginal High, SE Greenland Margin and Jan Mayen Ridge, emplaced at the rift-to-drift transition during the opening of the Norwegian-Greenland Sea.

6.2 Suggestions for future work

To the best of my knowledge, this study presents the first documentation of Hf isotopic ratios of igneous rocks belonging to the NAIP. Since Hf is largely immobile and therefore relatively resistant to alteration, Hf isotopic data provide important information when identifying the source components of igneous rocks. They are therefore useful for identifying possible crustal contamination of magmas, especially when combined with Nd isotopic ratios which have been reported for most NAIP igneous rocks. Thus, a documentation of Hf isotopic ratios for other rift-to-drift related rocks would broaden the basis for comparison of the various rocks,

which can provide further valuable information on the magmatic evolution of the volcanic margin(s).

In addition, it would be interesting to perform *in situ* trace element analysis of the samples presented in this study, as all samples have undergone at least slight alteration. The *in situ* technique allows for spot analyses of small domains of fresh glass in the samples. By this, it is possible to avoid for instance alteration spots, filled vesicles and fractures, ensuring that only fresh areas in the sample are being analysed. The technique could for example be performed by laser ablation (LA) inductively coupled plasma mass spectrometry (ICP-MS).

It would also be desirable to make further constrains on the time of emplacement of the lava delta succession. This could be achieved by radiogenic dating methods, such as the ^{40}Ar-^{39}Ar method.

Appendix

Appendix

Appendix A – Core description

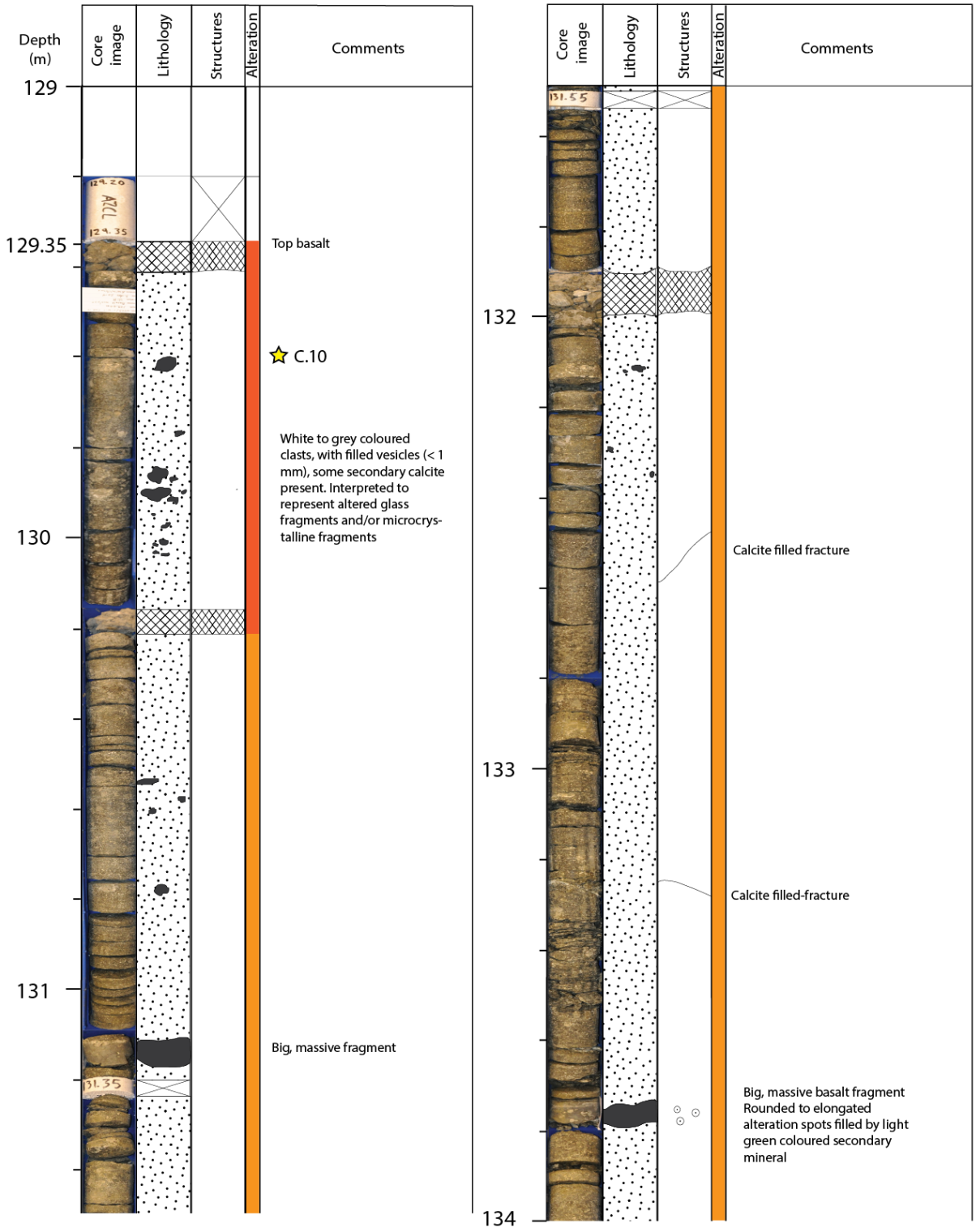

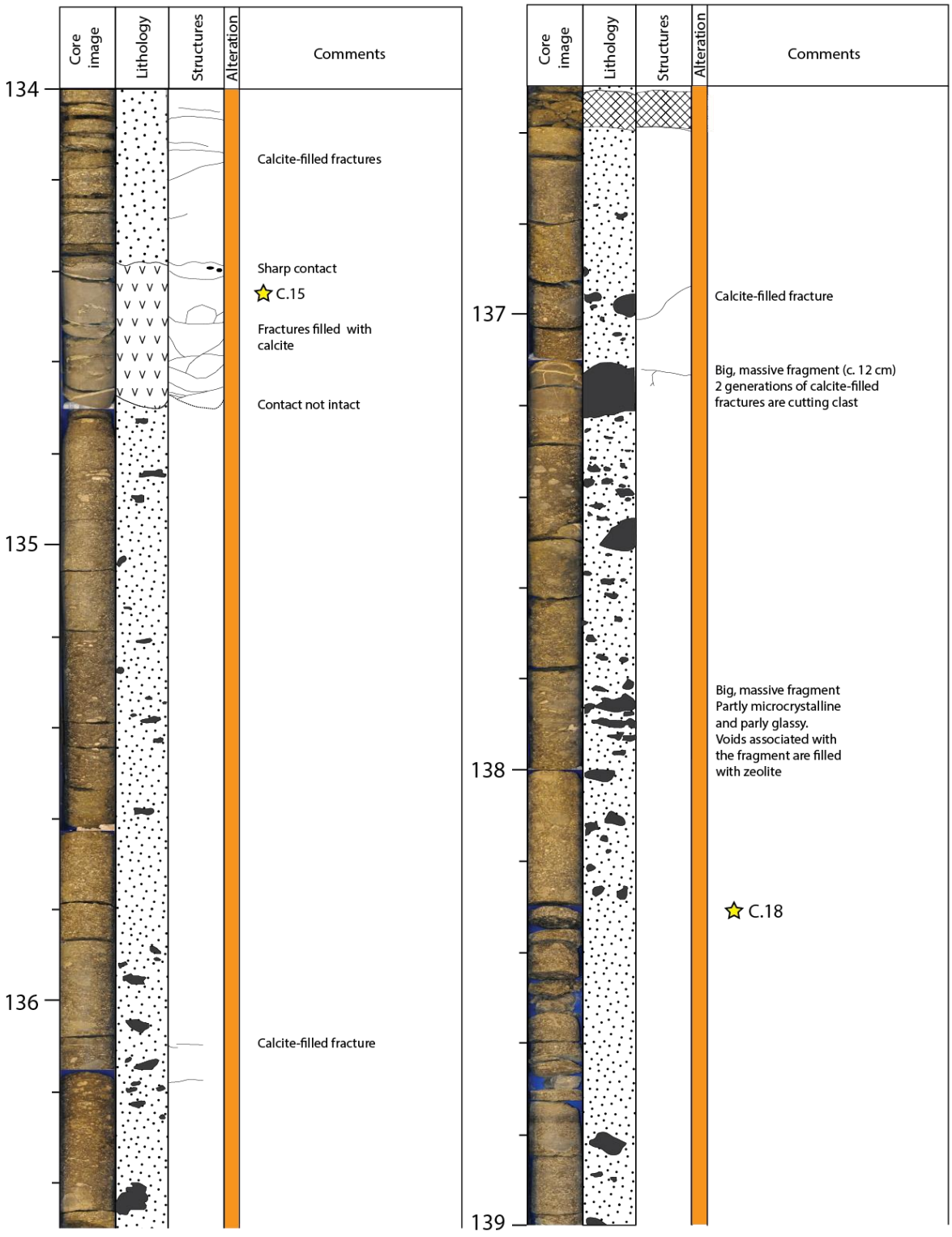
Core image
Lithology
Structures
Alteration
Comments
134
135
136
137
138
139
Calcite-filled fractures
Sharp contact
C.15
Fractures filled with calcite
Contact not intact
Calcite-filled fracture
Calcite-filled fracture
Big, massive fragment (c. 12 cm)
2 generations of calcite-filled fractures are cutting clast
Big, massive fragment
Partly microcrystalline and parly glassy.
Voids associated with the fragment are filled with zeolite
C.18

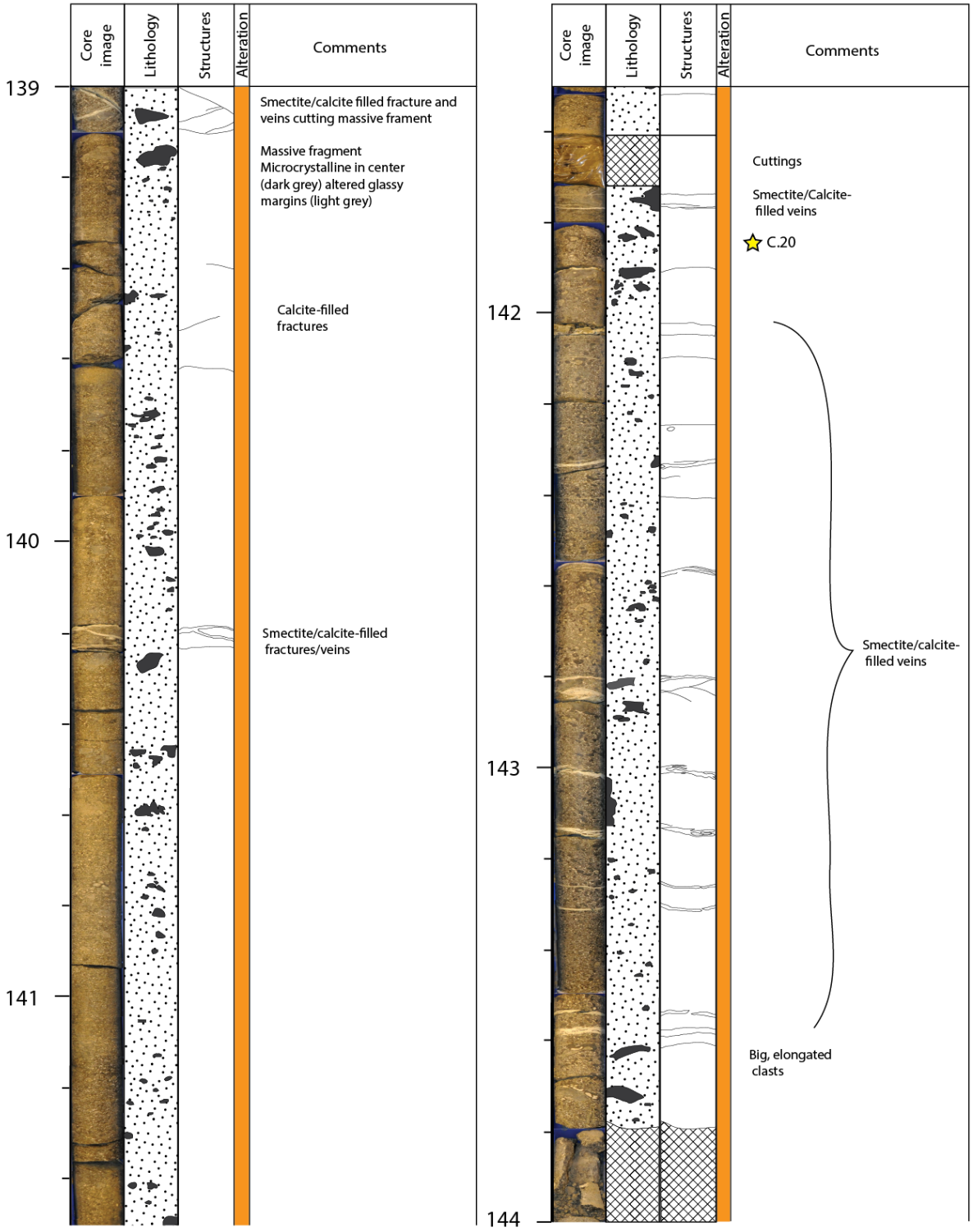
Core image
Lithology
Structures
Alteration
Comments
139
140
141
Smectite/calcite filled fracture and veins cutting massive frament
Massive fragment Microcrystalline in center (dark grey) altered glassy margins (light grey)
Calcite-filled fractures
Smectite/calcite-filled fractures/veins
142
143
144
Cuttings
Smectite/Calcite-filled veins
C.20
Smectite/calcite-filled veins
Big, elongated clasts

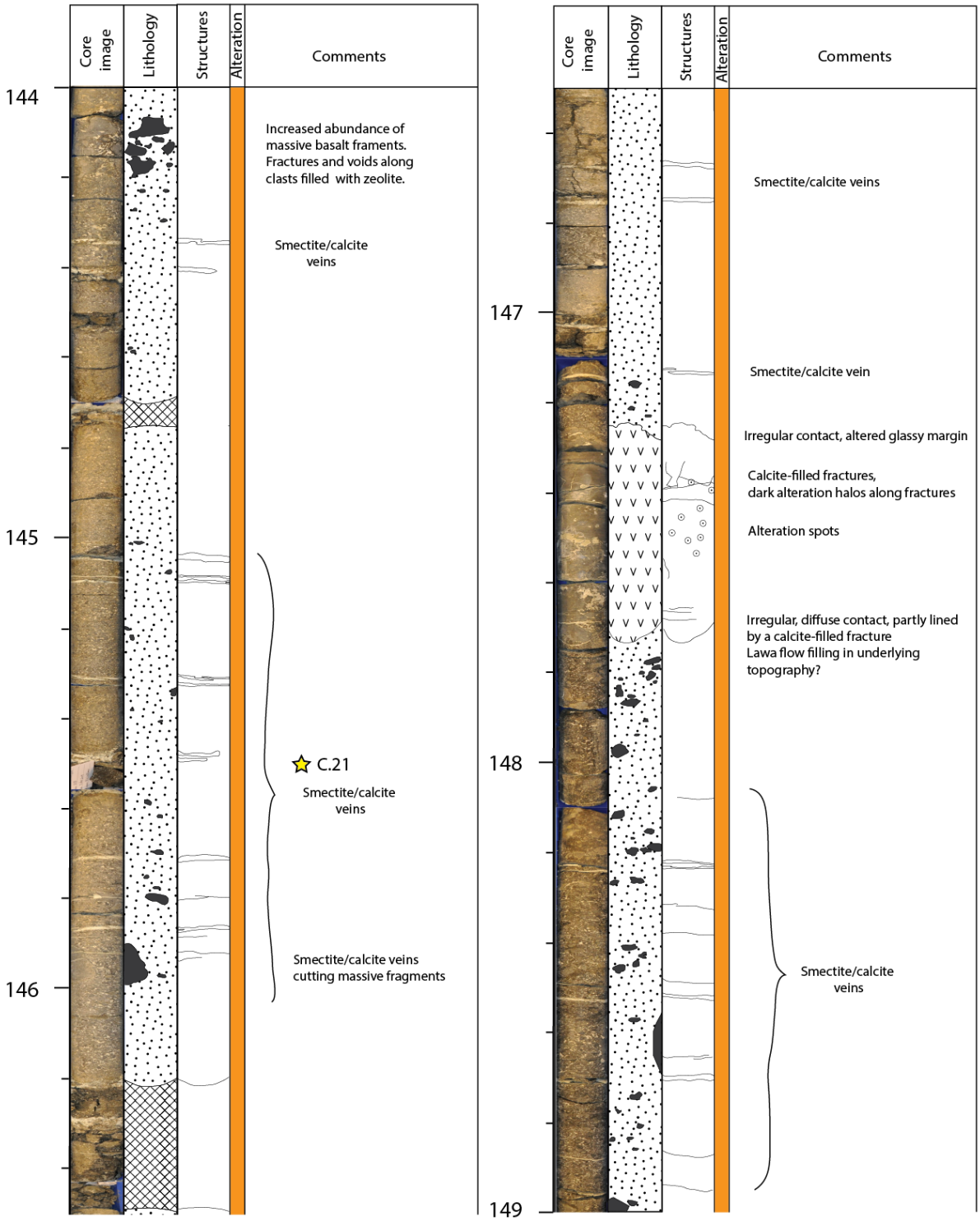
Core image
Lithology
Structures
Alteration
Comments
144
145
146
147
148
149
Increased abundance of massive basalt framents. Fractures and voids along clasts filled with zeolite.
Smectite/calcite veins
C.21
Smectite/calcite veins
Smectite/calcite veins cutting massive fragments
Smectite/calcite veins
Smectite/calcite vein
Irregular contact, altered glassy margin
Calcite-filled fractures, dark alteration halos along fractures
Alteration spots
Irregular, diffuse contact, partly lined by a calcite-filled fracture
Lawa flow filling in underlying topography?
Smectite/calcite veins

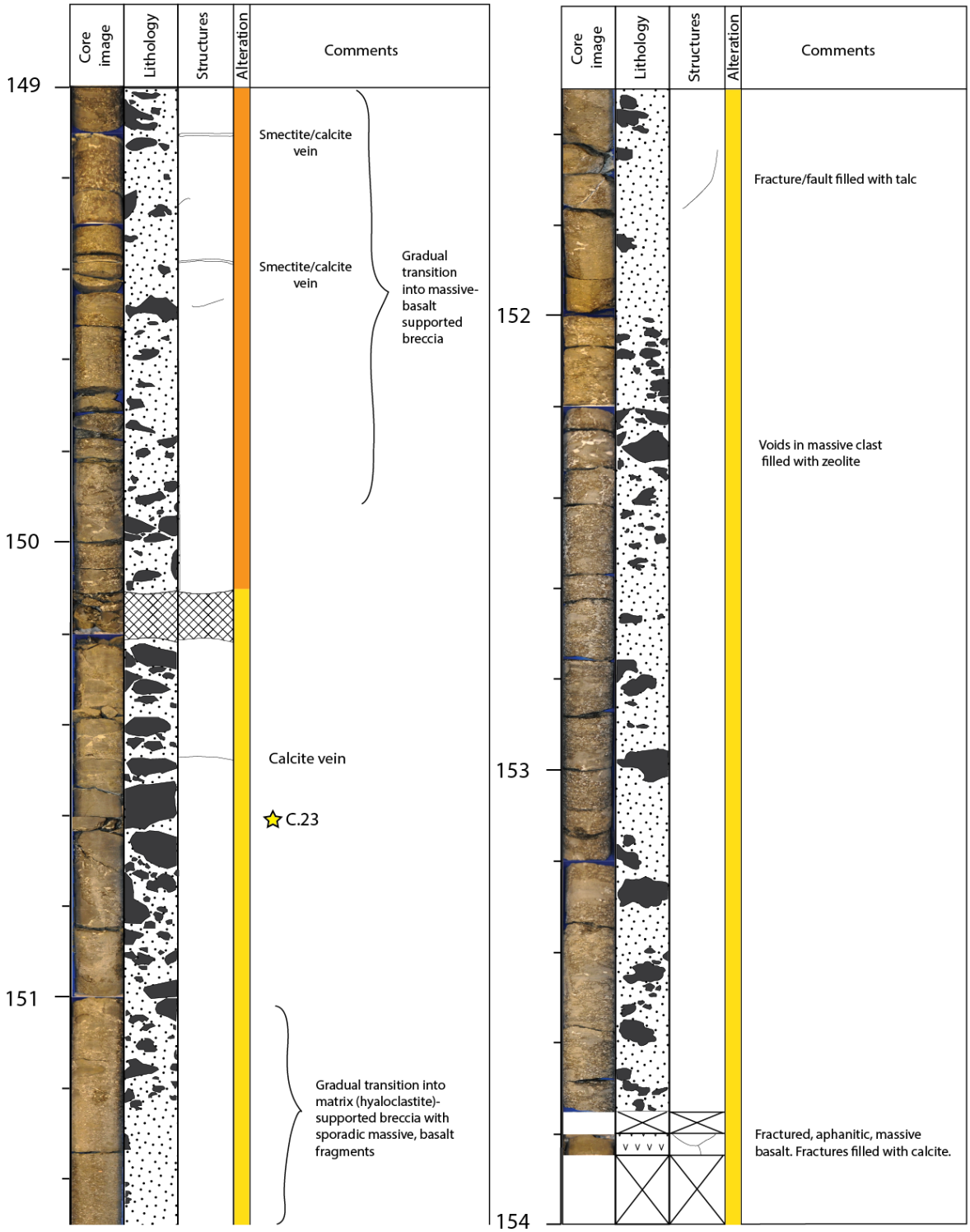
Core image
Lithology
Structures
Alteration
Comments
149
150
151
152
153
154
Smectite/calcite vein
Smectite/calcite vein
Gradual transition into massive-basalt supported breccia
Calcite vein
C.23
Gradual transition into matrix (hyaloclastite)-supported breccia with sporadic massive, basalt fragments
Fracture/fault filled with talc
Voids in massive clast filled with zeolite
Fractured, aphanitic, massive basalt. Fractures filled with calcite.

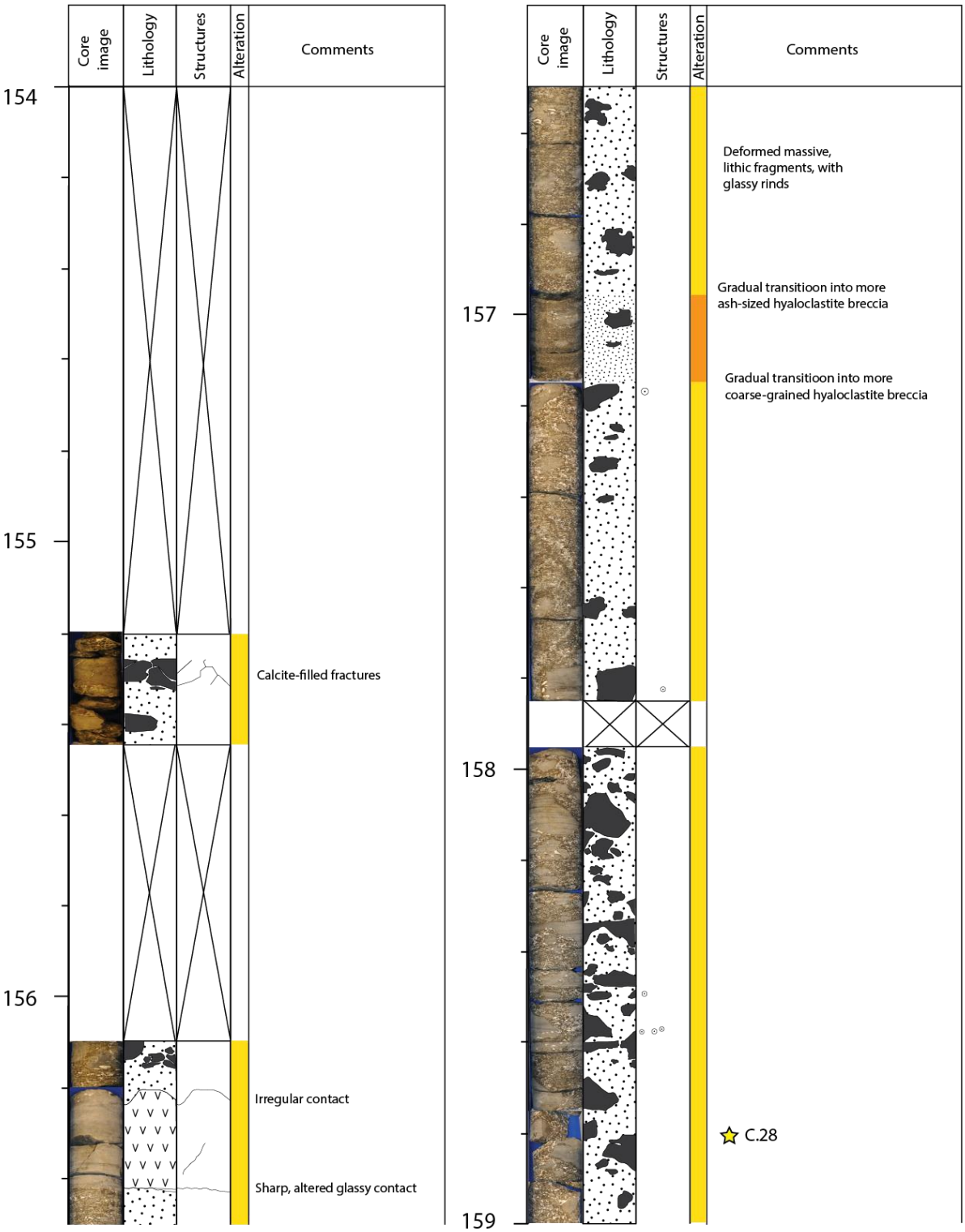
Core image
Lithology
Structures
Alteration
Comments
154
155
156
Calcite-filled fractures
Irregular contact
Sharp, altered glassy contact
Core image
Lithology
Structures
Alteration
Comments
157
158
159
Deformed massive, lithic fragments, with glassy rinds
Gradual transitioon into more ash-sized hyaloclastite breccia
Gradual transitioon into more coarse-grained hyaloclastite breccia
C.28

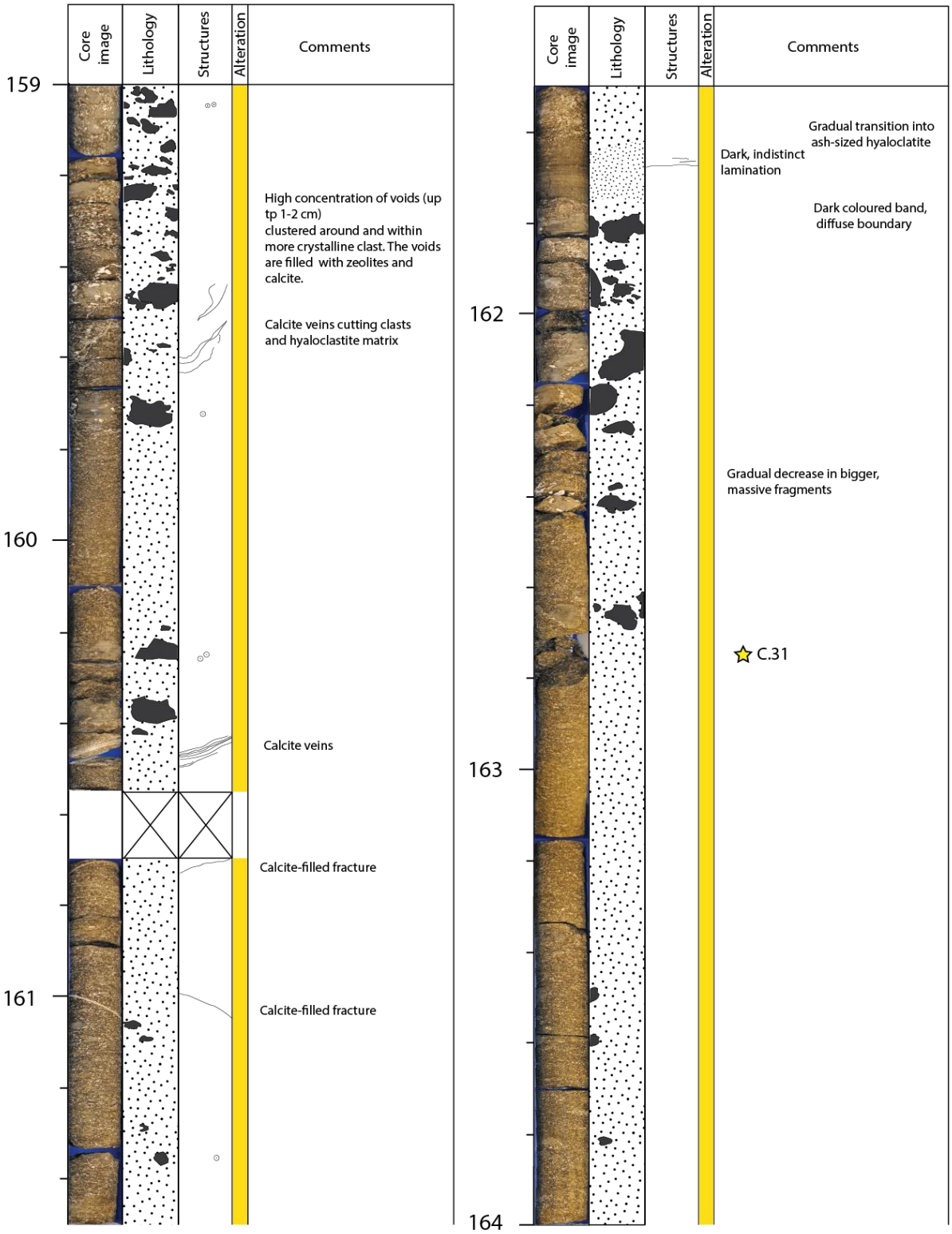
Core image
Lithology
Structures
Alteration
Comments
159
160
161
162
163
164
High concentration of voids (up tp 1-2 cm) clustered around and within more crystalline clast. The voids are filled with zeolites and calcite.
Calcite veins cutting clasts and hyaloclastite matrix
Calcite veins
Calcite-filled fracture
Calcite-filled fracture
Gradual transition into ash-sized hyaloclatite
Dark, indistinct lamination
Dark coloured band, diffuse boundary
Gradual decrease in bigger, massive fragments
C.31

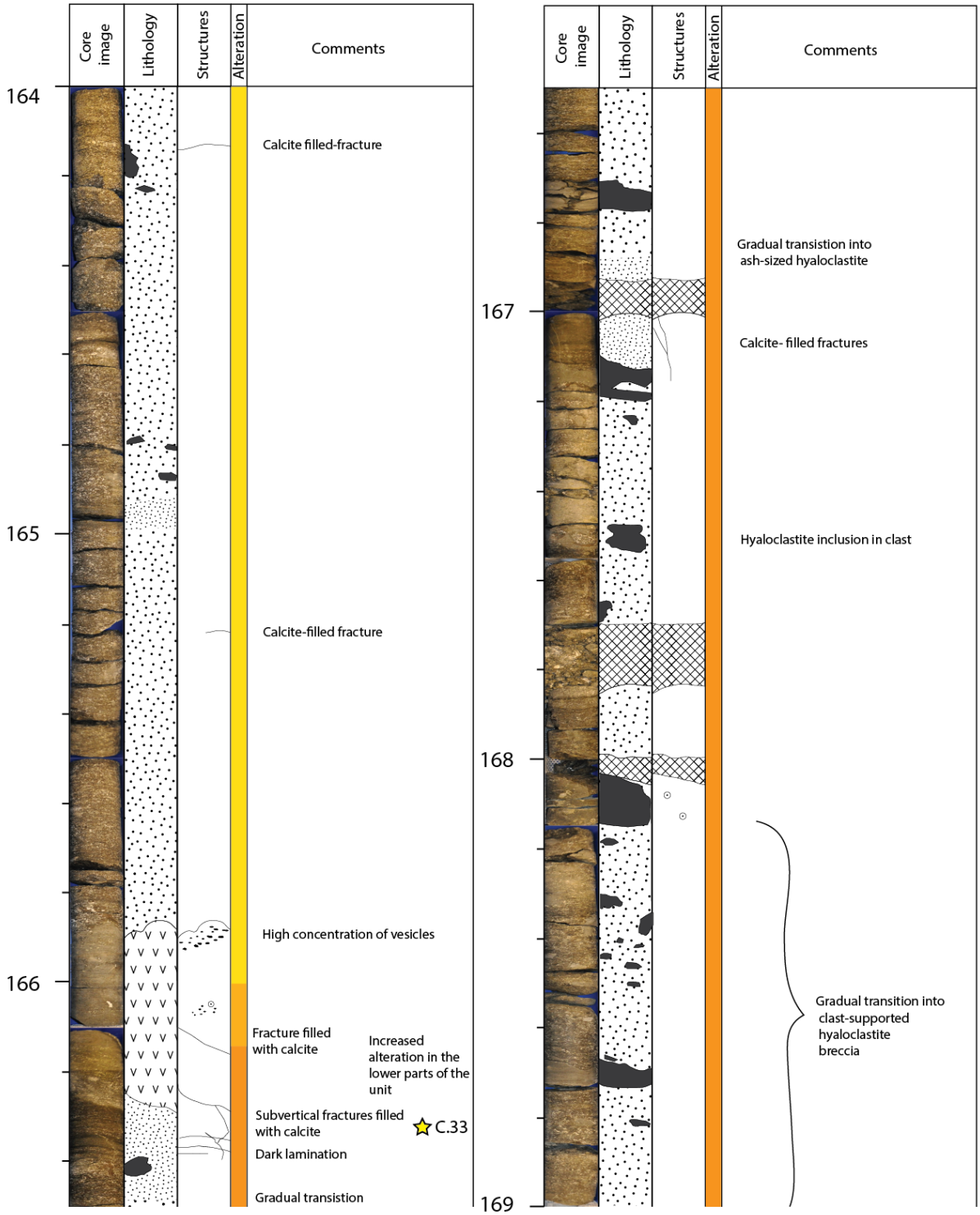
Core image
Lithology
Structures
Alteration
Comments
164
165
166
167
168
169
Calcite filled-fracture
Calcite-filled fracture
High concentration of vesicles
Fracture filled with calcite
Increased alteration in the lower parts of the unit
Subvertical fractures filled with calcite
C.33
Dark lamination
Gradual transistion
Gradual transition into ash-sized hyaloclastite
Calcite- filled fractures
Hyaloclastite inclusion in clast
Gradual transition into clast-supported hyaloclastite breccia

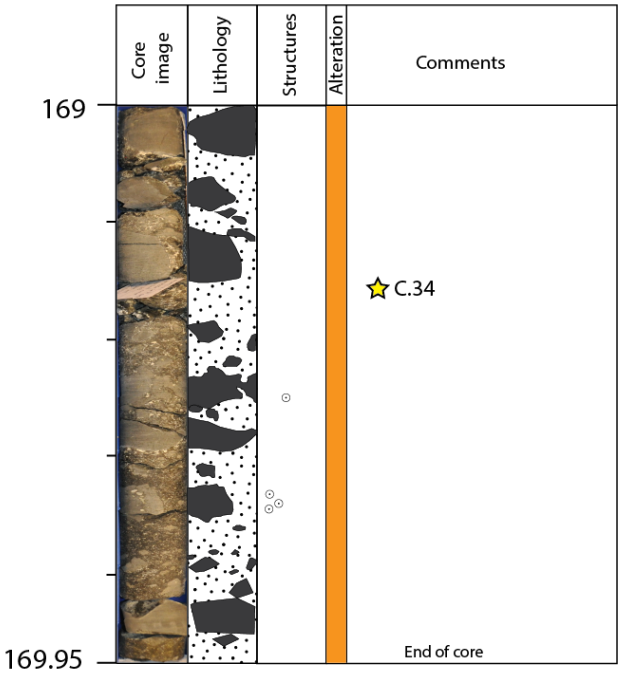

Legend

- No core
- Rubble
- Hyaloclastite (glass-breccia)
- Ash-sized hyaloclastite
- Coherent lava flow
- Massive, microcrystalline basalt clasts
- Sample location
- Fracture/vein
- Alteration spots
- Vesicles

Alteration

- Severe (>95 vol %)
- High (50-95 vol %)
- Moderate to high

Appendix B – Sample overview

Table B1: Overview of the samples and various analyses presented in the study.

Sample	Core depth (m)	Description	Thin section	Major element analysis	Trace element analysis	Isotope analysis
C.10	129.60	Heavily altered hyaloclastite	x			
C.15	134.45	Massive and microcrystalline coherent lava flow	x			
C.18	138.33	Hyaloclastite			x	x
C.20	141.85	Hyaloclastite	x		x	x
C.21	145.50	Hyaloclastite	x			
C.23	150.60	Massive, microcrystalline fragment in clast-supported breccia	x	x	x	x
C.28	158.85	Hyaloclastite	x	x	x	x
C.31	162.74	Hyaloclastite	x	x	x	x
C.33	166.32	Very fine-grained (ash-sized) hyaloclasitite			x	x
C.34	169.35	Massive, microcrystalline fragment in clast-supported breccia.	x			

Appendix C – Mineral analyses

Tabel C1: Listed and measured concentration (wt %) for the internal mineral standards used for control during mineral analyses. The accuracy is represented by the percentage recovery of the measured value compared to the listed value. The measured concentrations are the average of nine individual analyses.

Forsterite standard			
	Listed values	Measured values	Accuracy (REC%)
MgO	50,04	52,82	105,56
SiO_2	40,84	40,09	98,16
MnO	0,12	0,13	110,42
FeO	8,05	8,08	100,39

Fayalite standard			
	Listed values	Measured values	Accuracy (REC%)
SiO_2	29,75	26,96	90,63
MnO	2,54	2,14	84,43
FeO	66,85	63,48	94,96

Table C2: Measured concentrations (wt %) of olivine and plagioclase minerals for the samples C.28 and C.23, and the calculated Forsterite (Fo) and Anorthite (An) contents. The Fo content has been calculated as the molar Mg-number = 100* molar (MgO/(MgO+FeO)). The An content has been calculated as mole % An = mole Ca/(Ca+Na+K). All iron has been measured as Fe_2O_3. The measured concentrations are the average of nine individual analyses. n.a.: not analysed

Sample	C.28		C.23		C.28	C.23
Mineral	Olivine		Olivine		Plagioclase	Plagioclase
	1. gen.	2. gen.	1. gen.	2. gen.		
Na_2O	0,03	0,02	n.a.	n.a.	2,76	2,65
MgO	44,37	44,39	45,51	44,88	0,14	0,13
Al_2O_3	n.a.	n.a.	n.a.	n.a.	31,24	32,21
SiO_2	37,73	37,80	37,36	37,21	48,74	48,97
K_2O	0,06	0,05	0,02	0,01	0,04	0,05
CaO	0,31	0,37	0,29	0,34	16,19	16,92
TiO_2	0,02	0,06	0,02	0,03	0,05	0,03
MnO	0,19	0,25	0,21	0,26	0,02	0,02
Fe_2O_3	17,60	19,00	17,84	18,87	0,77	0,62
Total	100,31	101,94	101,24	101,61	99,95	101,60
Fo	83	82	84	83		
An					76	78

Appendix D – Major element data

Table D1: Certificated and measured concentrations (wt %) of the basaltic glass standard, USNM 113716, during SEM major element analysis. The certificated values are from Jarosewich et al. (1979). The measured concentrations are the average of nine individual analyses. n.a.: not analysed.

	Certificated values	Measured values	Accuracy (REC%)
Na_2O	2,48	2,73	110,08
MgO	8,21	7,99	97,36
Al_2O_3	15,39	15,48	100,60
SiO_2	51,52	51,45	99,87
P_2O_5	0,12	n.a.	-
K_2O	0,09	0,06	66,67
CaO	11,31	11,84	104,65
TiO_2	1,30	1,31	100,63
MnO	0,17	0,18	107,96
FeO*	9,13	9,52	104,26
Total	99,72	100,57	100,85

Table D2: Measured and normalised major element data (wt %) for selected samples (see Appendix B) from SEM analysis. The measured concentrations represent the average of nine individual analyses per sample. n.a.: not analysed.

	Matrix glass			Melt inclusions		
Sample	C.23	C.28	C.31	C.23-I	C.28-I	C.31-1
Na_2O	2,68	2,63	2,76	2,59	2,64	2,77
MgO	8,11	7,77	8,16	7,40	7,44	7,69
Al_2O_3	17,16	16,59	17,10	17,10	17,46	16,95
SiO_2	49,07	47,79	49,19	48,86	49,27	48,52
P_2O_5	n.a.	n.a.	n.a.	n.a.	n.a.	n.a.
K_2O	0,07	0,17	0,06	0,06	0,05	0,07
CaO	12,05	11,97	11,96	12,85	12,49	12,06
TiO_2	1,04	1,00	1,05	1,05	1,03	1,00
MnO	0,17	0,16	0,19	0,16	0,15	0,16
FeO*	10,76	10,51	10,56	10,57	10,18	10,08
Total	101,10	98,59	101,02	100,63	100,67	99,26

Normalised to 100%

	Matrix glass			Melt inclusions		
Sample	C.23	C.28	C.31	C.23-I	C.28-I	C.31-I
Na_2O	2,65	2,67	2,73	2,57	2,62	2,79
MgO	8,02	7,88	8,08	7,36	7,39	7,75
Al_2O_3	16,98	16,83	16,92	16,99	17,35	17,07
SiO_2	48,53	48,47	48,70	48,56	48,94	48,89
P_2O_5	n.a.	n.a.	n.a.	n.a.	n.a.	n.a.
K_2O	0,06	0,17	0,06	0,06	0,04	0,07
CaO	11,92	12,14	11,84	12,77	12,41	12,15
TiO_2	1,03	1,01	1,04	1,05	1,02	1,00
MnO	0,17	0,16	0,18	0,16	0,15	0,16
FeO*	10,64	10,66	10,45	10,50	10,12	10,15
Total	100,00	100,00	100,00	100,00	100,00	100,00

Appendix E – Trace element data

Table E1: Measured and recommended trace element abundances (ppm) for the BCR-2 standard during the time of ICP-MS analysis. Recommended concentrations and uncertainties are from Jochum et al. (2005).

Element	Measured value	Uncertainty (inst. RSD%)	Recommended value	Uncertainty	Accuracy (REC%)
Li	9,56	2,68	9,00	2,00	106,22
Sc	33,67	2,10	33,00	2,00	102,02
Ti	15203,93	2,00	13500	300	112,62
V	432,73	1,90	416,00	14,00	104,02
Cr	17,54	1,91	18,00	2,00	97,42
Mn	1574,31	2,32	1520	60	103,57
Co	37,45	1,88	37,00	3,00	101,21
Ni	13,47	1,82	12,57	0,30	107,15
Cu	16,67	2,17	19,00	2,00	87,73
Zn	137,68	2,25	127,00	9,00	108,41
Rb	45,96	1,89	48,00	2,00	95,76
Sr	337,41	1,80	346,00	14,00	97,52
Y	32,39	2,31	37,00	2,00	87,55
Zr	177,67	2,10	188,00	16,00	94,51
Nb	11,58	2,31	12,20	-	94,91
Cs	1,13	3,07	1,10	0,10	103,06
Ba	660,27	2,54	683,00	28,00	96,67
Hf	4,86	3,13	4,80	0,20	101,21
Ta	0,70	3,00	0,74	-	94,74
Pb	9,50	3,41	11,00	2,00	86,40
Th	5,21	2,52	6,20	0,70	83,96
U	1,53	3,41	1,69	0,19	90,51
Y	35,35	2,18	37,00	2,00	95,55
La	23,89	1,95	25	1	95,55
Ce	49,28	1,98	53	2	92,99
Pr	6,36	2,42	6,8	0,3	93,50
Nd	27,39	2,53	28	2	97,83
Sm	6,22	2,11	6,7	0,3	92,88
Eu	1,92	2,68	2,0	0,1	95,84
Gd	6,40	2,27	6,8	0,3	94,05
Tb	1,01	2,32	1,07	0,04	93,95
Dy	6,11	1,93	6,33	-	96,54
Ho	1,23	2,64	1,33	0,06	92,38
Er	3,53	2,52	3,62	-	97,52
Tm	0,50	2,04	0,54	-	92,24
Yb	3,20	2,41	3,5	0,2	91,51
Lu	0,49	2,82	0,51	0,02	96,27

Table E2: ICP-MS trace element concentrations (ppm) for selected samples (see Appendix B).

Samples	C.18	C.20	C.23	C.28	C.31	C.33
Li	24,25	21,56	7,75	6,26	8,55	14,28
Sc	52,15	64,86	2,12	2,86	45,36	69,28
Ti	8088	9011	5826	7342	6958	7586
V	234,5	254,2	213,4	233,6	220,8	222,4
Cr	848,8	774,2	717,5	1006	1284	833,5
Mn	1614	1717	1361	1341	1233	1258
Co	76,49	92,00	60,05	71,99	83,19	91,36
Ni	319,1	351,2	318,3	395,0	541,5	402,2
Cu	160,4	211,2	116,9	138,1	135	212,9
Zn	107,2	91,48	90,83	108,9	108,3	102,8
Rb	5,86	4,63	2,39	2,26	3,87	4,23
Sr	85,7	79,95	114,1	171,5	201,8	166,3
Y	18,85	15,93	15,77	19,79	21,59	20,99
Zr	88,33	116,4	60,73	74,64	74,63	117,4
Nb	2,06	2,30	1,52	1,83	1,78	2,01
Cs	0,250	0,150	0,020	0,014	0,140	0,150
Ba	7,08	1,48	53,08	31,55	14,91	6,26
Hf	2,80	3,66	1,87	2,31	2,36	3,65
Ta	0,130	0,170	0,090	0,109	0,110	0,160
Pb	1,69	1,84	1,20	1,37	1,92	1,96
Th	0,770	0,920	0,270	0,341	0,610	0,940
U	0,170	0,160	0,120	0,142	0,140	0,230
Y	19,97	16,82	17,44	22,56	23,14	22,20
La	2,36	2,19	2,80	3,40	3,27	5,40
Ce	6,34	5,80	7,32	8,92	8,63	12,66
Pr	1,03	0,93	1,17	1,44	1,38	1,76
Nd	5,70	5,25	6,71	8,13	7,77	9,09
Sm	2,27	2,10	2,45	2,94	2,89	3,12
Eu	0,93	0,82	0,95	1,16	1,13	1,17
Gd	3,03	2,84	3,13	3,77	3,71	3,88
Tb	0,55	0,45	0,54	0,64	0,63	0,69
Dy	3,64	2,78	3,43	4,23	4,19	4,50
Ho	0,77	0,57	0,73	0,89	0,88	0,97
Er	2,31	1,69	2,17	2,61	2,59	3,00
Tm	0,35	0,25	0,31	0,38	0,38	0,48
Yb	2,29	1,65	2,05	2,48	2,55	3,31
Lu	0,35	0,27	0,31	0,38	0,40	0,53

Appendix F – Isotope data

Table F: Sr, Nd, Hf and Pb isotopic ratios for selected samples (see Appendix B).

Sample	87/86Sr	2S error	143/144Nd	2S error	176/177Hf	2S error
C.18	0,707443	0,000009	0,512826	0,000006	0,283117	0,000004
C.20	0,707950	0,000008	0,512830	0,000006	0,283111	0,000006
C.23	0,704380	0,000008	0,512832	0,000006	0,283116	0,000004
C.28	0,706008	0,000009	0,512824	0,000007	0,283115	0,000006
C.31	0,706651	0,000008	0,512829	0,000008	0,283120	0,000006
C.33	0,707362	0,000009	0,512833	0,000006	0,283118	0,000006

	206/204Pb	error	207/204Pb	error	208/204Pb	error
C.18	18,1559	0,0002	15,5218	0,0002	38,1385	0,0007
C.20	18,2541	0,0002	15,5298	0,0002	38,2554	0,0007
C.23	18,1584	0,0003	15,5223	0,0002	38,1288	0,0008
C.28	18,1180	0,0002	15,5197	0,0002	38,0861	0,0006
C.31	17,9140	0,0002	15,5297	0,0002	37,8717	0,0007
C.33	18,1417	0,0002	15,5240	0,0002	38,1131	0,0006

References

Abdelmalak, M. M., Planke, S., Faleide, J. I., Jerram, D. A., Zastrozhnov, D., Eide, S., and Myklebust, R., 2016, The development of volcanic sequences at rifted margins: New insights from the structure and morphology of the Vøring Escarpment, mid-Norwegian Margin: Journal of Geophysical Research: Solid Earth, v. 121, no. 7, p. 5212-5236.

Alt, J. C., 2004, Alteration of the upper oceanic crust: mineralogy, chemistry, and processes, *in* Davis, E. E., and Elderfield, H., eds., Hydrogeology of the oceanic lithosphere, Volume 1: Cambridge, UK, Cambridge University Press, p. 495-533.

Arevalo, R., and McDonough, W. F., 2010, Chemical variations and regional diversity observed in MORB: Chemical Geology, v. 271, no. 1, p. 70-85.

Asmerom, Y., and Jacobsen, S. B., 1993, The Pb isotopic evolution of the Earth: inferences from river water suspended loads: Earth and Planetary Science Letters, v. 115, no. 1-4, p. 245-256.

Bergh, S. G., and Sigvaldason, G. E., 1991, Pleistocene mass-flow deposits of basaltic hyaloclastite on a shallow submarine shelf, South Iceland: Bulletin of Volcanology, v. 53, no. 8, p. 597-611.

Berndt, C., Planke, S., Alvestad, E., Tsikalas, F., and Rasmussen, T., 2001, Seismic volcanostratigraphy of the Norwegian Margin: constraints on tectonomagmatic break-up processes: Journal of the Geological Society, v. 158, no. 3, p. 413-426.

Blystad, P., Brekke, H., Færseth, R. B., Skogseid, J., and Tørudbakken, B., 1995, Structural Elements of the Norwegian Continental Shelf. Pt. 2. The Norwegian Sea Region, NPD-Bulletin No 8, Norwegian Petroleum Directorate

Boulter, M. C., and Manum, S. B., 1989, The Brito-Arctic Igneous Province flora around the Paleocene/Eocene boundary, *in* Eldholm, O., Thiede, J., and Taylor, E., eds., Proceedings of the Ocean Drilling Program, Scientific Results, Volume 104: College Station, TX, Ocean Drilling Program, p. 663-680.

Brekke, H., 2000, The tectonic evolution of the Norwegian Sea continental margin, with emphasis on the Vøring and Møre basins: Geological Society, London, Special Publications, v. 167, p. 327-378.

Chauvel, C., Garçon, M., Bureau, S., Besnault, A., Jahn, B. M., and Ding, Z., 2014, Constraints from loess on the Hf–Nd isotopic composition of the upper continental crust: Earth and Planetary Science Letters, v. 388, p. 48-58.

Dalland, A., Augedal, H. O., Bomstad, K., and Ofstad, K., 1988, The Post-Triassic succession of the Mid-Norwegian Shelf, *in* Dalland, A., Worsley, D., and Ofstad, K., eds., A Lithostratigraphic Scheme for the Mesozoic and Cenozoic and Succession Offshore Mid-and Northern Norway, NPD-Bulletin No 4, Norwegian Petroluem Directorate.

Deniel, C., and Pin, C., 2001, Single-stage method for the simultaneous isolation of lead and strontium from silicate samples for isotopic measurements: Analytica Chimica Acta, v. 426, no. 1, p. 95-103.

Doré, A. G., Lundin, E. R., Jensen, L. N., Birkeland, Ø., Eliassen, P. E., and Fichler, C., 1999, Principal tectonic events in the evolution of the northwest European Atlantic margin, *in* Fleet, A. J., and Boldy, S. A. R., eds., Petroleum Geology of Northwest Europe: Proceedings of the 5th Conferance, Geological Society, London, p. 41-61.

Eldholm, O., and Mutter, J. C., 1986, Basin structure on the Norwegian margin from analysis of digitally recorded sonobuoys: Journal of Geophysical Research: Solid Earth, v. 91, no. B3, p. 3763-3783.

Eldholm, O., Thiede, J., and Taylor, E., 1987a, Evolution of the Norwegian Continental Margin: Background and Objectives, *in* Eldholm, O., Thiede, J., and Taylor, E., eds., Proceedings of the Ocean Drilling Program, Initial Reports, Volume 104: College Station, TX, Ocean Drilling Program, p. 5-25.

Eldholm, O., Thiede, J., and Taylor, E., 1987b, Summary and Preliminary Conclusions, ODP Leg 104, *in* Eldholm, O., Thiede, J., and Taylor, E., eds., Proceedings of the Ocean Drilling Program, Initial Reports, Volume 104: College Station, TX, Ocean Drilling Program, p. 751-771.

Eldholm, O., Thiede, J., and Taylor, E., 1989a, Evolution of the Vøring Volcanic Margin, *in* Eldholm, O., Thiede, J., and Taylor, E., eds., Proceedings of the Ocean Drilling Program, Scientific Results, Volume 104: College Station, TX, Ocean Drilling Program, p. 1033-1065.

Eldholm, O., Thiede, J., and Taylor, E., 1989b, The Norwegian Continental Margin: Tectonic, Volcanic, and Paleoenvironmental Framework, *in* Eldholm, O., Thiede, J., and Taylor, E., eds., Proceedings of the Ocean Drilling Program, Scientific Results, Volume 104: College Station, TX, Ocean Drilling Program, p. 5-26.

Eldholm, O., Tsikalas, F., and Faleide, J. I., 2002, Continental margin off Norway 62–75° N: Palaeogene tectono-magmatic segmentation and sedimentation: Geological Society, London, Special Publications, v. 197, no. 1, p. 39-68.

Faleide, J. I., Tsikalas, F., Breivik, A. J., Mjelde, R., Ritzmann, O., Engen, O., Wilson, J., and Eldholm, O., 2008, Structure and evolution of the continental margin off Norway and the Barents Sea: Episodes, v. 31, no. 1, p. 82-91.

Faure, G., and Mensing, T. M., 2005, Isotopes: principles and applications, Hoboken, N.J., Wiley, 897 p.

Fisher, R. V., 1984, Submarine volcaniclastic rocks: Geological Society, London, Special Publications, v. 16, no. 1, p. 5-27.

Fitton, J. G., Hardarson, B. S., Ellam, R. M., and Rogers, G., 1998a, Sr-, Nd-, and Pb-isotopic composition of volcanic rocks from the southeast Greenland Margin at 63 N: temporal variation in crustal contamination during continental breakup, *in* Saunders, A. D., Larsen, H. C., and Wise, S. W., Jr., eds., Proceedings of the Ocean Drilling Program, Scientific Results, Volume 152: College Station, TX, Ocean Drilling Program, p. 351-357.

Fitton, J. G., Larsen, L. M., Saunders, A. D., Hardarson, B. S., and Kempton, P. D., 2000, Palaeogene continental to oceanic magmatism on the SE Greenland continental margin at 63 N: a review of the results of Ocean Drilling Program Legs 152 and 163: Journal of Petrology, v. 41, no. 7, p. 951-966.

Fitton, J. G., Saunders, A. D., Larsen, L. M., Hardarson, B. S., and Norry, M. J., 1998b, Volcanic rocks from the southeast Greenland margin at 63N: Composition, petrogenesis, and mantle sources, *in* Saunders, A. D., Larsen, H. C., and Wise, S. W., Jr., eds., Proceedings of the Ocean Drilling Program, Scientific results, Volume 152: College Station, TX, Ocean Drilling Program, p. 331-350.

Foulger, G. R., and Anderson, D. L., 2005, A cool model for the Iceland hotspot: Journal of Volcanology and Geothermal Research, v. 141, no. 1, p. 1-22.

Foulger, G. R., Natland, J. H., and Anderson, D. L., 2005, Genesis of the Iceland melt anomaly by plate tectonic processes: Geological Society of America Special Papers, v. 388, p. 595-625.

Fowler, A. D., Berger, B., Shore, M., Jones, M. I., and Ropchan, J., 2002, Supercooled rocks: development and significance of varioles, spherulites, dendrites and spinifex in Archaean volcanic rocks, Abitibi Greenstone belt, Canada: Precambrian Research, v. 115, no. 1, p. 311-328.

Hamelin, C., Bezos, A., Dosso, L., Escartin, J., Cannat, M., and Mevel, C., 2013, Atypically depleted upper mantle component revealed by Hf isotopes at Lucky Strike segment: Chemical Geology, v. 341, p. 128-139.

Hinz, K., Dostman, H. J., and Hanisch, J., 1984, Structural elements of the Norwegian Sea continental margin: Geol. Jahrb. A, v. 75, p. 193-211.

Hirschmann, M. M., and Stolper, E. M., 1996, A possible role for garnet pyroxenite in the origin of the "garnet signature" in MORB: Contributions to Mineralogy and Petrology, v. 124, no. 2, p. 185-208.

Hjelstuen, B. O., Eldholm, O., and Skogseid, J., 1999, Cenozoic evolution of the northern Vøring margin: Geological Society of America Bulletin, v. 111, no. 12, p. 1792-1807.

Hofmann, A. W., 1997, Mantle geochemistry: the message from oceanic volcanism: Nature, v. 385, no. 6613, p. 219-229.

Hofmann, A. W., 2003, Sampling Mantle Heterogeneity through Oceanic Basalts: Isotopes and Trace Elements, *in* Holland, H. D., and Turekian, K. K., eds., Treatise on Geochemistry, Volume 2: Oxford, Elsevier, p. 61-101.

Haaga, K. A., 2014, Petrogenesis of Jan Mayen Ridge magmas in space and time [Master thesis]: University of Bergen, 194 p.

Irvine, T. N., and Baragar, W. R. A., 1971, A guide to the chemical classification of the common volcanic rocks: Canadian Journal of Earth Sciences, v. 8, no. 5, p. 523-548.

Jarosewich, E., Nelen, J. A., and Norberg, J. A., 1979, Electron microprobe reference samples for mineral analyses: Smithsonian Contributions to the Earth Sciences, v. 22, p. 68-72.

Jochum, K. P., Nohl, U., Herwig, K., Lammel, E., Stoll, B., and Hofmann, A. W., 2005, GeoReM: a new geochemical database for reference materials and isotopic standards: Geostandards and Geoanalytical Research, v. 29, no. 3, p. 333-338.

Jochum, K. P., and Verma, S. P., 1996, Extreme enrichment of Sb, Tl and other trace elements in altered MORB: Chemical Geology, v. 130, no. 3-4, p. 289-299.

Kharin, G. N., 1976, The Petrology of Magmatic Rocks, DSDP Leg 38, *in* Talwani, M., and Udintsev, G. B., eds., Initial Reports of the Deep Sea Drilling Project, Volume 38: Washington, U.S Government Printing Office, p. 685-715.

Kharin, G. N., Udintsev, G. B., Bogatikov, O. A., Dmitriev, J. I., Raschka, H., Kreuzer, H., Mohr, M., Harre, W., and Eckhardt, F. J., 1976, K/Ar ages of the Basalts of the Norwegian-Greenland Sea, DSDP Leg 38, *in* Talwani, M., and Udintsev, G. B., eds., Initial Reports of the Deep Sea Drilling Project, Volume 38: Washington, U.S. Government Printing Office, p. 755-759.

King, S. D., 2005, North Atlantic topographic and geoid anomalies: The result of a narrow ocean basin and cratonic roots?: Geological Society of America Special Papers, v. 388, p. 653-664.

King, S. D., and Anderson, D. L., 1995, An alternative mechanism of flood basalt formation: Earth and Planetary Science Letters, v. 136, no. 3, p. 269-279.

King, S. D., and Anderson, D. L., 1998, Edge-driven convection: Earth and Planetary Science Letters, v. 160, no. 3, p. 289-296.

Klein, E. M., 2003, Geochemistry of the Igneous Oceanic Crust *in* Holland, H. D., and Turekian, K. K., eds., Treatise on Geochemistry, Volume 3: Oxford, Elsevier, p. 433-463.

Korenaga, J., 2004, Mantle mixing and continental breakup magmatism: Earth and Planetary Science Letters, v. 218, no. 3, p. 463-473.

Krolikowska-Ciaglo, S., Hauff, F., and Hoernle, K., 2005, Sr-Nd isotope systematics in 14–28 Ma low-temperature altered mid-ocean ridge basalt from the Australian Antarctic Discordance, Ocean Drilling Program Leg 187: Geochemistry, Geophysics, Geosystems, v. 6, no. 1, p. 1-18.

Kruber, C., Thorseth, I. H., and Pedersen, R. B., 2008, Seafloor alteration of basaltic glass: textures, geochemistry, and endolithic microorganisms: Geochemistry, Geophysics, Geosystems, v. 9, no. 12, p. 1-18.

Larsen, H. C., Saunders, A. D., and Clift, P. D., 1994a, Introduction: Breakup of the southeast Greenland margin and the formation of the Irminger Basin: Background and scientific objectives, *in* Larsen, H. C., Saunders, A. D., and Clift, P. D., eds., Proceedings of the Ocean Drilling Program, Initial Reports, Volume 152: College Station, TX, Ocean Drilling Program, p. 5-16.

Larsen, H. C., Saunders, A. D., and Clift, P. D., 1994b, Site 917, *in* Larsen, H. C., Saunders, A. D., and Clift, P. D., eds., Proceedings of the Ocean Drilling Program, Initial Reports, Volume 152: College Station, TX, Ocean Drilling Program, p. 107-158.

Le Bas, M. J., Le Maitre, R. W., Streckeisen, A., and Zanettin, B., 1986, A chemical classification of volcanic rocks based on the total alkali-silica diagram: Journal of Petrology, v. 27, no. 3, p. 745-750.

LeHuray, A. P., and Johnson, E. S., 1989, Rb-Sr systematics of site 642 volcanic rocks and alteration minerals, *in* Eldholm, O., Thiede, J., and Taylor, E., eds., Proceedings of the Ocean Drilling Program, Scientific Results, Volume 104: College Station, TX, Ocean Drilling Program, p. 437-448.

McPhie, J., Doyle, M., and Allen, R., 1993, Volcanic textures: a guide to the interpretation of textures in volcanic rocks, Hobart, CODES Key Centre, University of Tasmania, 198 p.

Meyer, R., Hertogen, J., Pedersen, R. B., Viereck-Götte, L., and Abratis, M., 2009, Interaction of mantle derived melts with crust during the emplacement of the Vøring Plateau, NE Atlantic: Marine Geology, v. 261, no. 1, p. 3-16.

Meyer, R., Van Wijk, J., and Gernigon, L., 2007, The North Atlantic Igneous Province: A review of models for its formation, *in* Foulger, G. R., and Jurdy, D. M., eds., Plates, plumes and planetary processes, Volume 430: Boulder, Geological Society of America Special Papers, p. 525-552.

Mjelde, R., Faleide, J. I., Breivik, A. J., and Raum, T., 2009a, Lower crustal composition and crustal lineaments on the Vøring Margin, NE Atlantic: a review: Tectonophysics, v. 472, no. 1, p. 183-193.

Mjelde, R., Kasahara, J., Shimamura, H., Kamimura, A., Kanazawa, T., Kodaira, S., Raum, T., and Shiobara, H., 2002, Lower crustal seismic velocity-anomalies; magmatic underplating or serpentinized peridotite? Evidence from the Vøring Margin, NE Atlantic: Marine Geophysical Researches, v. 23, no. 2, p. 169-183.

Mjelde, R., Raum, T., Kandilarov, A., Murai, Y., and Takanami, T., 2009b, Crustal structure and evolution of the outer Møre Margin, NE Atlantic: Tectonophysics, v. 468, no. 1, p. 224-243.

Moore, J. G., Phillips, R. L., Grigg, R. W., Peterson, D. W., and Swanson, D. A., 1973, Flow of lava into the sea, 1969–1971, Kilauea Volcano, Hawaii: Geological Society of America Bulletin, v. 84, no. 2, p. 537-546.

Neumann, E. R., Svensen, H., Tegner, C., Planke, S., Thirlwall, M., and Jarvis, K. E., 2013, Sill and lava geochemistry of the mid-Norway and NE Greenland conjugate margins: Geochemistry, Geophysics, Geosystems, v. 14, no. 9, p. 3666-3690.

Newbury, D. E., and Ritchie, N. W. M., 2015, Performing elemental microanalysis with high accuracy and high precision by scanning electron microscopy/silicon drift detector energy-dispersive X-ray spectrometry (SEM/SDD-EDS): Journal of Materials Science, v. 50, no. 2, p. 493-518.

Newcombe, M. E., Fabbrizio, A., Zhang, Y., Ma, C., Le Voyer, M., Guan, Y., Eiler, J. M., Saal, A. E., and Stolper, E. M., 2014, Chemical zonation in olivine-hosted melt inclusions: Contributions to Mineralogy and Petrology, v. 168, no. 1, p. 1-26.

Newsom, H. E., White, W. M., Jochum, K. P., and Hofmann, A. W., 1986, Siderophile and chalcophile element abundances in oceanic basalts, Pb isotope evolution and growth of the Earth's core: Earth and Planetary Science Letters, v. 80, no. 3-4, p. 299-313.

Nobre Silva, I. G., Weis, D., and Scoates, J. S., 2010, Effects of acid leaching on the Sr-Nd-Hf isotopic compositions of ocean island basalts: Geochemistry, Geophysics, Geosystems, v. 11, no. 9.

NPD, 2014, The 2014 NPD lithostratigraphic charts: http://www.npd.no/en/Topics/Geology/Lithostratigraphy/ (accessed April 2017).

Parson, L., Viereck, L., Love, D., Gibson, I., Morton, A., and Hertogen, J., 1989, The Petrology of the Lower Sereis Volcanics, ODP site 642, *in* Eldholm, O., Thiede, J., and Taylor, E., eds., Proceedings of the Ocean Drilling Program, Scientific Results: College Station, TX, Ocean Drilling Program, p. 419-428.

Pin, C., Briot, D., Bassin, C., and Poitrasson, F., 1994, Concomitant separation of strontium and samarium-neodymium for isotopic analysis in silicate samples, based on specific extraction chromatography: Analytica Chimica Acta, v. 298, no. 2, p. 209-217.

Planke, S., and Alvestad, E., 1999, Seismic volcanostratigraphy of the extrusive breakup complexes in the northeast Atlantic: implications from ODP/DSDP drilling, *in* Larsen, H. C., Duncan, R. A., Allan, J. F., and Brooks, K., eds., Proceedings of the Ocean Drilling Program, Scientific Results, Volume 163: College Station, TX, Ocean Drilling Program, p. 3-16.

Planke, S., Rasmussen, T., Rey, S. S., and Myklebust, R., 2005, Seismic characteristics and distribution of volcanic intrusions and hydrothermal vent complexes in the Vøring and Møre basins, *in* Doré, A. G., and Vining, B. A., eds., Petroleum Geology: North-West Europe and Global Perspectives - Proceedings of the 6th Petroleum conference, Volume 6: London, Geological Society p. 833-844.

Planke, S., Skogseid, J., and Eldholm, O., 1991, Crustal structure off Norway, 62 to 70 north: Tectonophysics, v. 189, no. 1, p. 91-107.

Planke, S., Symonds, P. A., Alvestad, E., and Skogseid, J., 2000, Seismic volcanostratigraphy of large-volume basaltic extrusive complexes on rifted margins: Journal of Geophysical Research: Solid Earth, v. 105, no. B8, p. 19335-19351.

Robinson, J. A. C., and Wood, B. J., 1998, The depth of the spinel to garnet transition at the peridotite solidus: Earth and Planetary Science Letters, v. 164, no. 1–2, p. 277-284.

Rudnick, R. L., and Gao, S., 2014, Composition of the Continental Crust *in* Holland, H. D., and Turekian, K. K., eds., Treatise on Geochemistry (Second Edition), Volume 4: Oxford, Elsevier, p. 1-51.

Salters, V. J. M., and Stracke, A., 2004, Composition of the depleted mantle: Geochemistry, Geophysics, Geosystems, v. 5, no. 5, p. 1-27.

Saunders, A. D., Fitton, J. G., Kerr, A. C., Norry, M. J., and Kent, R. W., 1997, The north Atlantic igneous province, *in* Mahoney, J. J., and Coffin, M. F., eds., Large igneous provinces: continental, oceanic, and planetary flood volcanism: Washington, AGU Geophysical Monograph, p. 45-93.

Schilling, J. G., 1976, Rare-earth, Se, Cr, Fe, Co, and Na abundances in DSDP leg 38 basement basalts: some additional evidence on the evolution of the Thulean Volcanic Province, *in* Talwani, M., and Udintsev, G. B., eds., Initial Reports of the Deep Sea Drilling Project, Volume 38: Washington, U.S. Government Printing Office, p. 741-750.

Sen, G., 2014, Petrology: Principles and Practice, Berlin, Springer, 368 p.

Skilling, I. P., 2002, Basaltic pahoehoe lava-fed deltas: large-scale characteristics, clast generation, emplacement processes and environmental discrimination: Geological Society, London, Special Publications, v. 202, no. 1, p. 91-113.

Skogseid, J., and Eldholm, O., 1989, Vøring Plateau continental margin: seismic interpretation, stratigraphy and vertical movements, *in* Eldholm, O., Thiede, J., and Taylor, E., eds., Proceedings of the Ocean Drilling Program, Scientific Results, Volume 104: College Station, TX, Ocean Drilling Program, p. 993-1030.

Smythe, D. K., 1983, Faeroe-Shetland Escarpment and continental margin north of the Faeroes, *in* Bott, M. H. P., Saxov, S., Talwani, M., and Thiede, J., eds., Structure and Development of the Greenland-Scotland Ridge: New Yourk, Springer, p. 109-119.

Smythe, D. K., Chalmers, J. A., Skuce, A. G., Dobinson, A., and Mould, A. S., 1983, Early opening history of the North Atlantic—I. Structure and origin of the Faeroe—Shetland Escarpment: Geophysical Journal International, v. 72, no. 2, p. 373-398.

Styve, E., 2015, Petrogenesis of igneous samples from from the Gjallar Ridge and the Vøring Spur [Master thesis]: University of Bergen, 153 p.

Sun, S.-s., and McDonough, W. F., 1989, Chemical and isotopic systematics of oceanic basalts: implications for mantle composition and processes: Geological Society, London, Special Publications, v. 42, no. 1, p. 313-345.

Talwani, M., and Eldholm, O., 1972, Continental margin off Norway: a geophysical study: Geological Society of America Bulletin, v. 83, no. 12, p. 3575-3606.

Talwani, M., Mutter, J., and Hinz, K., 1983, Ocean continent boundary under the Norwegian continental margin, Structure and Development of the Greenland-Scotland Ridge, Springer, p. 121-131.

Talwani, M., and Udintsev, G. B., 1976, Tectonic synthesis *in* Talwani, M., and Udintsev, G. B., eds., Initial Reports of the Deep Sea Drilling Project, Volume 38: Washington, U.S. Government Printing Office, p. 1213-1242.

Taylor, P. N., and Morton, A. C., 1989, Sr, Nd, and Pb isotope geochemistry of the upper and lower volcanic series at Site 642, *in* Eldholm, O., Thiede, J., and Taylor, E., eds., Proceedings of the Ocean Drilling Program, Scientific Results, Volume 104: College Station, TX, Ocean Drilling Program, p. 429-435.

Verma, S. P., 1992, Seawater alteration effects on REE, K, Rb, Cs, Sr, U, Th, Pb and Sr–Nd–Pb isotope systematics of mid-ocean ridge basalt: Geochemical Journal, v. 26, no. 3, p. 159-177.

Viereck, L. G., Hertogen, J., Parson, L. M., Morton, A. C., Love, D., and Gibson, I. L., 1989, Chemical stratigraphy and petrology of the Vøring Plateau tholeiitic lavas and interlayered volcaniclastic sediments at ODP hole 642E1, *in* Eldholm, O., Thiede, J., and Taylor, E., eds., Proceedings of the Ocean Drilling Program, Scientific results, Volume 104: College Station, TX, Ocean Drilling Program, p. 367-396.

Viereck, L. G., Taylor, P. N., Parson, L. M., Morton, A. C., Hertogen, J., and Gibson, I. L., 1988, Origin of the Palaeogene Vøring Plateau volcanic sequence: Geological Society, London, Special Publications, v. 39, no. 1, p. 69-83.

Walton, A. W., and Schiffman, P., 2003, Alteration of hyaloclastites in the HSDP 2 Phase 1 Drill Core 1. Description and paragenesis: Geochemistry, Geophysics, Geosystems, v. 4, no. 5, p. 1-31.

Watton, T. J., Jerram, D. A., Thordarson, T., and Davies, R. J., 2013, Three-dimensional lithofacies variations in hyaloclastite deposits: Journal of Volcanology and Geothermal Research, v. 250, p. 19-33.

White, J. D. L., 2000, Subaqueous eruption-fed density currents and their deposits: Precambrian Research, v. 101, no. 2, p. 87-109.

Winchester, J. W., 1963, Rare earth chromatography using bis-(2-ethylhexyl) orthophosphoric acid: Journal of Chromatography A, v. 10, p. 502-506.

Wood, D. A., 1980, The application of a Th-Hf-Ta diagram to problems of tectonomagmatic classification and to establishing the nature of crustal contamination of basaltic lavas of the British Tertiary Volcanic Province: Earth and Planetary Science Letters, v. 50, no. 1, p. 11-30.

Workman, R. K., and Hart, S. R., 2005, Major and trace element composition of the depleted MORB mantle (DMM): Earth and Planetary Science Letters, v. 231, no. 1, p. 53-72.

Wright, K. A., Davies, R. J., Jerram, D. A., Morris, J., and Fletcher, R., 2012, Application of seismic and sequence stratigraphic concepts to a lava-fed delta system in the Faroe-Shetland Basin, UK and Faroes: Basin Research, v. 24, no. 1, p. 91-106.